Biomaterials 280 (2022) 121247

Contents lists available at ScienceDirect

Biomaterials

journal homepage: www.elsevier.com/locate/biomaterials

Microfluidic nanomaterials: From synthesis to biomedical applications

Kavitha Illath [a], Srabani Kar [b], Pallavi Gupta [a], Ashwini Shinde [a], Syrpailyne Wankhar [c], Fan-Gang Tseng [d], Ki-Taek Lim [e], Moeto Nagai [f], Tuhin Subhra Santra [a,*]

[a] Department of Engineering Design, Indian Institute of Technology Madras, India
[b] Department of Electrical Engineering, University of Cambridge, UK
[c] Department of Bioengineering, Christian Medical College Vellore, Vellore, India
[d] Department of Engineering and System Science, National Tsing Hua University, Hsinchu, Taiwan
[e] Department of Biosystems Engineering, Kangwon National University, South Korea
[f] Department of Mechanical Engineering, Toyohashi University of Technology, Aichi, Japan

ARTICLE INFO

Keywords:
Microfluidics
Nanomaterials
Screening
Clinical evaluations
Biomedical applications

ABSTRACT

Microfluidic platforms gain popularity in biomedical research due to their attractive inherent features, especially in nanomaterials synthesis. This review critically evaluates the current state of the controlled synthesis of nanomaterials using microfluidic devices. We describe nanomaterials' screening in microfluidics, which is very relevant for automating the synthesis process for biomedical applications. We discuss the latest microfluidics trends to achieve noble metal, silica, biopolymer, quantum dots, iron oxide, carbon-based, rare-earth-based, and other nanomaterials with a specific size, composition, surface modification, and morphology required for particular biomedical application. Screening nanomaterials has become an essential tool to synthesize desired nanomaterials using more automated processes with high speed and repeatability, which can't be neglected in today's microfluidic technology. Moreover, we emphasize biomedical applications of nanomaterials, including imaging, targeting, therapy, and sensing. Before clinical use, nanomaterials have to be evaluated under physiological conditions, which is possible in the microfluidic system as it stimulates chemical gradients, fluid flows, and the ability to control microenvironment and partitioning multi-organs. In this review, we emphasize the clinical evaluation of nanomaterials using microfluidics which was not covered by any other reviews. In the future, the growth of new materials or modification in existing materials using microfluidics platforms and applications in a diversity of biomedical fields by utilizing all the features of microfluidic technology is expected.

1. Introduction

Microfluidic devices are systems that use small amounts of fluids (10^{-9} to 10^{-18} L) which manipulate through channels ranging from tens to hundreds of micrometers [1]. Over the past couple of years, microfluidics has emerged as a solution to several biomedical problems in the areas of antibody testing [2–4], tissue engineering [5–8], drug delivery [9–12], cellular targeting [13,14], cell isolation [15–19], single-cell analysis [20–22], etc. Most of these applications demand nanomaterials (NMs) as an essential tool to act either as a biomarker [23–25], a fluorescent probe for bioanalysis [26–29], antitumor agent [30], drug or gene carrying vehicles [31–36], toxin and pathogens detectors [37], and imaging probe in *in vivo* and *in vitro* analysis [28,38–40]. Each application requires particular NMs with a specific shape, composition, size, morphology, and surface modification.

In general, every NMs synthesize method falls under top-down or bottom-up approaches. In the top-down approach, the bulk material is chiseled down into small nano-sized particles and produces NMs in a naked form, which is easily oxidized and agglomerate intensively [41–43]. Further, this approach introduces surface imperfections and crystallographic defects, and thus, it can change the physical and surface properties of NMs [44]. Due to these drawbacks, the top-down approach is not suitable for NMs synthesis for biomedical applications. On the other hand, in a bottom-up approach, individual atoms or molecules are used to build NMs using solid-state [43,45], liquid state (or wet chemical) [46,47], gas phase [43], and biological methods [48–50]. The wet chemical synthesis is the most commonly employed bottom-up approach of NMs synthesis for biomedical applications due to its simplicity, flexibility, usage of inexpensive chemicals, and significant production rates of stable NMs compared to others [43]. The wet chemical synthesis deals

* Corresponding author.
E-mail addresses: tuhin@iitm.ac.in, santra.tuhin@gmail.com (T.S. Santra).

https://doi.org/10.1016/j.biomaterials.2021.121247
Received 1 May 2021; Received in revised form 5 November 2021; Accepted 8 November 2021
Available online 11 November 2021

with the chemical reactions in the solution phase using an ionic salt precursor with appropriate experimental conditions. It includes methods such as solvothermal [46,47], hydrothermal [51,52], sol-gel [53], chemical reduction [54,55], nanoprecipitation [56], etc, which involve liquid phase at one of the processing stages. Generally, wet synthesis carries out in a laboratory conical flask/beaker keep it in a stirrer hot plate arrangement, known as the conventional batch reactor method. However, in a conventional batch reactor, it is challenging to achieve the desired characteristics of NMs precisely due to the poor control over reaction kinetics [57–59]. It has been found that it is possible to convert these methods into microfluidic platforms to enhance the performance.

The key feature of the microfluidic devices for material synthesis is the use of a high surface-area-to-volume ratio. It allows abrupt heat and mass transfer, resulting in rapid cooling and heating of reagents that maintains an isothermal condition [60–62]. Hence, the reaction is faster in microfluidics (a few seconds or less) than in the conventional batch reactor (which takes hours or days). The consumption of reagent in microfluidics is minimum; hence the cost of synthesis is low, making the device transportation and storage safe. In contrast, the consumption of reagents is large or medium in a conventional batch reactor. As the microfluidic-based synthesis carry out in an enclosed environment, they are safe while handling toxic and flammable solvents [63,64]. At the same time, it is challenging to handle harsh conditions in a conventional batch reactor. The microfluidics technologies can monitor the evolution of reactions in the spatial and temporal domains, allowing real-time monitoring of the reaction parameters and produced NMs [65]. Therefore, with the help of programmable equipment and real-time monitoring, automation is possible [66,67]. In the conventional batch reactor, automation is lacking as it requires watching over the process [68].

The most crucial advantage is precise control over each step in NMs formation using microfluidics, whereas conventional batch reactors lack control over reaction steps [57–59,69,70]. Moreover, in microfluidics, the device design and flow rate of reagents are tunable and provide flexible reactions. At the same time, the conventional batch reactor has only a stirring rate as the tunable parameter [68]. Further, microfluidic devices have shown promises for synthesizing homogenous particles with narrow size distribution along with high or medium reproducibility, and scale-up validation is straightforward [71–73]. Low

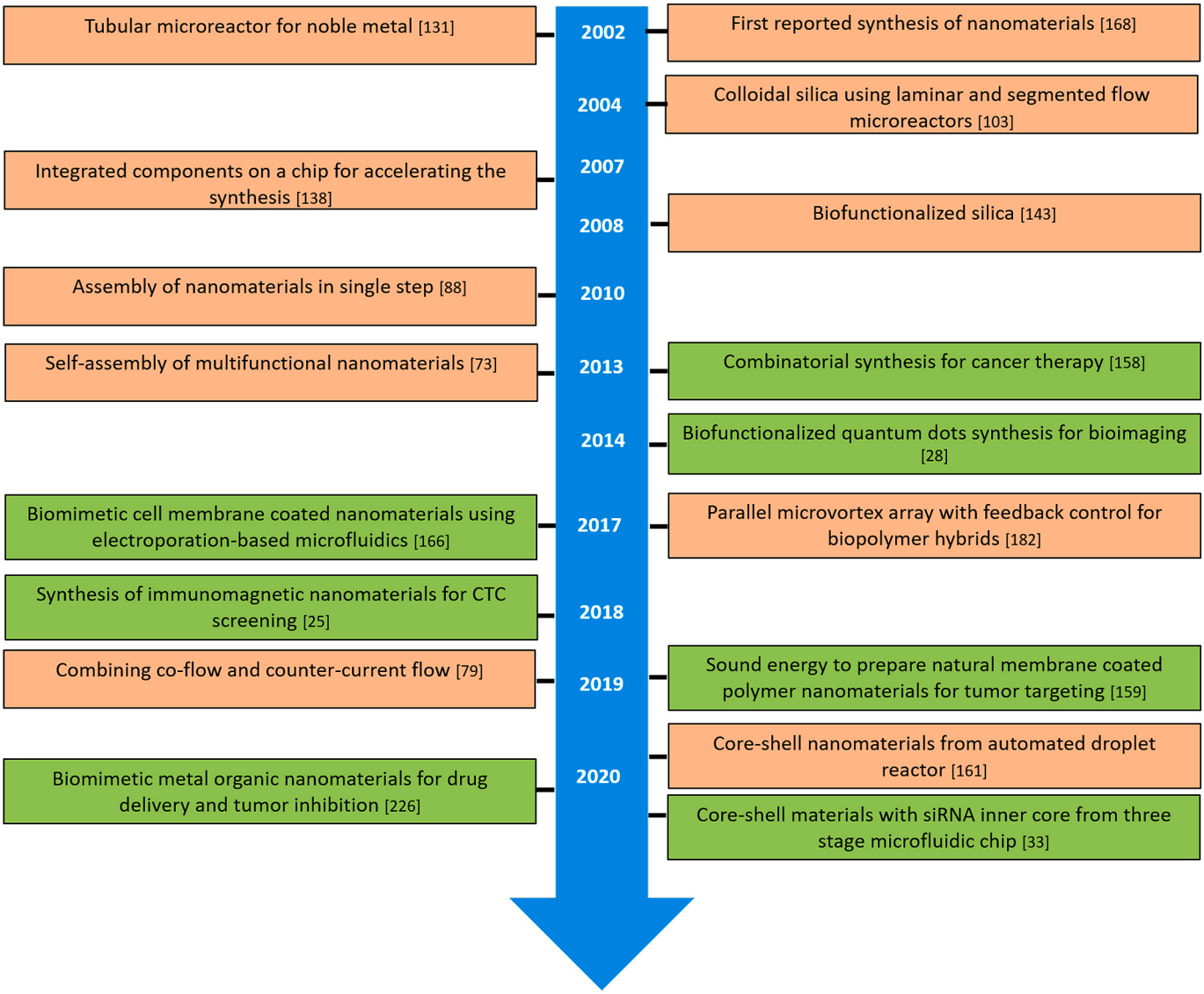

Fig. 1. Key historical events in microfluidics-based NMs synthesis for biomedical applications. NMs synthesis (pink) and biomedical application-specific (green) synthesis in microfluidics. CTC, circulating tumor cell; siRNA, small interfering ribonucleic acid; PDMS, polydimethylsiloxane. (For interpretation of the references to color in this figure legend, the reader is referred to the Web version of this article.)

reproducibility is observed in a conventional batch reactor, and the size distribution over the batch production is nonhomogeneous with large size distribution [71]. One of the most challenging fields of nanotechnology is the production of NMs for biomedical applications, which require NMs in the form of assembly/hybrid in most cases with highly monodispersed and reproducible form [63]. Interestingly, these microfluidic devices are capable of synthesizing nanohybrids, core-shell, and assembly of materials with reasonable control over the reaction kinetics using geometries such as hydrodynamic [74–80], flow-focusing [81–86], and coaxial flow [87–90] or nanoemulsification [91], etc. compared to the conventional method [74–80]. Thus, microfluidics offers a research and development pilot studies platform for NMs synthesis.

The past decade has witnessed a massive increment in the fabrication of NMs for biomedical applications using microfluidics and is expected to continue in the future. Especially in the past two years, increment in academic research is significant as per the Scopus and Web of Science data. Industry reports also revealed that the global microfluidics market is expected to grow at a 19.8% compound annual growth rate from 2019 to 2030 [92]. Another study conducted by Mordor Intelligence revealed the growing importance of the microfluidic sector in healthcare applications [93]. Trends in health care technology demand more production of NMs and microfluidics to facilitate the same. Key historical events in NMs synthesis using microfluidics for biomedical application are shown in Fig. 1.

There are few reviews published in recent years on the different facets of NMs synthesis using microfluidic technology. Most of them focus on specific microfluidic technology such as a droplet, hydrodynamic flow-focusing, etc. [75,76,81,94]. Nevertheless, only a few of them pertains to biomedical applications of NMs synthesized by microfluidic technology [57–59,64,95]. Further, a review on screening and clinical evaluation of these NMs synthesized by microfluidics is not yet attempted, which is an essential step for the successful application of these NMs. The last two years witnessing the introduction of several new concepts, technological demonstration, and successful application of microfluidics in biomedical NMs synthesis demand a comprehensive review of this topic. Recently, Zhao et al. described various microfluidic technologies to fabricate nanoparticles and nanofibers and explained their potential biomedical applications [58]. However, our review not only focuses on the controlled NMs synthesis using microfluidics for biomedical applications, but also the screening of NMs parameters and clinical evaluation of NMs using microfluidics with critical examples. Hence, this review tries to fill the gap between NMs synthesis and its biomedical applications, by analyzing the screening and clinical evaluation of synthesized materials. Few reviews have briefly mentioned the screening of parameters, but a detailed description of real-time monitoring of NMs parameters for fully automated synthesis is not available. Also, the clinical evaluation of NMs using microfluidics was not covered by any other reviews, which is crucial before the application was performed. Overall, this brief review tries to update, organize, and critically analyze the recent development in NMs synthesized by microfluidic devices for biomedical applications, with a particular focus on their screening and clinical evaluation in microfluidics and their biomedical applications.

This review discusses the latest trends in NMs synthesis for biomedical applications using microfluidic technology, including its screening, clinical evaluation, and biomedical applications. It is divided into four sections; the first section analyses the current advancement in synthesizing noble metal, silica, biopolymer, iron oxide, quantum dots, carbon-based, rare-earth-based, and other NMs using various microfluidic devices. Tuning parameters and controlled synthesis are explained under each category of NMs. Second, we describe the progress in screening NMs using microfluidic technology, which has become an essential procedure for automating the process, speeding up the synthesis, and easy validation for scale-up production. Third, we describe the clinical evaluation of NMs in microfluidics even though it is not fully established for clinical use. Key evaluation parameters such as NMs' hemocompatibility, toxicity, transport, uptake by cells, target NMs accumulation, and its efficacy are discussed with the various microfluidics models, including blood vessel-on-a-chip, blood-brain barrier model, single-cell microfluidics, lung-on-a-chip, tumor-on-a-chip, body-on-a-chip, and animal-on-a-chip, with their advantages, disadvantages, and perspectives. Essential applications in imaging, sensing, targeting, and therapy using NMs synthesized from the microfluidic platform are discussed in the fourth section. Last, we focus on the challenges associated with the current microfluidic technology for biomedical application-specific NMs synthesis and propose solutions.

2. Microfluidic nanomaterials synthesis

One of the most challenging areas of nanotechnology is the production of NMs for biomedical applications. Over the years, technological advancement in material science produced NMs in the form of a hollow shell, assembly of materials, hybrid, core-shell, and drug/molecule loaded NMs required for biomedical applications. Interestingly, microfluidic technologies' features helped to fabricate these NMs with precise control over the reaction parameters with a short period and minimal reagent consumption [63].

A typical microfluidic device for the synthesis of NMs has a reagent handling zone (inlets), a micromixing zone, a reaction zone, a subsequent microchannel, and a product collecting zone (outlet). The reagent handling zone pumps the reagent into the channels, reagents mix in the micromixing zone, reaction zone provides sufficient residence time, and NMs can be collected from the product collecting zone. In general, NMs synthesis in the microfluidic platform can be achieved by either mixing single or multiple miscible solvents (single-phase microfluidics) or mixing multiple immiscible solvents (multiphase microfluidics). Several microfluidic architectures are available to achieve either single-phase flow (or continuous flow) or multiphase flow (or segmented flow) for NMs synthesis.

Single-phase microfluidics (Fig. 2a) is the most widely used microfluidics in NMs synthesis due to their simplicity and versatile control of reagents, temperature, reaction time, and flow rate. Most of them are developed to work at low Reynolds numbers; hence the flow pattern is laminar. Generally used mixing modules are winding and distributed channel mixing [64]. Mixing efficiency is down due to laminar flow. Hence different geometries are adapted, including zig-zag [97], intersecting [98], spiral [99], and 3D serpentine [25] or twisted structures [100]. The problems with single-phase microfluidics include broad-sized NMs, broad residence time distribution, Taylor dispersion, lengthy channels, and difficulty in isolating growing NMs from the microchannel walls. A reliable solution to overcome these difficulties is to adapt multiphase microfluidics [96,101,102]. By adding a new immiscible phase, recirculation motion is triggered to enhance the solution's folding and stretching, promoting mixing efficiency. This can be achieved in three ways; (1) gas-liquid flow, (2) liquid-liquid flow, and (3) gas-liquid-liquid flow. In gas-liquid flow, gas slugs are formed in a liquid such as air in water. In liquid-liquid flow, reagents are mostly in the aqueous phase (discrete), and they form droplets in the oil (continuous phase) due to shear force and interfacial tension [103,104]. Homogenous mixing can be achieved in multiphase flow microfluidics due to the same residence time and the same amount of mixing in each slug or droplet generated. The most extensively studied microfluidic device for NMs synthesis is the droplet generating devices (Fig. 2b) [104–106]. The droplet-based microfluidic devices can be achieved with three types of geometry; a T-junction, co-flow, and flow-focusing devices. The widely studied droplet-based device is a flow-focusing as it can generate droplets with the size same as an orifice [103].

NMs used in biomedical applications can be categorized into noble metal, silica, biopolymer, iron oxide, quantum dots, carbon-based, rare-earth-based, and other NMs. This section discusses the critical examples in controlled synthesis of each type of NMs using various microfluidic

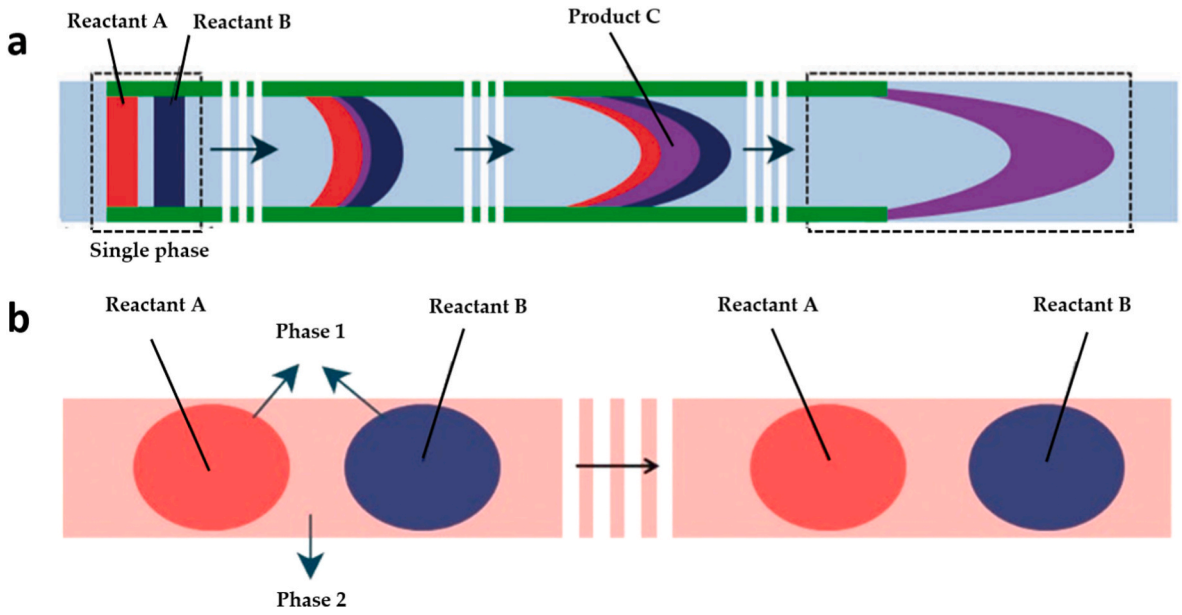

Fig. 2. Schematic representation of single-phase and multi-phase flow for NMs synthesis. **a)** Reactant A and B mix in single-phase due to diffusion and forms product C after covering lengthy channels. **b)** Multi-phase flow formed by aqueous droplets (Reactants A and B) as one phase and oil as another phase. Republished with permission [96]. Copyright 2011, Royal Society of Chemistry.

technologies with its latest trends. We emphasize microchannel geometry, materials for device fabrication, and tuning parameters for each category of NMs. Besides, each type of NMs' features that make them suitable for biomedical application is also explained.

2.1. Noble metal

Noble metal NMs include ruthenium (Ru), rhodium (Rh), palladium (Pd), silver (Ag), osmium (Os), iridium (Ir), platinum (Pt), gold (Au), and copper (Cu). Due to its high surface-to-volume ratio, these materials can be used as biomarkers by functional molecules such as antibodies and drugs. Moreover, the absorption and fluorescent properties of noble metal NMs are useful in protein detection using Surface-enhanced Raman scattering and fluorescent imaging [107]. In addition, it possesses natural grafting, x-ray absorption, shape-dependent localized surface plasmon resonance (LSPR), catalysis, and electrochemical properties [108]. When light having wavelength comparable with the size of NMs falls on it, electrons in NMs oscillate due to its size restriction. If the collective oscillation has a frequency same as that of the incident light, maximum absorption and scattering of light happens, known as LSPR. This property depends on the shape and size of the NMs, refractive index of the surrounding medium, and complex dielectric constant [107,109,110]. It gives rise to various features, including metal enhanced fluorescence, photothermal and photodynamic properties, Surface-enhanced Raman Scattering, and surface plasmon resonance [111–113].

Compared to other noble metals, Au and Ag NMs are commonly employed in biomedical applications due to their relative inertness and tunable plasmonic peak in the visible or near-infrared region [111]. Au NMs were investigated in detail and treated as a quintessential noble metal because they show exclusive features: ease of functionalization, non-toxicity, physiochemical, biological, and catalytic properties, and LSPR. These features make them useful in biomedical imaging, targeting, therapeutics, diagnostics, biosensing, and drug delivery [114–122]. On the other hand, Ag NMs exhibit macroscopic quantum tunneling, surface and volume effects, and quantum size features. These features make them suitable for biochemical sensors, chemical probes, antimicrobial material, anti-cancer material, DNA detection material, and drug carrier [123,124]. The final properties of the noble metal NMs for specific application entirely depend on particle size, distribution, morphology, composition, and surface modifications [67].

General synthesis of noble metal NMs is by reducing the metallic precursor (or ionic salt) with a reducing agent into atoms, which are insoluble in the solvent. Hence, they aggregate to form stable nuclei (known as nucleation), followed by the growth of nanostructures from the nuclei. Sometimes, surfactant (to reduce surface energy) and capping agent (to prevent particles' aggregation) are also used [125]. Hence, an ideal platform should control the reaction kinetics to produce desired noble metal NMs, and microfluidic technology offers the same. Microfluidic technologies for noble metal NMs synthesis are well established [67,126–128]. Microfluidic architectures, namely coaxial flow, coiled flow inverter, emulsion droplet, etc., were used to synthesize spherical structures [127,129–131]. Compared to spherical structures, non-spherical noble metal NMs have shown tremendous applications in the biomedical field. For example, Au nanostars or branched structures, nanorods, hollow NMs, nanocages, and core-shell NMs possess tunable plasmonic peaks that can be tuned to the near-infrared region, which is beneficial for photothermal and photodynamic therapy [132].

In a microfluidic platform, morphology, shape, material composition, size, and crystallinity of noble metal NMs can be tuned by adjusting the flow rate (or residence time), the molar ratio of reagents, temperature, pH, the geometry of the device, dimension, etc. Flow rate plays a vital role in controlling the size of noble metal NMs. A higher flow rate means a short time for nucleation; then, growth favors over nucleation, producing large particles [133]. Since nucleation is chaotic compared to growth, the mixing of reagents is more, leading to smaller NMs. A higher flow rate allows more reducing agents to be available; hence, the nucleation is more and growth step is suppressed [51]. Further, a higher flow rate favors less reactor fouling due to the higher shear force [134,135]. The effect of the reagents' flow rate ratio has been studied in detail. For example, the aspect ratio of Pd nanorod was increased by increasing the flow rate ratio (stabilizer plus reducing agent to precursor) from 0.25 to 1.8.In the case of monometallic NMs, precursor to reducing agent flow rate ratio can control the size distribution [136]. For monometallic NMs with monodispersed particle distribution, the precursor flow rate should always be higher than that of the reducing agent. With equal flow rate, synthesized NMs were small with narrow size

distribution. On the other hand, if the flow rate of the reducing agent is higher than that of precursor, synthesized NMs possess polydispersity due to the presence of aggregated particles. The reason might be the lack of precursor monomer to reach the supersaturation level arises with the formation of precursor-reducing agent complex [136].

The increase in residence time (or low flow rate) influenced the size and morphological evolution of Pd NMs in a single-phase microreactor. Pd nanocubes were grown into different shapes when the residence time was increased from 10 to 20 min [137]. Similar to the flow rate ratio, the molar ratio of precursors was used to control the size and shape of noble metal hybrid NMs. In an example, Pd–Pt core-shell NMs synthesis was controlled by tuning the precursor flow rate ratio; increasing the Pd/Pt ratio (1:1 to 6:1) increased the diameter of particles (28–31 nm), and morphology changed gradually from cubic wavy nature to spherical dendritic [137].

Highly monodispersed noble metal NMs synthesis requires precise control over temperature, mixing time, and reaction time. Temperature can control the reaction kinetics. At low temperatures, thermal energy is low; nucleation rate is low. Hence growth is higher, produces large-sized particles. In the case of Au NMs synthesis, higher temperature promotes the conversion of $[AuCl_4]^-$ into hydroxylated species, reactive species are converting to less reactive species, thereby terminating the nucleation period faster. Equilibrium shifts to more hydroxylated forms at a higher temperature. Also, the reduction rate of Au precursor increases at higher temperatures, resulting in a higher nucleation rate during a short time. Due to excess thermal energy available, the size of stable nuclei is more significant at higher temperatures. But increasing temperature beyond 80 °C, resulted in a slight increment in Au particle size [129]. Similar to temperature, higher heating time causes quick transfer of reagents, leading to the reduction of metallic salt. Hence aggregation of NMs is more [138].

To control the reaction kinetics precisely, many devices were designed to separate the nucleation and growth stages of NMs formation. It includes adopting different mixing geometries and employing a series of microreactors or using separate reaction zones for nucleation and growth [67,129]. Ag NMs of 5–8 nm were successfully synthesized in a series of microreactors, with the first reactor triggering nucleation with the help of a potent reducing agent and long residence time (~8 min). This avoids secondary nucleation in the successive reactors and produces highly monodispersed NMs [67]. Various strategies were employed in improving the mixing efficiency of reagents.; pulsating flow micromixing and static micromixer followed by T-junction are a few examples used to produce highly monodispersed Ag NMs [123,136]. An inverted helical flow mixing reactor was recently used to synthesize Ag NMs, enhancing radial mixing by promoting the Dean vortices under laminar flow [67]. The geometry helped to synthesize the monodispersed NMs with minimum agglomeration even in the absence of capping ligands. The growth stage of spherical noble NMs formation can be controlled by providing sequential addition of precursors due to their low diffusion time [67]. This was achieved in a conventional batch reactor by the dropwise addition, which generally results in concentration profiles across the reactors. A Series of microreactors in the growth stages with distributed feed at the inlet of each reactor can resolve this issue.

In 2016, Sebastian et al. fabricated a silicon-pyrex microreactor with separate mixing (cold) zone and reaction (hot) zone to withstand high temperature and pressure [139]. In the cold zone, reagents mix before reaction starts, which helps to produce monodispersed NMs by providing passive mixing and avoiding nucleation during the growth stage. A hot reaction zone can increase the solubility of gases in the liquid phase and can utilize water as a solvent at high temperatures. Also, after passing through the hot reaction zone, before collecting the particles, passes through the cold zone to quench further growth of NMs. Monometallic, bimetallic, and hybrid metallic nanostructures were synthesized in this device by varying the flow rate, temperature, and gas type. The synthesis method is based on the liquid-gas multiphase flow, where formed gas (Carbon monoxide, CO) slug act as reducing and capping agent, which helps to transport liquid-gas flow and promote homogenous size and shape distribution of NMs. Another advantage of this device is that it can easily switch from laminar to segmented flow and vice versa. Compared to laminar flow, segmented flow can promote crystallization kinetics by promoting the inter-phase mixing in the gas/liquid slugs formed in the spiral mixing area. CO as gas-phase produced anisotropic nanostructures due to preferential adsorption, while N_2 gas produced shapeless particles. Conventional reactors take several hours to synthesize Pt nanocubes, whereas segmented flow microfluidics took only 150 s to synthesize perfect cubic structures [139].

The latest trend in the controlled synthesis of noble metal NMs is that synthesis can be triggered with external energy sources (passive mixing) such as magnetic field, electric field, electromagnetic radiation, and ultrasound. For example, a droplet-based microfluidic device with embedded electrodes was developed to fabricate branched Au NMs with high reproducibility in a controllable manner (Fig. 3a) [105]. The polydimethylsiloxane (PDMS) based device has two nozzles; nozzle 1 generates droplets, followed by the winding channel to mix the reagents, electrodes are embedded in nozzle 2, where Au seed solution can be injected. By adjusting the mixing channel length between nozzle 1 and nozzle 2, and flow rates, the local concentration of reagents were varied between two nozzles. Electrodes were supplied by an electric voltage of 600 V, which destabilizes the droplets and provides sufficient Au seed (~15 nm) for the anisotropic growth of NMs. Hatton and co-workers employed a similar concept in producing Au–Pd core-shell NMs (10 nm shell thickness) [140]. Water-oil emulsion generates microdroplets in T and Y connectors in multiple sequential steps and is allowed to pass through a microchannel sandwiched between the electric field. Application of electric field with sufficient energy expands the droplet size rapidly (known as electrocoalescence), which helps subsequent addition of reagents in a controlled manner, thereby improving the mixing. The droplet size increased with increased electric field intensity (4300 V/cm to 11400 V/cm) and with residence time (controlled by the tube length). Hence, for higher electrocoalescence to promote reagent mixing, electric field intensity should be high for a specific residence time. Also, beyond 11000 V/cm, there was no significant change in expansion of droplet size. Three step synthesis procedure has been reported in synthesizing Au–Pd core shell NMs. If the electric field signal is burst type such as on-off signal, electrocoalescence rate can be increased by increasing the number of on cycle or the duration of on cycle [140]. In another device, microwave heating induced temperature was employed to produce Ag NMs and observed that it is more favorable for NMs formation than conventional heating [100]. The temperature profile varied in the microchannel due to the distribution of the electromagnetic field. The channel's average temperature decreased with increasing the flow rate due to the substantial temperature reduction at a high flow rate.

Multiple components can be integrated on a single microfluidic chip to accelerate the synthesis of NMs. It can also help control and monitor reaction parameters, including residence time, droplet size, photoluminescence, absorbance, etc., that are crucial for reducing errors during synthesis and increasing the production of homogenous materials. Weng et al. successfully synthesized hexagonal Au nanostructures in a microfluidic chip, consisting of a micromixer, micro-pumps, microvalves, micro heaters, and micro temperature sensor [138]. Integrated microfluidic devices provide automated control, which minimizes user dependency. Similar to components, multiple steps in synthesis such as sample preparation, reaction, and detection can also be integrated into one device to allow massively parallel analysis and increase the device's throughput.

More details about the controlled synthesis of noble NMs using microfluidic devices are explained in Table 1. It is observed that the majority of noble metal NMs are synthesized using segmented flow devices than continuous-flow devices. It might be because mixing efficiency is higher with segmented flow devices, enabling more control of parameters than continuous flow. Further, particle clogging is often

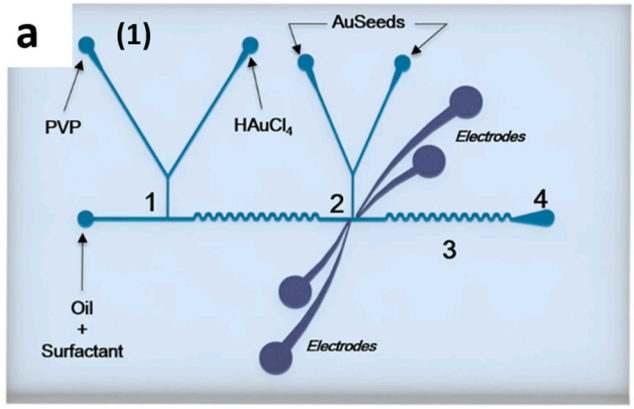

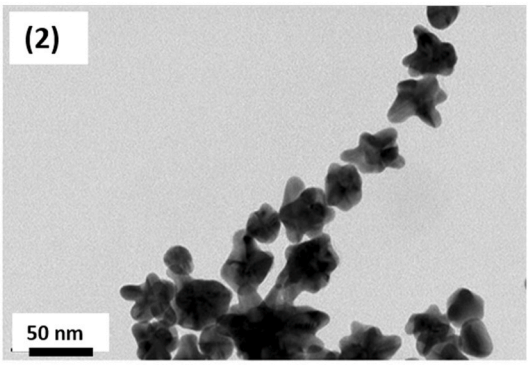

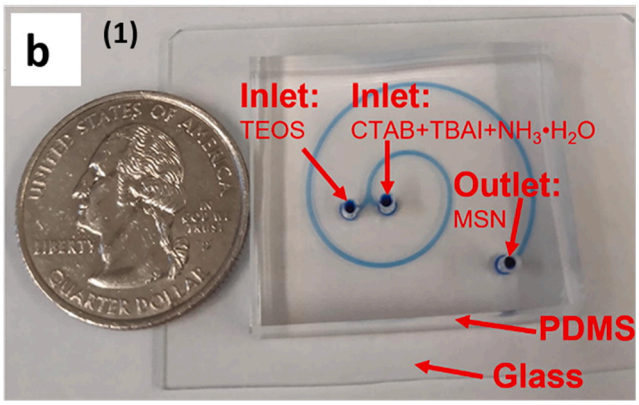

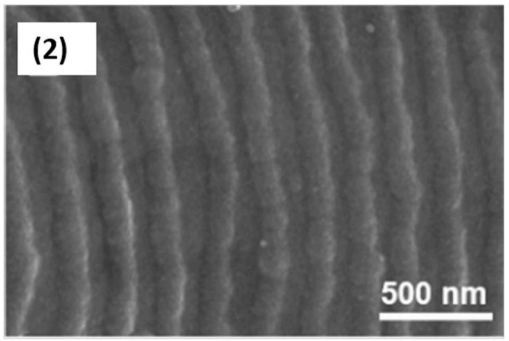

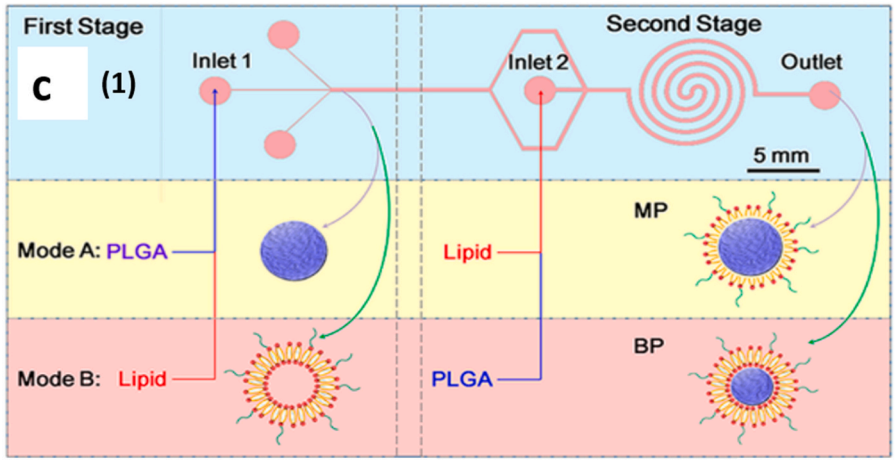

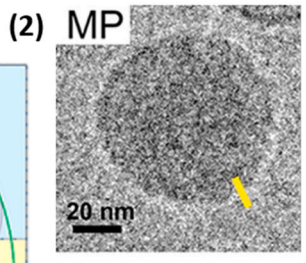

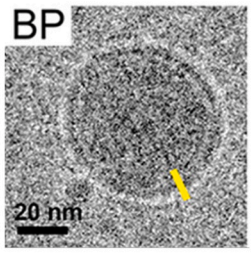

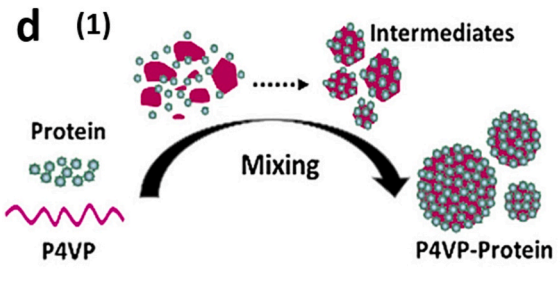

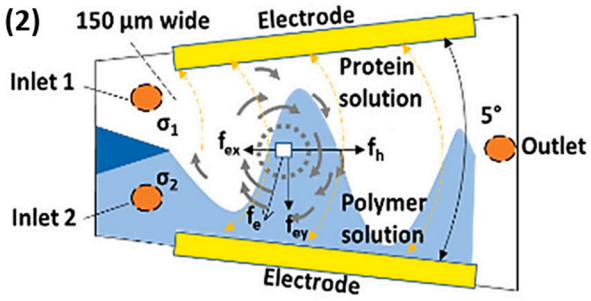

(caption on next page)

Fig. 3. Microfluidic systems for synthesizing noble metal, silica and biopolymer NMs. **a)** (1) Schematic drawing of PDMS based droplet microfluidic device with external electrodes to synthesize branched Au NMs and (2) TEM image of synthesized NMs. Reproduced with permission [105]. Copyright 2018, Nature. **b)** Spiral-shaped microfluidic device to synthesize silica NMs. (1) Photograph of the two-run spiral device to synthesize mesoporous silica nanosheets and (2) corresponding generated NMs. Reproduced with permission [151]. Copyright 2019, Elsevier. **c)** Formation of polymer-lipid NMs with monolayer or bilayer lipid shell (MP or BP) using PDMS based microfluidic device. (1) Schematic illustration of the two-stage device with two modes; Mode A synthesize MP and mode B for BP. (2) TEM images of MP and BP. Reproduced with permission [154]. Copyright 2015, American Chemical Society. **d)** Formation of polymer-protein assembly using electrokinetic flow: (1) Schematic illustration of the process and (2) Illustrative drawing of the entrance of microfluidic device, where σ_1 and σ_2 are electrical conductivity of fluids from inlet 1 and inlet 2 respectively, f_h is the hydrodynamic force, f_e is electrical body force with x-component f_{ex} and y-component f_{ey}. Reproduced with permission [155]. Copyright 2020, Elsevier. TEM-Transmission electron microscope; PVP-Polyvinylpyrrolidone; $HAuCl_4$-Gold salt; TEOS-Silica precursor. (For interpretation of the references to color in this figure legend, the reader is referred to the Web version of this article.)

observed in the microfluidic channel, requiring surface modification of channels in noble metal NMs synthesis. In addition, the majority of noble metal NMs synthesis is carried out at a specific temperature. Hence the device material should be thermally conductive.

2.2. Silica

Silica NMs are one of the most promising NMs in the biomedical field. It is widely used as drug and gene delivery vectors, drug coadjutants, fluorescent probes for bioanalysis, bio-separation, etc. [35,68,141–143]. It possesses unique properties such as high loading efficiency as a nanocarrier, biodegradability, biocompatibility, and high functionalization based on silane ligand's condensation on surface silanol groups [108]. Generally, silica NMs are synthesized using a sol-gel process, known as the Stöber process, or its modifications. It consists of hydrolysis, condensation, nucleation, and growth steps. Thus, controlled synthesis of silica NMs requires fine-tuning of reaction parameters in these steps [102,144,145]. The hydrolysis process is slow compared to condensation, so an alkyl or acidic catalyst is usually used to enhance the hydrolysis rate [146]. The addition of water, temperature, and catalyst can control hydrolysis and condensation, eventually into the controlled material synthesis.

Among all the silica NMs, solid spherical, mesoporous, core-shell, hybrid, and hollow nanostructures are essential in biomedical applications. Solid spherical silica was synthesized in geometries such as conventional flow-focusing, a combination of winding channel and T-junction, and baffling micromixer. Baffling micromixer fabrication is easy and provides sufficient mixing at low and high flow rates, and controlled silica NMs synthesis was achieved at a low cost [146]. The device has three mixing units; each contains a gap followed by a baffle as an obstacle. The best mixing efficiency was achieved with a gap size of 50 μm at Reynolds number less than 0.1 due to molecular diffusion and at Reynold number greater than 40 due to the formation of more energetic vortices. Some of the microreactors have separate tubings to provide sufficient residence time for the hydrolysis and silicification process. The effect of mixing geometries on silica NMs formation has been studied in detail. For laminar flow, mixing in the T mixer is better than slit interdigital mixing due to the longer diffusion time in slit interdigital due to fluid shift towards the wall. Wall deposition was often observed in solid silica NMs, which can be avoided by adopting Taylor flow for internal mixing [145]. Within laminar flow, particle size can be controlled by tuning the tube diameter; particle diameter increases with increased tube diameter. Small tube size leads to small axial dispersion, thereby producing small particles [147].

As explained for noble NMs, the temperature can control the silica NMs synthesis; temperature changes may bring phase transition due to its dependence on hydrolysis rate; hydrolysis rate of precursor halves with each 25 °C rise in temperature. At the same time, while synthesizing ordered mesoporous silica, mixing at low temperature produced hollow NMs. At 0 °C of the mixing temperature, the hydrolysis rate of the precursor was poor; the initial mesophase became unstable, a phase transition occurred within the worm-like micelle to stabilize the emulsion. Again, in the aging section at a higher temperature, the precursor hydrolysis rate is higher, forming thin mesophase structure skin. Also, lowering the temperature reduced the yield of production [145]. Apart from the shape, high temperature can reduce the particle size also. As temperature increases, the hydrolysis rate of precursor increases, which reduces the OH^- concentration, nucleation is favored than growth, hence the size decreases. Like temperature, longer reaction time favours growth process rather than nucleation, thereby producing large particles [146].

Flow rate has the same impact as the temperature in silica NMs; as flow rate increases, size decreases, and size distribution becomes narrow. At a low flow rate, the pressure difference between the central point and wall of the stream is low. The pressure difference enhances the shear stress and creates an extra force in the central stream, which drives the reagents close to each other. Higher pressure difference at a higher flow rate ratio leads to higher force in the central stream, causing the molecules to be significantly closer. There is a limit value for maximum flow rate ratio; beyond that, particle size distribution is broader. Narrow particle size distribution was observed for a flow rate ratio of 15–45 [148]. Flow rate can also control the morphological evolution in anisotropic silica structures; decreasing the flow rate of silica precursor leads to longer surfactant micelles, resulted in higher aspect ratio nanofibers. This can also be achieved with a higher flow rate of surfactant. On the other hand, increasing the flow rate of precursor produced lower aspect ratio nanofibers until it becomes spherical. Flow rates of surfactant and catalyst (ammonia) have an inverse effect; longer aspect ratio nanofibers were produced at a higher flow rate while spherical shapes evolved at a low flow rate [26]. The effect of flow rate on morphological evolution during solid ellipsoidal silica into hollow ellipsoidal silica conversion has been explored. A low flow rate indicates a higher etching rate; particles might be etched partially and produce irregular pieces. As flow rate increases, etching rate decreases, and found that flow rate corresponds to 1000 μL/min can maintain the shape of ellipsoidal mesoporous silica with fine etching [149].

The catalyst concentration can control the size of particles; an increase in the catalyst amount favors hydrolysis reaction, which promotes nucleation compared to growth; hence particle size increases [146]. Increased precursor and catalyst concentration and the addition of water favors faster hydrolysis, resulting in an increased number of monomers, which promotes nucleation than growth, thereby increasing the particle diameter (sphere), aspect ratio, or thicker nanosheet silica [26,144,146,150,151].

Among all the geometries, single-phase continuous flow spiral-shaped microchannels (Fig. 3b) were able to fabricate silica NMs in various shapes, including mesoporous nanofibers, 2D hollow sandwich like mesoporous nanosheets, functional hollow sphere, hollow ellipsoidal mesoporous, and triangular Ag-silica core-shell NMs [68]. Transverse Dean flow (flow in curved pipes and channels) provides sufficient rapid mixing of reagents in spiral geometry. To obtain different morphology, microchannels' dimensions (number of turns, width, height and length) were varied. With five turns-spiral microreactors, ellipsoidal mesoporous silica was converted into a hollow mesoporous structure within ~4 s [149]. The conventional batch reactor requires ~18 h for this conversion [26].

Silica-based plasmonic nanoshell attracted photothermal cancer therapy, drug delivery, biosensing, and diagnosis [152]. Multiple Y-junction micromixers, split interdigital micromixers, and laminar flow microreactors were employed to produce silica-titania, silica-Au

nanoshell, and cobalt oxide-silica core-shell NMs, respectively [68]. Recently, a 3D printed multistage cascaded microreactor was developed to synthesize silica-based hybrid NMs [150]. The first reactor synthesized silica NMs, and functionalization with polyethyleneimine (PEI) was performed in second and third reactors, followed by capping with gluconolactone (GLU) in the fourth reactor. The reactors were equipped with a magnetic stir bar in each chamber and thermocouple to ensure sufficient mixing and temperature control. Residence time distribution was found to match with an ideal reactor, which helped to synthesize particles with narrow size distribution [150]. Apart from synthesizing monodispersed silica NMs, the surface charge can be controlled in microfluidics by tuning the residence time and concentration. As an example, zeta potentials of silica NMs were tuned from -40.2 ± 1.3 mV to +31.5 mV (PEI-Silica) and +8 mV (GLU-PEI-silica) by varying the concentration of silica NMs, PEI and GLU, and its molar ratio as well as residence time (8–16 min) [150]. In another recent work, a specially designed microfluidic device with capillary and PDMS membrane was used to assemble Ag NMs on a silica shell in a 3D extended array [153].

Detailed information about the tuning parameters in controlled synthesis of silica NMs is listed in Table 1. Flow rate and molar mass ratios are the major tuning parameters to control the size and shape of simple and silica-based hybrid NMs. Inline control for real-time analysis is not so developed for silica NMs. If it can be achieved soon, automated synthesis is possible.

2.3. Biopolymer

Biopolymer NMs are a promising nanomaterial in several biomedical applications due to their easy functionalization, drug encapsulation, biodegradability, biocompatibility, and versatile design [108]. It includes lipopolyplex, small interfering ribonucleic acid (siRNA) containing lipid NMs, cubosomes, liposome, poly lactic-co-glycolic acid (PLGA) NMs, chitosan, polyester, liposome hydrogel, lipid, lipid quantum dots, lipid polymer hybrid, natural membrane coated polymer, and leukocyte mimicking NMs [156].

The most common method of synthesizing a biopolymer is nanoprecipitation (formation of NMs from the solution as precipitates), adapted in the microfluidic environment. The standard device material for biopolymer NMs synthesis is the PDMS due to its biocompatibility and transparency. Fabrication of highly monodispersed polymer NMs requires higher mixing efficiency. Hence, there have been a variety of microfluidic geometries emerged to improve the mixing efficiency to synthesize various biopolymer NMs; staggered herringbone mixing to produce cubosomes [34], 3D glass capillary co-flow nanoprecipitation device to make PLGA, hydrophobic chitosan, and acetylated dextran NMs [157], hydrodynamic flow focusing nanoprecipitation for fabricating polyethylene glycol (PEG) hybrids [39], 3D hydrodynamic flow focusing for producing liposome [77], and combinatorial synthesis embedded into 3D hydrodynamic focusing to synthesize targeted polymer hybrid for cancer therapy [158], etc. Polymer NMs are combined with lipid particles to enhance drug encapsulation, efficiency, stability, prolonged circulation half-life, and improved cellular uptake [154]. Also, polymer NMs are often coated with natural membranes [159]. These polymer-lipid hybrid and polymer-natural membrane hybrids are prepared by two methods; (1) one-step method and (2) two-step method. In the one-step approach, polymeric NMs are prepared initially, and lipid shell forms simultaneously as self-assembly. Zhang et al. developed a two-stage PDMS-based microfluidic chip (Fig. 3c) to synthesize polymer-lipid NMs with monolayer or bilayer lipid shells [154]. For monolayer formation, PLGA was introduced in inlet 1 of the first stage to form PLGA NMs, and lipid was introduced in inlet 2 of the second stage to create a monolayer of lipid shell. For bilayer formation, lipid was introduced in the first stage, surrounding the PLGA in the second stage. Spiral geometry in the second stage is the crucial structure for bilayer formation. On the other hand, the two-step synthesis method produces polymer NMs and aqueous lipid/natural materials separately, followed by assembling the NMs in the second step with the help of external energy (such as sound, extrusion, etc.). Recently, an electrokinetic flow-based microfluidic device (Fig. 3d) was developed to synthesize polymer-protein assembly [155]. In the initial stage, the polymer and protein stream in ethanol meets in the microchannel and forms the large droplets; with the application of electric field, formed droplets break up, which improves the mixing and assemble the polymer-protein. Further, microfluidics was employed in synthesizing tunable rigidity and acid-switchable surface charge with PLGA core NMs to overcome multidrug resistance, which was the key reason behind the failure of chemotherapy [160].

Flow rate and molar ratio control the size and size distribution of polymer-protein assembly [155]. In general, the Poly dispersity index (PDI) of particles decreases with increasing flow rate and is always lower than the conventional batch method. However, in the electrokinetic microchannel with the electric field application, the PDI of particles synthesized at a low flow rate (2 μL/min) is lower than that of particles prepared at a high flow rate (10 μL/min). It might be due to the reduced mixing as the flow rate increases in the electric field. By keeping the flow rate constant, changing the molar mass ratio can tune the size of the polymer-protein assembly. Increasing the protein-polymer mass ratio (1:8 to 1:0.08) resulted in increasing the particle size (284–925 nm) due to the availability of polymer in large quantities.

Cubosomes are lipid-based NMs consisting of lipid membranes that intertwine into complex arrays of pores well-ordered in a cubic lattice. Reaction time is an essential factor in deciding the well-ordered cubosomes structure. Successful cubosomes synthesis was carried out in a staggered herringbone microfluidic device within 14 min of reaction time [34]. Increasing the amount of stabilizer can elevate the size (75 nm) of cubosomes without compromising the ordering of bicontinuous cubic membrane. Since the stabilizer cap on the formed NMs, size cannot increase further, which is helpful for biomedical applications as the size window for successful therapeutic purposes is 5–100 nm.

The controlled synthesis of above-mentioned biopolymer NMs is summarized in Table 1. Most of the biopolymer NMs synthesis uses PDMS microfluidic devices, and the flow behavior is continuous. Flow rate and molar ratio are tuned to achieve the controlled synthesis of biopolymer NMs in microfluidic devices and is well established.

2.4. Iron oxide

The iron oxide NMs possess various properties; paramagnetism, superparamagnetism, thermal and electrical conductivities, size-dependent magnetic properties, and hyperthermia (magnetic heating) [108]. These NMs are considered the right candidate for magnetic resonance imaging (MRI). By combining the iron oxide NMs with other nanostructures such as noble metal, silica, or polymer, formed hybrid structures can be used for targeting, drug delivery, and hyperthermia treatment [88].

Synthesizing iron oxide NMs for biomedical application is difficult, even though they are readily available in the form of rust. Iron's reactivity is a dominant factor that concerns nanoscale level and found that it is pyrophoric if finely divided. The extreme reactivity of iron oxide NMs makes it challenging to study and unsuitable for applications [163]. The coprecipitation method is generally used to synthesize iron oxide NMs, and the reaction temperature is often tuned to control the synthesis process. The quality of synthesized NMs depends entirely on how fast iron precursor and alkaline solution mix. As the microfluidic systems provide rapid mixing of reagents and controlling the temperature is possible, iron oxide NMs can be easily synthesized in a microfluidic platform. However, most of the studies were not paid much attention to the reactivity of iron oxide NMs. Also, various hydrophilic ligands have been used to make iron oxide NMs soluble in an aqueous solution. In microfluidic-based synthesis, surface ligands modification has been achieved successfully, and their performance is enhanced for biomedical applications.

Table 1
Summary of information about controlled synthesis of various NMs using microfluidics.

Composition	Shape	Size (nm)	Reagents	Device Geometry, Material & Dimension	Tuning Parameters	Ref.
Ag	Sphere	5–80	$AgNO_3$, NaOH, trisodium citrate, BSA, $NaBH_4$ & HNO_3	Series of microreactors; T-shape mixers; PFA tubing coiled on an inverted flow helical 3D printed frame; length 3 cm i.d.xo.d.:1/16 × 0.03 in.	Seed to growth ratio (4–40 seed diluted), number of growth reactors (1–5), residence time (0–40 min), pH (5.6–12.5) & precursor concentration (1–4 mM)	[67]
Au	Star	–	Trisodium citrate, $HAuCl_4$, HCl, $AgNO_3$, PVP, HFE-7500 & DMF	T-junction, zig zag microchannel and electrodes; PDMS; Width 80 μm Height 75 μm Length 3.29 mm	Presence or absence of surfactant (PVP)	[105]
Ag	Sphere	19 ± 4.3	$AgNO_3$, PVP & Ethylene glycol	Y-mixer & microwave heating helical reactor; PTFE tubing; 0.3875 × 1.5875 mm (i.d. x o. d.) Length 77 cm	Flowrates (0.1–0.6 mL/min)	[100]
Ag	Sphere	5 ± 2	$AgNO_3$, $NaNO_3$, $NaBH_4$ & NaOH	Jet mixing reactor; PEEK cube consists of 3 cylindrical channels; 1.02 mm (main channel), 0.51 mm (other)	Ratio of capping agent and reducing agent concentration (0.1–1000) & sample collecting time (10–55 min)	[175]
Au	Sphere	<5	HAuCl4, TOAB, toluene, $NaBH_4$, Na_2SO_4, DMAP	T shaped micromixers of PEEK, mixing coil and split and recombine micromixer of PTFE; Length 10 m (first stage and 5 m (second stage) & split and recombine; width 300 μm Depth 100 μm	Flow rate ratio (1:1, 2:1 & 4:1 TOAB-Au: DMAP)	[176]
Au	Rod	5.1 ± 0.3 (aspect ratio)	CTAB, $HAuCl_4$, $AgNO_3$, L-ascorbic acid, PEG-methyl ether thiol & hydrogen tetrabromoaurate (III) hydrate	Multiple Y shaped junctions; PTFE tubing and PEEK Y junction; 1.016 mm (i.d.)	Halide anions (Br, I, Cl) & seed aging time (2–125 min)	[177]
Pd Pd–Pt	Nanocubes Core-shell nanocubes	14 ± 1.6 28 ± 4.2	Palladium (II) chloride, hydrogen hexachloroplatinate(IV), L-ascorbic acid & CTAB	PEEK Y-junction and PTFE coiled tubing; i.d. 800 μm & length 4.2 m	Residence time (2–30 min), temperature (60–130 °C), concentration of surfactant (4.17–37.5 mM CTAB) and precursor & molar ratio (6:1–1:1)	[137]
SiO_2 Magnetic SiO_2 SiO_2-QD SiO_2–Ag NPs	Hollow sphere with sponge like porous shell	100 (pore size) 1254 ± 237 (sphere)	CTAB, TMB, TEOS & NH_4OH	Spiral shaped microchannel; PDMS; Width 500 μm Height 50 μm Diameter of spirals 7.69, 13.8 & 22.2 mm	Reactant concentration (0–1500 mM TMB, 5.5–41.1 mM CTAB, 0.28–2.1 M ammonia) & flow rate (50 μL/min- 5 mL/min)	[178]
Ag@ SiO_2	Triangular core shell (excessive) sphere	10 (coating thickness)	$AgNO_3$, TSC, H_2O_2, $NaBH_4$, TEOS & NH_4OH	2 loop spirals; PDMS; Width 500 μm Height 50 μm, Diameter 7.69, 13.8 and 22.2 mm	Concentration of reagents ($AgNO_3$, TSC, H_2O_2, $NaBH_4$) & flow rate of catalyst (0–400 μL/min)	[99]
Mesoporous SiO_2	2-D nanosheet	100 (thickness)	TEOS, CTAB, ethanol & NH_4OH	Spiral shaped microchannel; PDMS; Width 500 μm Height 50 μm Diameter 7.69, 13.8 & 22.2 mm	Concentration of reagents (2.5–40 mM CTAB, 7.5–120 mM ammonia, 45–720 mM TEOS) & flow rate of TEOS (25–100 μL/min)	[151]
Lipid-PLGA	Core-shell; bilayer and monolayer lipid	103.67 ± 8.51 (monolayer) 106.43 ± 6.75 (bilayer)	DPPC, cholesterol, DSPE-PEG2000, NBD-DSPE & PLGA	Straight channel and double spiral mixing; PDMS; width 300 μm Depth 20 μm 3 loops in counter clockwise, changes direction and rotates in clockwise	Reagent injecting order	[154]
Polymer-protein assembly	Core-shell	433-453 (average)	P4VP, p-aminophenol, phenazine methosulfate, NADH sodium salt, BSA & EGFP fluorescent protein	Electro kinetic flow; quasi-T-shaped; acrylic plates, Au chips, Teflon membrane & PTFE sheets; Length 5 mm Width 150 μm Height 230 μm	Mass ratio (1:8, 1:0.8 & 1:0.08) and flow rate (1–10 μL/min)	[155]
Cubosomes Cuboplex	Core-shell	<100	Glycerol monooleate, PEGylated GMO, DOTAP,		Reaction time (0–14 min)	

(*continued on next page*)

Table 1 (*continued*)

Composition	Shape	Size (nm)	Reagents	Device Geometry, Material & Dimension	Tuning Parameters	Ref.
				Y-junction and herringbone structured microchannel; PDMS;		
Iron oxide-silica	Core-shell	~50	APTES, iron oxide, TEOS, RITC & NH_3	Series of 3 coaxial flow devices; PDMS	–	[88]
Iron oxide- Au assembly	Core (rod)-shell	69 ± 5 (Au); 8.7 ± 0.5 (iron oxide)	Peptide D1, Au nanorod & iron oxide NMs	Y type micromixer and bend lengthy channels; PDMS; width 513 μm Height 136 μm	Flow rate ratio (0.1, 1, 10)	[165]
Iron oxide-Au	Core-shell	13.1 ± 2.5	$FeCl_3{\cdot}6H_2O$, $FeCl_2{\cdot}4H_2O$, ammonia, mineral oil & $HAuCl_4$	Capillary droplet reactor; Tygon tubing; i.d. x o.d.: 0.51 × 1.52 nm Fused silica capillary; i.d.xo.d.:100 × 360 μm	Precursor flow rate (5–25 μL/min)	[66]
RBC-iron oxide	Core-shell	~80 (core) ~9.4 (shell thickness)	Mouse RBC, iron oxide, uranyl acetate, PBS & FBS	Y-shaped merging channel, S-shaped mixing channel & electroporation zone; PDMS;	Pulse voltage (20–70 V), voltage duration (50–300 μs) & flow rate (10–50 μL/min)	[166]
QD-DNA-MB	Hybrid core-shell	–	QDs, MB, Sodium tetraborate, tris(2-carboxyethyl) phosphine hydrochloride, L-gluta-thione, tetramethylammonium hydroxide, tris-borate buffer & oligonucleotide	2 parallel droplet generator meets in a T-junction followed by serpentine channel (30 turns); PDMS; Width: 300 μm, height: 100 μm, length between junctions: 900 μm, droplet transportation channel: 25 mm, oil bridge: 100 μm width & 2600 μm length	–	[162]
CNT	3D closed cellular network	~400 (thickness)	H_2SO_4, CNT, HNO_3, EDC, hydrochloride, toluene, nitrogen gas, PVA	Co-flow and flow-focusing geometry; Glass capillary; i.d.xo.d.:0.58 × 1.00 mm & square capillary; i.d. 1.05 mm	Flow rate; oil phase (500–4000 μL/h) & Aqueous phase (20–280 mL/h)	[172]
CQD-PLGA	Core-shell	100–150	Azithromycin dihydrate, tobramycin, heptafluorobutyric acid, PLGA, trifluoroacetic acid, acetonitrile, HEPES, $(NH_4)_2SO_4$, KCl, NaCl, & KH_2PO_4	Microvortex device	Flowrate of reagents	[170]
CdSe QDs CdSe@ZnS QDs	Sphere	4.35–6.14 8.15	CdO, selenium powder, ethyl ziram, OA, OLA, ODE, TOP, TBP, Cs_2CO_3 & $PbBr_2$	Dual channel Y-type microfluidic chip & ferruginous pipeline; Diameter: 400 μm; Heating length: 800 mm	Flowrates (5–25 mL/h) & Reaction temperatures (210–290 °C)	[169]
lipid/PCL-PEI/siRNA	Core-shell	120.2 ± 1.4	Polyethyleneimine-graft-polycaprolactone, Cholesterol, 1,2-distearoyl-sn-glycero-3-phosphoethanol-amine-N- [methoxy (polyethylene glycol)-2000, DMSO	Spiral mixing (double spiral, 5 loop each); PDMS; Width 300 μm Depth 60 μm	–	[33]
F127-stabilized MAG-DHA	Hexosome	108–138	Docosahexaenoic acid monoglyceride, Pluronic F127, PBS & ethanol	Hydrodynamic flow focusing; Polyimide; 90 × 125 μm^2 & length 9 cm	Total volumetric flow rate (50–150) & flow rate ratio (10–40)	[78]
Superparamagnetic iron oxide	Sphere	2.3 ± 0.6 to 3.4 ± 0.6	Iron (III) acetylacetonate, triethylene glycol, absolute ethanol, ethyl acetate & hydrochloric acid	Mixing zone of meandering channel & reaction zone of spiral geometry; stainless steel; Depth 150 μm Width 370 μm Volume 160 μL	Flow rate (250–1000 μL/min)	[179]
Polymer	Sphere	67–1127	PEG-PPG-PEG, ethanol & milli-Q water	Co-flow mixing; Glass capillary; 1 mm (o.d. of inner capillary) 1.1 mm (i.d. of outer capillary)	Reynolds number (20–200), flow rate ratio (5.5–330 mL/h), order of injection & tip size of inner capillary (20, 150 & 680 μm)	[87]
UiO-66	3D porous	80–110	$ZrCl_4$, DMF, H_2bdc,	T-mixer followed by coiled micro capillary; i.d. 0.8 mm	Flow rate (0.1–0.5 mL/min)	[171]

Earlier, iron oxide NMs were synthesized using continuous flow microfluidics, and later onwards, functionalization of NMs was also achieved within a single device. Microreactors were combined or coupled to assemble NMs with multifunctional architecture for biomedical applications. In 2009, Abou-Hassan et al. fabricated fluorescent core-shell iron oxide-silica NMs (~50 nm) by connecting three PDMS-based coaxial flow microreactors in series; microreactor1 (at 50 μL/min) for grafting amine-containing molecule on iron oxide NMs, microreactor2 (at 100 μL/min) mixes these complexes with silica precursor (+fluorescent dye) and microreactor3 (at 200 μL/min) coat the iron oxide-amine complex with silica NMs (Fig. 4a) [88]. Synthesized materials were aggregated because silica NMs were not functionalized, and the whole process took only 7 min, whereas conventional batch synthesis takes ~24 h for the coating process. A similar concept was implemented by Hassan et al. to synthesize multifunctional silica-Au-iron oxide NMs by assembling fluorescent silica-Au (186 ± 3 nm) nanostructures and iron oxide NMs (16.5 ± 3.3 nm), using two continuous glass microreactors [164]. Residence time played a

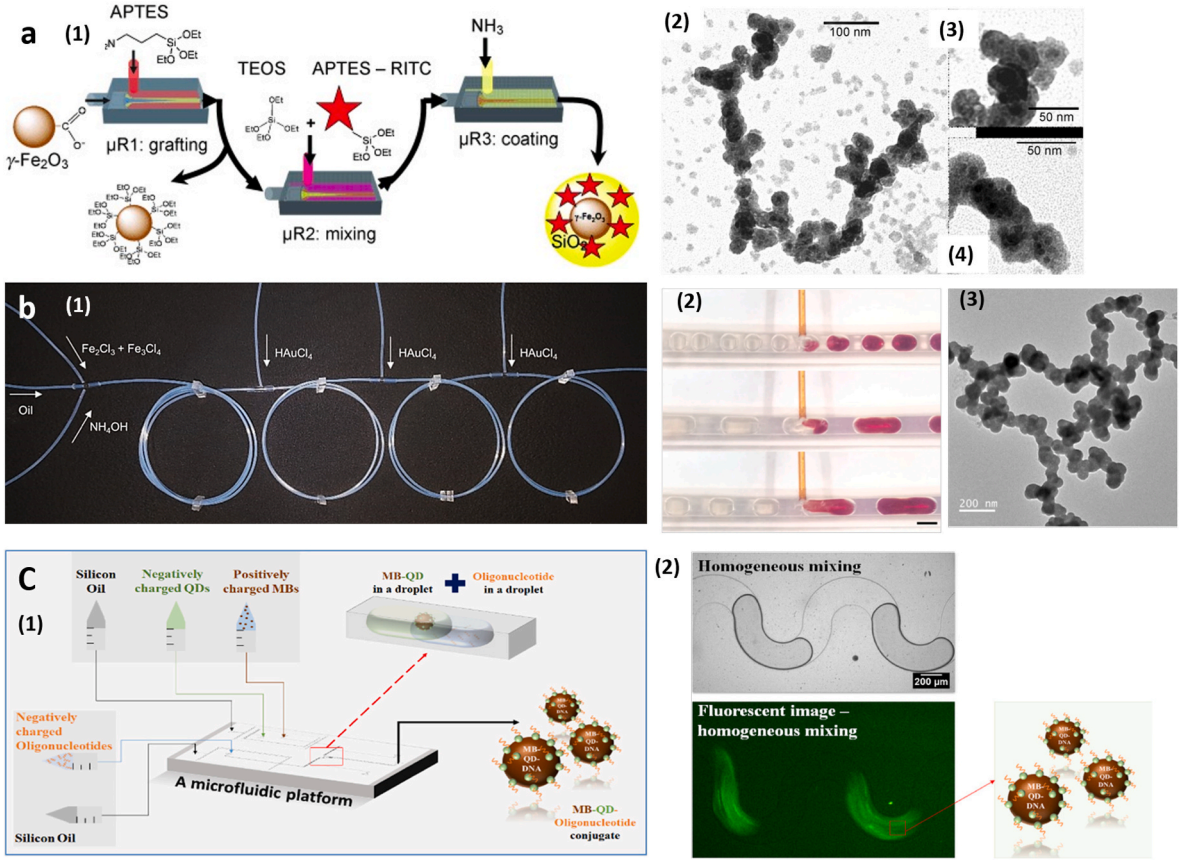

Fig. 4. Microfluidic platform to synthesize iron oxide and QDs based nanohybrids. a) Cascaded microfluidic device for synthesizing fluorescent iron oxide-silica core-shell NMs. (1) Schematic illustration of the synthesis, microreactor1 for grafting APTES on γFe_2O_3 NMs, microreactor2 mixes with silica precursor and microreactor3 coat silica on γFe_2O_3 NMs. (2) TEM images of synthesized particles, (3) and (4) are enlarged of (2). Reproduced with permission [88]. Copyright 2009, Wiley-VCH. **b)** Simple glass capillary (Tygon) network to synthesize iron oxide-Au core-shell NMs through multi-stage reagent addition. (1) Photograph of the microreactor. (2) Photograph showing the droplets at the injecting junction, red color indicates the mixing of Au precursor with potassium cyanide solution for illustration purpose (scale bar is 1 mm). (3) TEM image of NMs synthesized at Au precursor flow rate of 20 μL/min. Reproduced with permission [161]. Copyright 2020, Nature. **c)** Synthesizing QDs-based biomimetic NMs. (1) Schematic diagram representing the droplet-based microfluidic platform for fabricating magnetic bead-QDs-oligonucleotide conjugate. (2) Images showing chaotic mixing of reagents inside the droplets to immobilize the oligonucleotide. Reproduced with permission [162]. Copyright 2020, American Chemical Society. Rhodamine B isothiocyanate (RITC); (3-Aminopropyl) triethoxysilane (APTES). (For interpretation of the references to color in this figure legend, the reader is referred to the Web version of this article.)

significant role in controlling the assembling of hybrid NMs. It has been observed that the attachment of iron oxide NMs on silica-Au structures entirely depended on the residence time. Later, the same group assembled the peptide-functionalized magneto-plasmonic NMs of various structures using a single microreactor (Y-shaped mixing geometry) by controlling the flow rate ratio of reagents [165]. As the iron oxide to Au nanorod flow rate decreased, clusters of iron oxide NMs' size decreased and they were more localized on Au nanorod.

Recently, Ahrberg et al. showed that using a simple glass capillary droplet multistep microreactor (Fig. 4b (1)), iron oxide-Au core-shell NMs can be synthesized in single-step [161]. The first capillary junction generates droplets from the iron precursor, and the subsequent junctions are used to inject the Au precursor solution. The droplets can be easily visualized (Fig. 4b (2)), and the process can be monitored by integrating transmission measurement unit, which can further automate the process. The flow rate of injecting precursor solution was found to impact droplets' size; higher flow rate produced droplets with the larger size, but beyond 30 μL/min, secondary droplets were observed near the second junction. Also, thicker Au shells were observed with an increasing flow rate. This simple reactor's advantage is that it does not require any clean room environment to fabricate the device. Also, multiple reagents can be injected anywhere in the tubing, followed by a coiled network to promote sufficient mixing. Biomimetic NMs containing iron oxide NMs are essential in biomedical applications due to their superior biochemical properties. It can be easily fabricated using external energy-triggered microfluidic devices. For example, electroporation (generation of cell membrane pores by the application of electric field) facilitated microfluidic device was used to synthesize red blood cells (RBC) membrane vesicle coated iron oxide NMs (~80 nm). Electric energy generates membrane pores in the cell membrane and facilitates the easy entry of NMs [166]. Pulse voltage, pulse duration, and flow velocity can influence the synthesis. Complete cell membrane coating was achieved at pulses of 50 V with 200 μs duration at 200 μL/min flow rate.

Details of tuning parameters and controlled synthesis of iron oxide NMs are listed in Table 1. The flow rate ratio of the precursor is a dominant tuning parameter that controls the shell thickness, attachment of particle on core, and overall size of iron oxide-based hybrid NMs. Here, we discussed only hybrid NMs due to their dominance in biomedical applications. Earlier, cascaded connections of microfluidics were used to obtain the iron oxide-based hybrid structures; later, they started to fabricate in a single device, and nowadays it uses external energy sources to fabricate these structures, which gives more control over the reaction parameters. However, if the microfluidic chip develops iron oxide NMs alone, the reaction temperature is significant. Hence, the materials used to construct the microfluidic chip should be thermally conductive and withstand high temperatures. Further, none of the work studied the reactivity of iron oxide NMs.

2.5. Quantum dots

Quantum dots (QDs) are semiconductor NMs, possess shape and size-controlled photoluminescence properties [108]. They are useful in drug delivery, gene therapy, *in vivo* imaging, cell tracking, fluorescent labeling of cellular proteins, tumor investigation, and toxin and pathogen detection. QDs possess unique properties like tunable size, long lifetime, brightness, narrow luminescence, low autofluorescence, and absorption. Its brightness is 20 times higher, and stability against photobleaching is 100 times higher than organic dyes, which makes their sensitivity and repeatability higher in complex sample analysis [167,168]. The QDs' surface modifies with various molecules including carbon allotropes, upconversion NMs, metal oxides, metal-organic frameworks, noble metal NMs, peptides, DNAs, and antibodies for several biomedical applications [108,167].

Various microfluidic technologies are used to synthesize QDs in different shapes, compositions, surface modification, photoluminescence properties, etc. Due to the technical advancement in the optical measurement system, most of the QDs synthesis process in microfluidics is automated by providing screening of the photoluminescence properties of QDs (this will be discussed in detail in the screening section). External energy is also used in controlled QDs synthesis. For example, an external magnetic field was used to synthesize single (4.35–6.14 nm) and hybrid (8.15 nm) QDs in microfluidic reactors; the device has an induction coil that continuously generates a magnetic field and heats the ferruginous pipeline, thereby controlling the reaction temperature (210–290 °C) [169]. QDs combined with DNA oligonucleotide are the right candidate for nucleic acid bioassays, drug delivery, and intracellular probes. Recently, a PDMS-based microfluidic chip (Fig. 4c) was fabricated to synthesize QDs-magnetic bead-oligonucleotide conjugate NMs [162]. The device consists of two flow-focusing droplet generators and one T-junction droplet mixing region. One droplet generator encapsulates QDs on the magnetic bead, while other forms droplets of DNA in oil. Finally, the droplet mixing region (serpentine channel) allows the single-step synthesis of DNA immobilization on magnetic bead-QDs. A tesla mixer was used to encapsulate QDs within the core of lipid-PEG hybrid NMs (lipid-QD: 60 nm) [84]. Tesla mixer provides a homogenous environment for nucleation and growth by reducing the mixing time, thereby controlling the QDs' nanoprecipitation. Further, mixing efficiency was improved due to the diffusion and convection at a high flow rate. By varying the flow rate ratio, the number of QDs encapsulated by lipid molecules was varied. The produced materials do not require further purification for *in vitro* or *in vivo* experiments.

Another category of QDs is carbon QDs, which have large surface area properties and can easily interact with molecules through stable bond formation, making them suitable for drug or gene loading vectors. They can also convert absorbed light energy at near-infrared to heat energy, offering the NMs for photothermal applications. Combined with PLGA NMs, formed nanohybrid features high antibiotic loading, chemo-photothermally synergistic anti-biofilm efficacy, and good biocompatibility. A microvortex microfluidic chip (Fig. 5a) was able to fabricate carbon QDs-PLGA NMs (100–150 nm) of varying surface charges (−20 to −50 mV) by controlling the flow rates of reagents alone [170]. The organic phase was injected through the outer two inlets, while the aqueous phase was supplied through the middle inlet. Formed

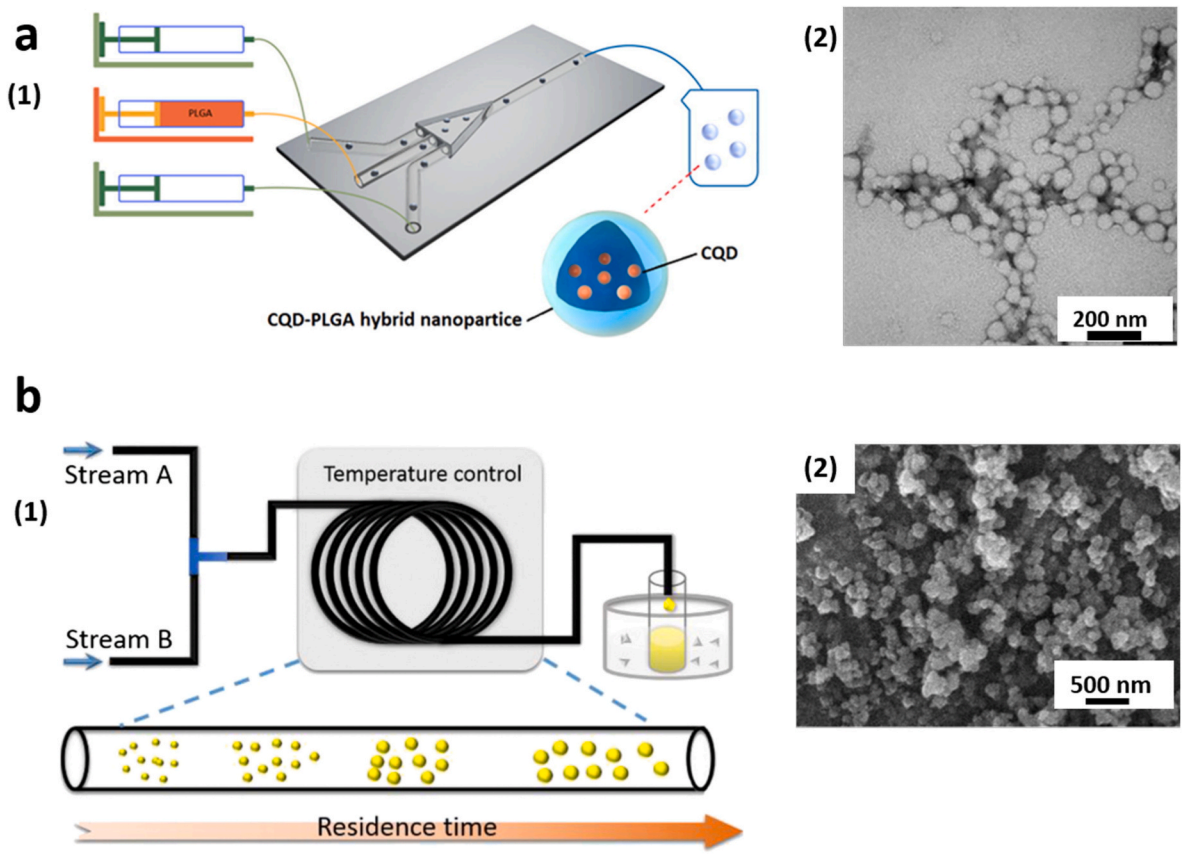

Fig. 5. Microfluidic platform for fabricating carbon-based and metal organic framework NMs. **a)** Synthesis of carbon QDs-PLGA nanohybrid using a microvortex chip. (1) Schematic diagram of synthesis. (2) TEM image of carbon QDs-PLGA NMs. Reproduced with permission [170]. Copyright 2020, Elsevier. **b)** Synthesis of metal organic framework using continuous flow microreactor; (1) Schematic illustration shows the size distribution of NMs with residence time. (2) SEM image of UiO-66 metal organic framework prepared at a flow rate of 0.2 mL/min. Reproduced with permission [171]. Copyright 2016, Elsevier. ODA-Octadecylamine; CQD-Carbon QD; SEM-Scanning electron microscope.

micro-vortices enable proper mixing, lead to superior reproducibility and high monodispersity.

The summary of the controlled synthesis of the QDs mentioned above is listed in Table 1. For clinical use, most of the QDs are used in conjunction with other NMs to enhance biocompatibility. Microfluidics serves as a good platform for synthesizing these NMs as it can easily tune the physicochemical properties of core-shell NMs through precursors' flow rate ratio. If we can adapt the fully automated synthesis into the QDs-based hybrid NMs, clinical translation of QDs will be much easier.

2.6. Carbon-based

Carbon NMs for biomedical applications include fullerene, carbon nanotubes (CNT), graphene, carbon dots (already described), nanodiamonds, nanohorns, and nano-onions. Carbon NMs have unique properties such as covalent and non-covalent conjugation, unique Raman signal, photoluminescence, and thermal and electrical conductivity [108]. CNT consists of sp^2 hybridized carbon atoms in nanometer-scaled tubules, and they possess unique thermal, electrical, optical, and mechanical properties. Recent progress in microfluidic-based CNT synthesis and facile functionalization expanded for the biomedical applications of CNT. The biocompatibility of CNT can be improved by substitutional doping with nitrogen atoms [23].

Vortex flow-based microfluidic devices were extensively used to fabricate various carbon-based NMs, manufacturing single-walled CNT toroid, lateral slicing of CNT, decorating CNT surface with noble metal NMs and synthesizing carbon dots (~6 nm) from multi-walled CNT. A standard vortex flow device accommodates an angled, rapidly rotating borosilicate glass tube inclined at 45^0 with the horizontal position. It has the advantages of easy installation, low cost, clogging-free synthesis, and easy scaling up [63]. A combination of microfluidic droplet generating techniques can fabricate 3D closed architectures by assembling 1D carbon NMs. Recently, Jun et al. synthesized a 3D CNT cellular network using a glass capillary microfluidic device combining flow focusing and co-flow techniques [172]. The device consists of two cylindrical glass capillary tubes with one end tapered, are coaxially arranged with a square capillary tube. The innermost gas phase was formed by inert nitrogen, the outer phase was polyvinyl alcohol aqueous solution, and the middle phase was oil (octadecylamine-CNT in toluene). This combination developed CNT-shelled microbubbles, which further generated gas-oil-water compound bubbles. By varying the flow rates, the size and shell thickness of microbubbles were controlled. To form a 2D hexagonal array, octadecylamine-CNT shells were assembled on silicon substrate by evaporation, and a stainless-steel mesh was used to form a 3D assembly.

The detailed information about the works mentioned above is summarized in Table 1. Compared to other categories of NMs, carbon-based NMs synthesis in microfluidics is not well explored. It further demands the study of the formation of carbon-based NMs, growth mechanism, and implementation in microfluidic platforms.

2.7. Rare-earth-based and others

Rare-earth metal NMs have diverse shapes with high paramagnetic properties, photoluminescence, and high catalytic activity [108]. Rare-earth-based NMs in biomedical applications include upconversion NMs, which are fluorescent materials that can convert lower energy photons to higher energy photons through an upconversion process [14]. Simple flow-focusing droplet devices are commonly employed to synthesize upconversion NMs [173].

Metal oxide NMs (commonly known as a metal-organic framework) other than iron oxides, such as titanium dioxide, cerium oxide, and zinc oxide, are also useful in biomedical applications due to their excellent biocompatible surface for cell attachment, cell proliferation, anti-oxidative properties, etc. Non-aqueous-based synthesis of the metal-organic framework was extensively studied. For example, flow focusing-based droplet generation followed by reaction channels of various geometries operating at different temperatures were employed to fabricate zinc oxide (100 °C), titanium oxide (200 °C), and cerium oxide NMs (170 °C) [174]. In another example, UiO-66 NMs (made up of $[Zr_6O_4(OH)_4]$) were synthesized using a simple continuous flow microreactor (Fig. 5b) with T-junction geometry to mix the reagents, followed by a reaction zone operated at 120 °C to promote NMs growth [171]. Nanomaterial size was controlled from hundreds of nanometers to dozens by tuning the flow rate (which can influence the residence time) alone. Increasing the residence time produced smaller particles, and beyond 3 min, microreactor was blocked due to particles' aggregation.

The description of the aforementioned NMs synthesis is summarized in Table 1. High temperature is often required for synthesizing metal-organic framework and upconverting NMs. Therefore, thermally conductive material that can withstand high temperature should be used as device material. Residence time plays a crucial role in synthesizing monodispersed NMs. By varying the flow rate, residence time can be tuned to achieve the desired NMs size.

*i.d.: internal diameter; o.d.: outer diameter; SiO_2: silica; EDC: 1-ethyl-3-(3- dimethylamino) propyl carbodiimide; $FeCl_2.4H_2O$: iron (II) chloride tetrahydrate); $FeCl_3.6H_2O$: iron (III) chloride hexahydrate; KH_2PO_4: Potassium dihydrogen phosphate; KCl: Potassium chloride; NaCl: Sodium chloride; $(NH_4)_2SO_4$: Ammonium sulfate; CdO: Cadmium oxide; OA: oleic acid; OLA: oleylamine; ODE; 1-octadecene; TOP: trioctylphosphine; TBP: tributylphosphine; Cs_2CO_3: cesium carbonate: lead bromide; $AgNO_3$: silver nitrate; $NaNO_3$: sodium nitrate; $NaBH_4$: sodium borohydride; NaOH: sodium hydroxide; CTAB: cityltrimethylammonium bromide; TMB: 1,3,5-trimethylbenzene; TEOS: tetraethyl orthosilicate; TSC: trisodium citrate; H_2O_2: hydrogen peroxide; NH_4OH: ammonium hydroxide; DMAP: 4-(dimethylamino)pyridine; $NaBH_4$: sodium borohydride; TOAB: tetraoctylammonium bromide; Na_2SO_4: sodium sulfate; $HAuCl_4$: chloroauric acid; PEG: Polyethylene glycol; PVP: polyvinylpyrrolidone; PPG: polypropylene glycol; DPPC: 1,2-dipalmitoyl-sn-glycero-3-phosphocholine; DSPE-PEG2000: 1,2-distearoyl-sn-glycero-3-phosphoethanolamine-N-[methoxy(PEG)-2000; NBD-DSPE: 1,2-distearoyl-sn-glycero-3-phosphoethanolamine-N-(7-nitro- 2–1,3-benzoxadiazol-4-yl); APTES: 3-Aminopropyl)- triethoxysilane; H2bdc: 1,4-benzenedicarboxylate acid; GMO: genetically modified organism; DOTAP: dioleoyl-3-trimethylammonium propane.

3. Microfluidic screening of nanomaterials

An ideal microfluidic platform to synthesize NMs for biomedical application demands synthesis of NMs with controlled physicochemical properties by tuning the operating parameters and adjusting the production rate for rapid screening (μg/min) and on-scale production (g/min). Over the years, several mechanisms and techniques have been developed for screening various reaction parameters. In earlier times, screening was performed after the synthesis (*ex situ*) and arrived at optimal conditions for the desired physicochemical properties of NMs. For this purpose, characterization techniques such as transmission electron microscopy (TEM), scanning electron microscopy (SEM), UV–Vis absorption spectrum, X-ray diffraction techniques, etc., were used. Nowadays, real-time parameters screening is possible by integrating the microfluidic platform with a camera, microscope, spectrometer, small-angle X-ray scattering (SAXS), etc., known as *in situ* or inline characterization [180]. Inline characterization or real-time screening helps to synthesize NMs rapidly through optimized reaction conditions and study the dynamics of material formation. Another screening method results in intelligent synthesis, where a control system uses real-time monitoring data to adjust the parameters and achieve the desired properties [181].

This section describes the wide range of available methods to screen the NMs' properties using microfluidics to speed up the process and critical examples of intelligent synthesis. We discuss how NMs with

specific features can be achieved by integrating the device with measurement sensors and developing an algorithm that suits a particular nanomaterial synthesis.

3.1. Real-time monitoring

Real-time monitoring of the NMs' synthesis process enables the visualization of the process and measures the parameters to control reaction kinetics, thereby obtaining NMs with desired physicochemical properties. Currently, available monitoring methods include spectroscopic measurements for measuring the optical properties, microscopic techniques to visualize the reaction process, and various sensors to measure flow rate, pressure, temperature, electrical resistance, etc. Optical characterization can be monitored through photoluminescence, absorbance, and X-ray spectroscopic measurements [180]. Photoluminescence and absorbance give quantitative information about NMs size, size distribution, shape, composition, and surface integrity. Both have advantages such as ease of use, low detection limits, high sensitivity, non-invasiveness, and fast response time. At the same time, X-ray spectroscopic measurements give information about the crystal and electronic structure of NMs. The complexity of the equipment makes its usage difficult in real-time monitoring. In general, absorbance and X-ray spectroscopic measurements are used for noble metal and metal hybrid NMs' screening, while photoluminescence helps to monitor QDs. As an example, particle cluster formation during the synthesis of polystyrene-coated Au NMs was studied using the screening parameters obtained from X-ray scattering and UV–Vis spectrometer in real-time [183]. These measurements were also used in investigating the effect of seed age in Au nanorod synthesis [184]. Controlling the shell thickness is essential in the case of core-shell NMs, specifically for drug delivery purposes. Knauer et al. showed a controlled deposition of shell metal using combinatorial synthesis by screening the flow rate variations in real-time [185]. As the plasmonic properties of metal core-shell depend on shell thickness, *in situ* screening of UV–Vis absorption spectrum synthesizes the desired shell thickness.

Microscopic measurements involve monitoring droplet size, slug size, reaction process, etc., through an optical or fluorescence microscope. As most of the device material is transparent including PDMS and glass, microscopic monitoring helps optimize the parameters. Since the reaction mixing happens within the droplets, controlling the droplet size can eventually control the NMs and PDI. For example, Bandulasena et al. investigated the droplet size variation in a three-phase glass capillary device with the help of a high-speed optical camera [79]. The device was mounted on the microscopic stage and, droplet generation was monitored with each parameter variation.

Real-time monitoring of direct measurement of size and shape of synthesized NMs is not explored yet. It requires the characterization techniques such as TEM, SEM, HR-TEM, etc., which are very sophisticated equipment, and the NMs sample has to be prepared in advance for their usage. Further, NMs have to be purified through filtration or multiple centrifuging before characterizing them. If we can perform particle purification within microfluidics, it will be a drastic change, and screening followed by clinical translation will be easy.

3.2. Intelligent synthesis

In an intelligent system, thousands of synthesis reactions can be carried out within a fraction of time. The bottleneck of such a system is a sophisticated and specialized 'intelligent' algorithm. Developing such an algorithm is challenging as the process handles toxic and explosive chemicals with minimal reagent consumption [181]. Despite these difficulties, the intelligent synthesis of QDs and their hybrids are well established. Very few examples addressed the intelligent synthesis of other NMs. The concept of intelligent synthesis was introduced by Krishnadasan et al. to synthesize QDs by monitoring the emission spectra [186]. Monitored emission spectra were fed into the algorithm, and based on that information, it generated a reduced scalar dissatisfaction coefficient. According to the coefficient value, the reaction condition was optimized to reach the desired value. The successful adaptation of this approach requires clogging-free and non-degradable stable reagents as the search for an optimized algorithm takes long time. Bovone et al. showed a method for rapid formulation screening and production of polymeric NMs after being synthesized in a coaxial jet micromixer [89]. This was achieved by controlling the output via pump software and monitored the process through a bright field inverted microscope. Using rhodamine-containing central organic stream, flow behavior was observed for various Reynolds numbers. The effect of mixing speed (slow mixing and rapid mixing) and polymer concentration on production rate were screened and formulated for optimal polymer NMs with minimum size and low PDI. The same device was used to scale-up the synthesis due to its rapid screening at low production rates. One of the recent examples monitored NMs formation by conjugating microfluidics with electrical resistance measurement in studying the corona formation around the carbon NMs. By coupling with machine learning and wavelet transform algorithm, it could discriminate corona types, which further enhanced targeted drug delivery [187]. In the future, the same approach can be used to discriminate the corona types associated with other NMs categories and correlate with their inherent characteristics. This can compare among other NMs in their bio-nano interactions, which could be potentially helpful in *in vivo* applications. The factorial design of the experimental approach was used in rapid size optimization of liposomes synthesized in a staggered herringbone micromixer [188]. In this approach, tuning parameters like flow rate ratio and total flow rate were screened to optimize the synthesis parameters by analyzing several experiments. Statistical tools, including multiple linear regression and partial least squares, were used to fit the optimal model. This model could help to optimize other nanocarrier screening and could be favorable for conventional drug delivery systems.

The feedback process controlling mechanism is an advanced method to tune the synthesis parameters to achieve automation. In this approach, a set of process parameters are continuously monitored and compared with the set value. Several algorithms were developed in this regard; the famous Kriging algorithm was developed by Bezinge et al. to predict future reaction conditions based on the photoluminescence measurements of QDs [189]. The algorithm computes or refines the reaction parameters by mapping photoluminescence with the target wavelength of each iteration. The screening method is fast, accurate, and reliable for QDs production. Combining with a scaled-out reactor will make the commercial production of QDs easier with predefined emission spectra. In terms of the information obtained from microfluidics, in conjunction with the Kriging algorithm, microfluidics can maximize the output information without escalating the number of experiments.

Similar to the Kriging algorithm, artificial neural networks are also helpful in reaction optimization and optimizing NMs synthesis [181]. In 2017, Kim and co-workers integrated parallel swirling microvortex reactors with intelligent feedback control to screen lipid-polymer NMs' physicochemical properties in a highly reliable and robust manner, which allowed the easy clinical translation of NMs for imaging and drug delivery (Fig. 6a) [182]. A simple swirling microreactor with varying diameters increased the mixing efficiency (90% or higher), and produced NMs with desired properties. It can model into an analog fluidic circuit with an impedance and pressure at the inlets and outlets. Microreactor inlet pressure was evaluated using these impedance values for various flow conditions (or Reynolds number); hence controlling the pressure variation can eventually control the impedance, thereby improve mixing efficiency. In order to obtain high throughput and reproducibility, a feedback pressure control loop was used. Large scale optimized synthesis was achieved by connecting 25 swirling microvortex reactors in parallel with a feedback pressure control loop to measure the inlet pressure variations of parallel reactor networks, then

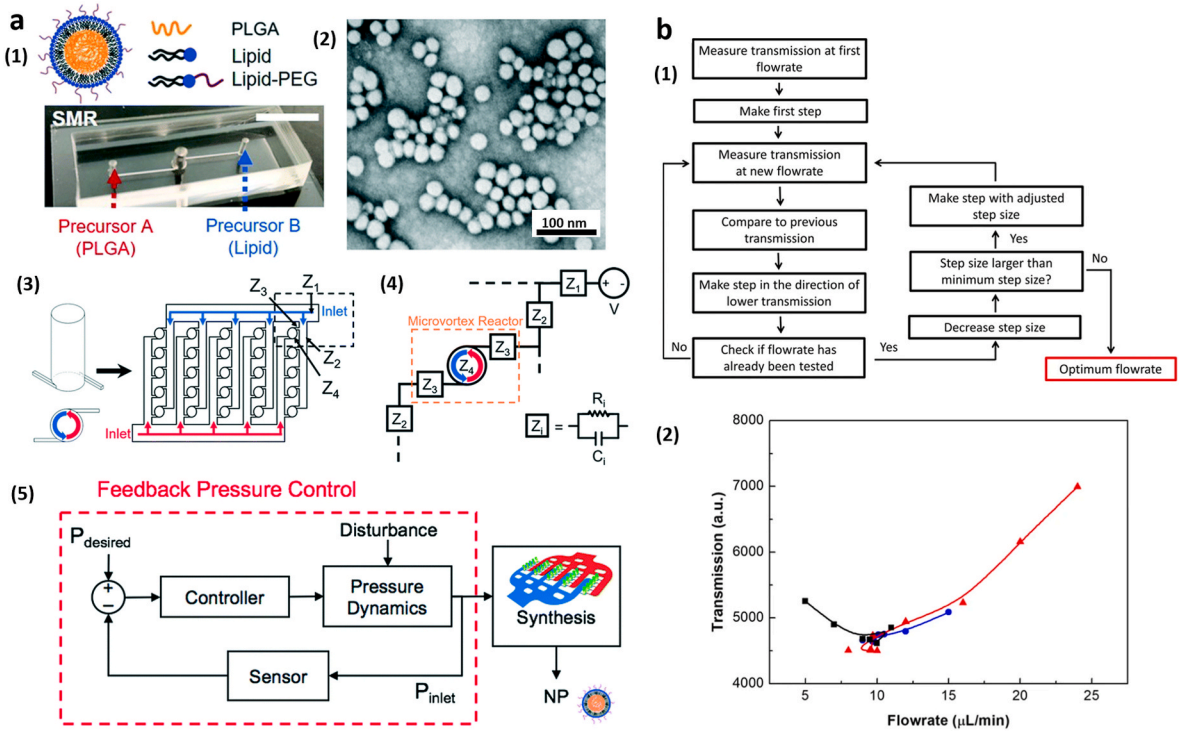

Fig. 6. Screening of NMs using microfluidics. **a)** Robust and reliable fabrication of lipid-PLGA NMs using parallel networks of swirling microvortex reactors and feedback pressure control loop. (1) Photograph of the device (scale bar is 5 mm) and schematic drawing of the NMs. (2) TEM image of synthesized NMs. (3) Parallelized microvortex array with 25 microreactors with a microfluidic network. (4) Fluidic circuit analogue decomposition of the parallel device, where Z_i is the impedance of ith inlet, R_i and C_i are resistance and capacitance respectively. (5) Schematic of feedback pressure control loop to synthesize lipid-polymer NMs. Reproduced with permission [182]. Copyright 2017, Royal Society of Chemistry. **b)** Screening of transmission measurement to control the size by optimizing the flow rate. (1) The algorithm used to optimize the flow rate. (2) The plot of flow rate dependent transmission measurement of three experiments with an initial guess of 5, 15 and 24 μL/min and step size of 2, 3 and 4 μL/min represented by black, blue and red lines respectively. Reproduced with permission [161]. Copyright 2020, Nature. SMR-Swirling microvortex reactor; Z-impedance; R-Resistance; C-Capacitance; V-voltage; NP-Nanoparticles. (For interpretation of the references to color in this figure legend, the reader is referred to the Web version of this article.)

amplified and compared with the desired set value. The method enabled robust manufacturing of lipid-polymer NMs (1.8 kg/day), and extension into an array could result in a greater production rate. In addition, this method could help to produce a wide range of hybrid NMs for therapeutics and diagnostics efficiently.

In another example, real-time evaluation of transmission measurement and a self-optimizing algorithm were used to automate the synthesis process [161]. Automation was performed by equipping the Tygon glass capillary tubing droplet microreactor (Fig. 4b (1)) with an optical transmission measurement device in conjunction with a

Table 2
Review of recent works in the screening of NMs' parameters during microfluidic synthesis and automated approach.

Composition of NMs	Shape	Size (nm)	Screening Parameters	Details of Real-time Monitoring	Intelligent Synthesis Details	Ref.
Carbon	Sphere	10, 50 & 90	Electrical resistance	Biomolecular corona formation of NMs	Machine learning & wavelet transform	[187]
Iron oxide-Au	Core-shell	13.1 ± 2.5	Droplet transmission	Transmission w.r.t flow rate	Simplex optimization algorithm	[66]
Ag	Sphere	5–80	Absorbance	UV–Vis absorbance	Mie-theory based calibration algorithm	[67]
Au	Rod	–	SAXS diameter & absorbance	SAXS & UV–Vis spectrum	–	[119]
Perovskite crystals	–	–	Phase velocity & length	Phase velocity, length sensors & camera validation	Custom user interface & slug tracking algorithm	[190]
Au-polystyrene	Core-shell	46.9 ± 2.0	Scattering intensity & absorbance	SAXS & UV–Vis Absorption	–	[183]
Carbon dot	Sphere	2.2–4.3	Photoluminescence	Temperature & fluorescence imaging	–	[191]
Lipid-polymer	Core-shell	<200	Inlet pressure	Inlet pressure & absolute error	Pressure feedback control	[182]
Au–Ag	Core-shell	11.5	Absorbance	Microphotometers at different wavelengths	Combinatorial synthesis	[185]
CdSe	–	–	Absorbance & fluorescence	Spectrometer	LabVIEW algorithm	[192]
$CsPbX_3$ (X = Br, I, Cl & Br/Cl and Br/I)	–	8–12.5	Molar ratio of reagents, reaction temperature and reaction times	Photoluminescence & absorbance	–	[193]
Lead halide perovskite	–	–	Photoluminescence	Spectroscopic measurements	Kriging based adaptive sampling algorithm	[189]
$CsPbX_3$ (X = Br, I, Cl)	Cube	–	Fluorescence lifetime	Photoluminescence	LabVIEW algorithm	[194]
Lead halide perovskite	Cube	~40	Photoluminescence/absorbance	Photoluminescence & absorbance	Combinatorial approach	[195]

computer algorithm (Fig. 6b). The algorithm automatically finds the optimum synthesis conditions for the iron oxide-Au core-shell NMs formation; it starts from two initial guesses of flow rate and changes Au precursor's flow rate until it reaches the minimum optical transmission of the droplet. Once it arrives at the value, the flow rate increases by the step size of 0.1 μL/min. As the flow rate of Au precursor changes, Au shell thickness varies due to droplet size changes. This method can be adapted for any segmented flow-based devices that can measure the transmission of slug or droplets through a capillary which eventually corresponds to the size of single-component NMs or shell thickness of core-shell NMs.

Table 2 summarizes the recent works on inline screening of NMs' parameters using microfluidics. It is observed that the majority of the synthesis process uses real-time monitoring of spectroscopic measurements due to its various advantages. Also, inline screening is developed mainly on QDs, followed by noble metal and their hybrid combinations. Feedback control allows robust biopolymer-based nanocarrier manufacturing that helps to scale-up the NMs for drug delivery. As the integrating unit increases, complexity arises with multiple parameter screening and allows reasonable control over-optimized NMs synthesis. At the same time, a fully automated microfluidic platform need not involve complex algorithms. It should merely screen the parameters and set the reaction conditions using simple algorithms [180].

4. Clinical evaluation of Microfluidic nanomaterials

Even though tremendous efforts observed over the past few years in translating NMs for clinical use, the noted growth is relatively slow. Only a few NMs got approval from the US Food and Drug Administration (FDA) and the European Medicines Agency. It includes polymer NMs for drug delivery and diagnostic imaging, iron oxide NMs for MRI, and liposomes carrying the anticancer drug for chemotherapy [196]. Conventional clinical evaluation of NMs uses 2D cell culture, which is very easy to implement, but difficulties in reconstructing the exact physiological behavior result in an inaccurate outcome. Compared to 2D, the 3D cell culture model mimics the tissue structure greatly but fails to maintain flow conditions and chemical gradients. The animal model can provide more accurate results, but it is complicated, expensive, and time-consuming [197]. On the other hand, microfluidics evolved as a cost-effective platform, allowing easy cell culturing with specific cell numbers, extracellular matrix, the interaction between cell-cell and cell-extracellular membrane with precise control over mechanical cues and shear stress. Microfluidics can also mimic the *in vivo* flow environment for NMs evaluation. The shear stress-induced due to flow behavior reduces the NMs sedimentation and aggregation, thereby improves cellular uptake. Transparent devices based on PDMS (majority) or glass allowed the real-time monitoring of physiological behavior of NMs and corresponding biological response. High-throughput evaluation can be carried out by making parallelization and integration [196]. Like fluid flow, microfluidics can also stimulate chemical gradients, easy to partition multi-organs on-chip, and easily control the local environment [197].

A successful NMs delivery into the human body involves the following sequence; intravenous infusion, penetration through blood vessel endothelium, penetration through the target tissue, finally uptake and detainment by the target tissue. Before achieving the final stage, NMs may face several issues; poor penetration, rapid plasma clearance, poor uptake or unexpected organ uptake and accumulation, etc. The reasons behind plasma clearance are due to easy renal filtration (<5.5 nm size) or macrophage internalization (20 nm- 2 μm). NMs transport may hinder due to barriers such as the blood-brain barrier, blood-vessel endothelium, and interstitial fluid pressure. Unexpected organ uptake leads to toxicity or lesions. In addition, at the molecular level, flow behavior has a significant impact [197]. For example, shear stress can influence NMs binding and detachment, and can identify specific and non-specific adhesion. Also, it regulates nanomedicine uptake and triggers the release of drugs. There are few NMs sensitive to shear stress, including lenticular liposomes and microscale aggregates of NMs. Hence, these NMs can target obstructed blood vessels, as it induces shear stress due to thrombosis (blood clot) or embolism (blocked by a blood clot). NMs properties like shape, size, surface charge, and functionalization have to be optimized to achieve successful delivery. With the help of specific microfluidic models, NMs interaction for specific biomedical applications can be quantitatively studied before the administration. Clinical evaluation of NMs can be quantitatively measured using parameters such as hemocompatibility, toxicity, NMs transport, uptake by cells, target NMs accumulation, and NMs efficacy. The currently available microfluidics models for this evaluation are blood vessel-on-a-chip, blood-brain barrier model, single-cell microfluidics, tumor-on-a-chip, lung-on-a-chip, body-on-a-chip, and animal-on-a-chip [197]. This section discusses the essential examples in each category of the microfluidics model for clinical evaluation, its features, advantages, and disadvantages. It explains how a particular model suits evaluating a specific parameter.

4.1. Blood vessel-on-a-chip

The blood vessel-on-a-chip model mimics the blood vessel's microenvironment and helps to study the interaction among blood cells and NMs, NMs margination, the impact of shear stress and vessel geometry on NMs accumulation, and vessel permeability on NMs translocation. Since most NMs for biomedical applications introduce intravenously into the blood, they should not cause any significant changes to blood cells or blood plasma. The Hemocompatibility of NMs can be evaluated using a blood vessel-on-a-chip model, and it possesses higher sensitivity than conventional hemolysis analysis [197]. For example, a PDMS-based microfluidic device (20x400x26,389 μm) with a hyperbolic-shaped central channel was used for NMs' hemocompatibility evaluation (Fig. 7a) [198]. This geometry allowed RBCs to detect small rigidity changes (deformation index) when they pass through the central channel. Even with considerable shear stress, the strain rate was maintained at the center. Iron oxide NMs' effect on RBC stretching has been evaluated by performing the experiments in the presence or absence of NMs. With the help of an inverted microscope, morphological changes were observed [198]. The study also proposed that the size, shape, and composition of iron oxide NMs may influence RBC membrane interaction. Further, this study can be extended to investigate other hemorheological and biological interactions between iron oxide NMs and RBC. These interactions have to be explored together in the future, thereby opening the door to nanomedicine evaluation by understanding RBC-NMs interaction in depth. Compared to the traditional hemocompatibility test, microfluidic model has shown very high sensitivity. Hemocompatibility can also be analyzed using platelet activation, plasmatic coagulation test, and leukocyte phagocytosis inflammation. Besides hemocompatibility, NMs transport and its efficacy were also evaluated with blood vessel-on-a-chip model [197].

An ideal blood vessel on-a-chip model for clinical evaluation of NMs should incorporate geometries of vasculature such as bifurcations, straight channels, and tortuosities. It should study the impact of NMs with various sizes, shapes, and surface charges. One of the studies on hemocompatibility of mesoporous silica NMs observed that it significantly increased platelet aggregation and adhesion to the endothelium. Also, rod-shaped NMs showed higher specific targeting and lower non-specific accumulation than spherical NMs in endothelialized channels [203].

As most NMs for clinical application involve intravenous injection, its interaction with blood has to be investigated in detail. A blood vessel-on-a-chip model can evaluate NMs' hemocompatibility and their transport through blood. It could help to develop various nanocarriers for therapeutic purposes.

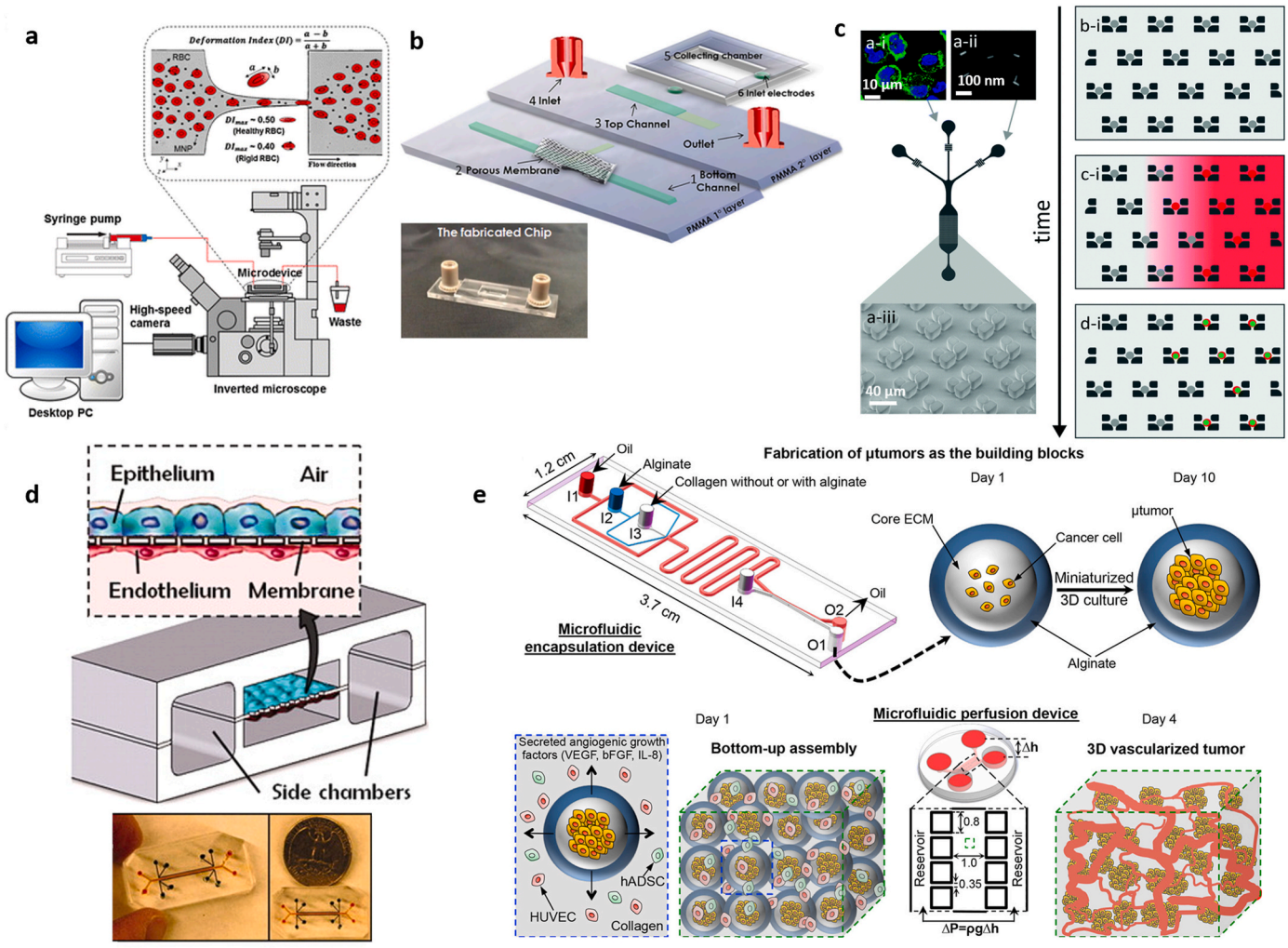

Fig. 7. Clinical evaluation of NMs using various microfluidic platforms. **a)** Schematic diagram of the experimental setup of a blood vessel-on-a-chip model for hemocompatibility evaluation. Reproduced with permission [198]. Copyright 2016, Springer. **b)** Schematic representation and photograph of blood brain barrier model chip to study NMs transport across barrier. Reproduced with permission [199]. Copyright 2016, Wiley Periodicals, Inc. **c)** Schematic representation of single-cell microfluidic chip based on microtraps to investigate the cellular uptake and toxicity of NMs; (a–i) confocal fluorescence microscopic image of dendritic cells, (a-ii) SEM image of Au nanorod, (a-iii) SEM image of microtrap array and schematic representation of temporal analysis of microfluidic device; (b–i) cell trapping, (c–i) nanorod delivery and (d–i) antigen processing. Reproduced with permission [200]. Copyright 2016, Royal Society of Chemistry. **d)** Dynamic lung-on-a-chip model to study the effect of NMs on the pulmonary system. Reproduced with permission [201]. Copyright 2010, The American Association for the Advancement of Science. **e)** Tumor on-a-chip model formed by culturing 3D vascularized tumor in a microfluidic device to study NMs cytotoxicity and efficacy. Reproduced with permission [202]. Copyright 2017, American Chemical Society.

4.2. Blood-brain barrier model

The blood-brain barrier is the vascular border of the central nervous system (CNS) through which substances are transported between blood and the brain. It consists of complex cellular networks of astrocytes and pericytes endothelial cells. Hence, the CNS drugs find difficulty in penetrating this barrier and reduce the success rate in developing the medicine for the CNS [204]. The blood-brain barrier model helps to evaluate the NMs (or nanomedicine) transport into the CNS. It predicts the NMs performance in brain endothelium and opens the platform for efficient drug discovery into the brain.

There are only a few works observed on the microfluidics blood-brain barrier model to study NMs transport. Falanga et al. evaluated the transport of NMs by gH625 peptide across the barrier with this model (Fig. 7b) [199]. It mimics the *in vivo* flow pattern and allows brain endothelial cells to grow on a porous membrane, sandwiched between two channels representing the blood and brain side. They found that gH625 peptide conjugated NMs (fluorescent amine capped polystyrene) can easily cross the barrier under flow conditions. Without the peptide functionalization, NMs were unable to reach the CNS due to the barrier. Hence, this study revealed a higher affinity of gH625 peptide conjugated NMs on cells than blank NMs under a flow rate of 5 µL/min (fall under blood vessel flow rate). The reason might be the tropism shown by the peptide for cell membrane cholesterol, which promoted the adhesion of peptide-functionalized NMs on cells. The same model without cells can also evaluate the NMs for clinical applications [197]. Recently, Kim and co-workers developed another blood-brain barrier model chip that mimics the contact among brain vascular endothelium and human brain perivascular pericytes with the 3D networks of astrocytes [204]. The chip consists of 4 layers; a bottom glass slide, a lower layer, a porous membrane, and an upper layer. The Upper and lower layers are made up of PDMS and correspond to the 2D vascular endothelial region and 3D brain microenvironment. These layers are separated by a porous membrane of 7 µm thickness and 8 µm diameter pores. The lower layer consists of three parallel channels separated by a series of micropillars and cultures pericytes and astrocytes in a 3D Matrigel that flows through the center channel and two side channels. The height of all the channels is 100 µm, and the width varies from 200 to 400 µm. Compared to the

previous chip model, this chip was able to quantify the distribution of NMs in vascular and perivascular space and on each cell along with the NMs transport. To assess the NMs' transport, bio-conjugated high--density lipoprotein NMs were intravenously injected with a fluorescent dye and observed easy administration and an accumulation of ~3% in the brain. The mentioned compartmentalized chip model allowed to track the NMs' penetration across the barrier. For this purpose, they used a precise time-lapse sampling and fluorescence-activated cell sorting analysis, which helped to quantify the 3D distribution of NMs across the blood-brain barrier. Further, this quantitative analysis provides information on the cellular uptake of NMs, thereby enabling to calculate the targeting efficacy at the cellular level. The device's high throughput can be achieved by performing NMs' evaluation using a multiple parallel blood-brain barrier model.

In the future, it is expected the development of a sophisticated blood-brain barrier model that could mimic the complex interaction associated with the blood-brain barrier and could be used in translational medicine research specifically for neurological disorders.

4.3. Single-cell microfluidics

At the single-cell level, clinical evaluation of NMs can be performed by creating many small structures comparable with the cell's size, termed single-cell arrays. It can be an array of microwells or microtraps to trap the single-cell, incubate NMs on cells, and analyze NMs' uptake and toxicity [196]. In general, metal and metal NMs can generate reactive oxygen species, induce reactive stress, and lead to DNA lesions or genotoxicity. Hence, the effect of cellular uptake has to be evaluated at the DNA level. A PDMS-based comet chip was used to investigate the genotoxicity of silica, zinc oxide, iron oxide, Ag, and cerium oxide NMs, and observed that the device could provide both DNA damage and gene mutation induced by NMs [205]. The chip consists of size-tunable microwells arranged in ordered microarray, and cells were seeded in the microwells and exposed to NMs of various compositions. A comet assay was performed *in situ* to investigate the DNA damage in each cell; the genotoxicity in human lymphoblastoid cells varied from high to low for zinc oxide, Ag, iron oxide, cerium oxide, and silica NMs, respectively. In the case of adherent Chinese hamster ovary cells, the trend in genotoxicity is Ag, iron oxide, zinc oxide, cerium oxide, and silica. From both genotoxicity profiles, it has been observed that silica NMs possess the lowest genotoxicity. The same platform could help to compare other NMs dosimetry analyses to prepare NMs hazard ranking. This model has advantages such as lowered noise, bias, labor, and high throughput (~more than 2 orders of magnitude) compared to traditional assay. By combining with fluorescent *in situ* hybridization, DNA damage due to NMs can be located and used for gene repair. The comet chip model can be expanded further to investigate specific DNA lesions and double-stranded DNA breakage due to NMs exposure.

The effect of NMs on protein expression at a single-cell level was well studied by single-cell immunoassay and single-cell western blotting platforms [196]. Wu et al. analyzed the cytotoxicity of QDs in a microwell array-based single-cell chip and found that cytotoxicity depends on cell cycle phases [206]. The chip consists of a microwell array for trapping single cells and fluidic channels that helps to keep the QDs concentration to a stable value. The variation in cytotoxicity of different cell cycle phases is due to the difference in cellular uptake of NMs at each phase. The device could be used for single-cell research in detail by combining it with high throughput analysis. Similar to the cell cycle phase, heterogeneity in cellular uptake of NMs were also studied using single-cell microfluidics. For example, a chip based on precisely ordered microtraps was used to study cellular uptake and toxicity of Au nanorod mediated vaccine (Fig. 7c) [200]. It consists of an array of microtraps to isolate single primary dendritic cells. A concentration gradient ovalbumin-loaded Au nanorod was supplied across the width of the array and successfully tested the impact of NMs on dendritic cells. This device can estimate the NMs properties, effect of cell heterogeneity, and NMs uptake in a high throughput manner. Real-time images were captured using time-lapse spectroscopy to study the dynamics of cell-NMs interactions, and the platform applies to any NMs formulations and cell types. This study used biologically relevant human cells compared to cell lines which are advantageous in investigating actual NMs-cell interaction. Further, this device can provide quantitative information about the dynamics of intracellular activity of NMs, which helps to discover drugs and vaccines. Among all the microfluidic technology, droplet-based devices have shown great promise in single-cell drug screening. Cellular uptake of Au NMs-citric acid and Au-DNA NMs on HeLa cells were analyzed using an on-line droplet chip inductively coupled with plasma mass spectrometry hyphenated technique [207]. The results revealed that NMs with high concentration and short incubation time is beneficial for NMs based biomarker analysis and intracellular delivery. As a result of difference in adhesion and internalization mechanism, Au-DNA NMs uptake is more on cells than Au-citric acid NMs.

In general, single-cell microfluidics is an adequate platform to investigate the intracellular activity of NMs, which helps in designing NMs based drugs and vaccines for therapy and developing dosimetry analysis of NMs. Dosimetry analysis of noble metal NMs is of significant concern as they induce genotoxicity. For industrial adoption, the device could be attached with a high throughput analysis system.

4.4. Lung-on-a-chip

Sometimes, through inhalation, NMs may enter the respiratory tract and easily interact with alveolar cells. Hence it should be evaluated before clinical use with a proper Lung-on-a-chip microfluidic model. This model provides quantitative information about NMs transport into the pulmonary vascular endothelial and alveolar epithelial cells. Ingber and co-workers in 2010 fabricated a famous lung-on-a-chip model (Fig. 7d) [201]. The device has three PDMS layers to mimic lung alveolar epithelial cells, extracellular membrane, and vascular endothelium, with the middle porous layer as an extracellular membrane. Breathing was achieved by providing pressure on the layers driven by the computer-assisted vacuum and release from the two side chambers. Overall, this device implemented the microarchitectures of the alveolar-capillary unit, kept the alveolar epithelial cells at air-liquid interface, allowed them to exert relevant physiological forces on the entire structure, and investigated the effect of forces on lung functions. For clinical evaluation, NMs were introduced into the alveolar epithelial channel and studied the impact during breathing. Without any mechanical stretching, NMs translocation is the same as normal static cell culture conditions, but during mechanical stretching (mimic breathing conditions), translocation of NMs increased four-fold. This model mimics complex physiological phenomena associated with the lung in a single device. Another lung-on-a-chip model developed by Zhang et al. considered more dynamic and studied the nanotoxicity induced by metal-organic framework on epithelial and endothelial cells [208]. The chip represents the 3D model of the human lung by co-culturing human vascular endothelial cells and alveolar epithelial cells on a 3D Matrigel membrane with flow cues that mimic the structural and functional alveoli. Results were quantified by performing assays for dose-dependent cytotoxicity, reactive oxygen species production, apoptosis, junction protein expression, and increased permeability to macromolecules.

Recently, Feng and co-workers simulated a lung-on-a-chip model to study the NMs' interaction with alveolar cells by modeling NMs using Lagrangian and Euler models [209]. They studied the adsorption and deposition of various size NMs under different exercise and breath-holding patterns. It has been found that during exercise, the NMs deposition increases, and deposition rate varies non-monotonically with particle size. Even though the lung-on-a-chip model successfully studied the nanotoxicity introduced by NMs into the alveolar tissues by simultaneously introducing shear stress and during alveolar gas exchange,

they did not include immune cells [210].

In the future, it is expected to develop a more realistic complex human lung model consisting of other organs, which could study NMs' interaction with lung alveolar epithelial cells and NMs' transport, and toxicity due to organ-organ interactions.

4.5. Tumor-on-a-chip

The Tumor-on-a-chip model is used to study the NMs accumulation on the target tissue and its efficacy [197]. Penetration of NMs onto the tumor target tissue depends on the size and surface features of NMs and the tumor environment. High tumor cell density and interstitial fluid pressure act as a barrier for proper penetration, and the result is it cannot cross more than one or two cell layers. *In vitro* 3D tumor cellular models combined with a microfluidic chip is termed as tumor-on-a-chip model. Cytotoxicity and efficacy of NMs-drug conjugate on tumor target can be analyzed using this model. Tokarska et al. developed such a model to study the cytotoxicity of nanocarrier loaded with verteporfin (medication to eliminate abnormal blood vessels) photosensitizer (size <120 nm) [213]. The chip has four V-shaped microstructures. It enables testing various cell culturing platforms (monoculture, coculture, and mixed culture) simultaneously and a concentration gradient generator to test the four concentration states concurrently. Monoculture was performed using three pairs of not connected microchambers, while coculture was performed in five pairs of connected channels (1000, 800, 600, 400, and 200 μm). Finally, a single microchamber followed by coculture allowed mixed culture. The results revealed that nanocarrier loaded with verteporfin has long-term colloidal stability, and after intravenous injection, it showed more extended circulation in the bloodstream. The *in vitro* study also evaluated the undesirable effects of nanocarriers on non-targeted sites with the information about target delivery and cytotoxicity profile of photosensitizers. In the future, this device could be used to study the target delivery and cytotoxicity of any photosensitizers for photodynamic therapy.

Vascularization has to be implemented in the tumor-on-a-chip model to evaluate the efficacy of NMs-drug conjugate on the tumor target. As an example, a 3D vascularized human tumor (Fig. 7e) was developed using (1) a nonplanar microfluidic encapsulation device (PDMS-based)

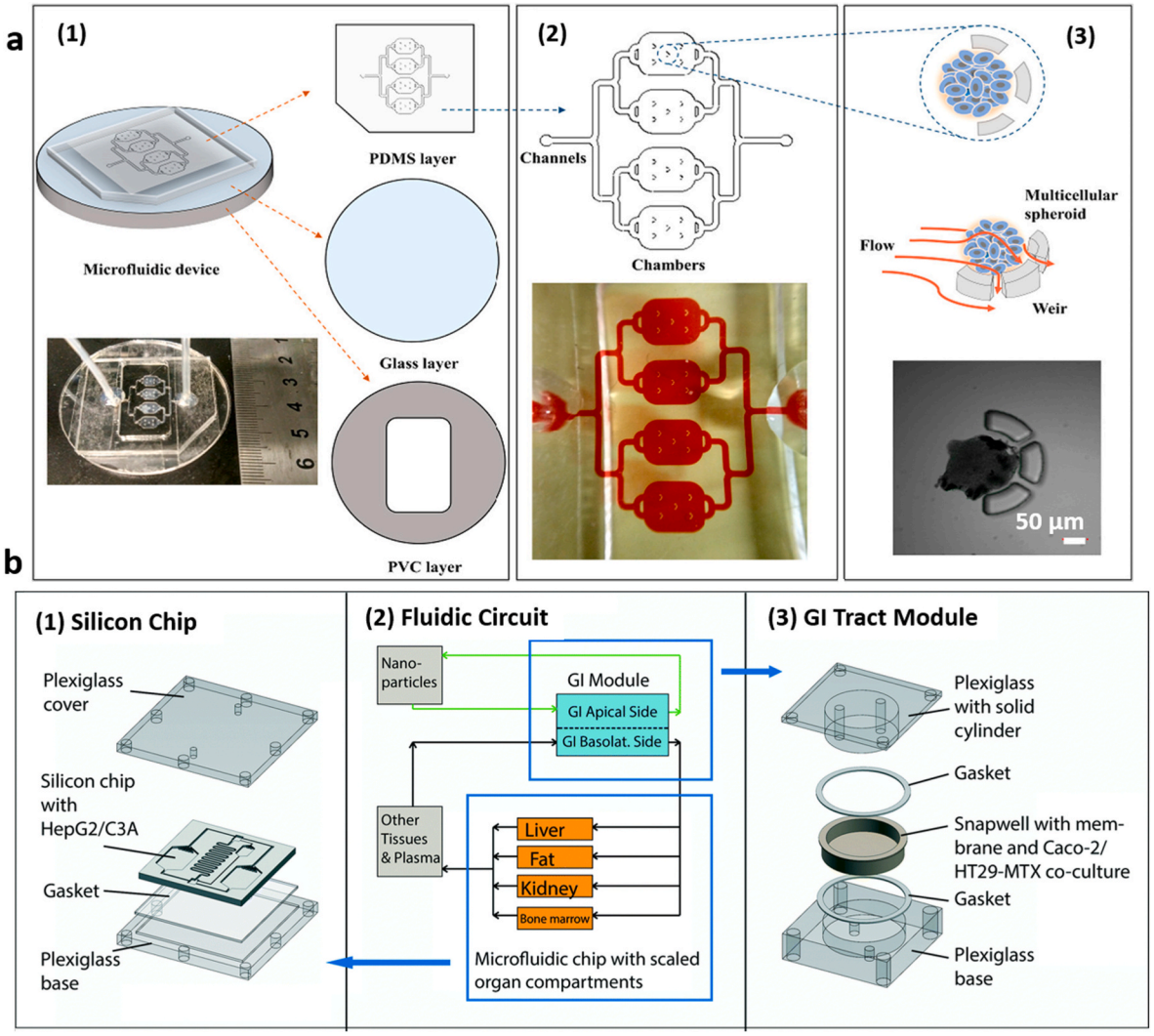

Fig. 8. Clinical evaluation of NMs using tumor on-a-chip and body on-a-chip models. **a)** Tumor-on-a-chip to evaluate the effect of NMs' surface charge, protein corona, exterior flow, and NMs accumulation on tumor target. (1) schematic drawing of the three (PVC bottom layer with square window in the middle, glass layer with thickness of 0.17 mm & PDMS upper layer) layered chip and photographic image, (2) schematic image of the top layer with 4 chambers. Each chamber has 5 semicircular weirs of two apertures, and (3) schematic and microscopic image of the weir trapping the spheroid. Reprinted with permission [211]. Copyright 2017, American Chemical Society. **b)** Schematic of the body on-a-chip model to investigate the hepatotoxicity of NMs. (1) silicon chip, (2) fluidic circuit, and (3) GI tract module. Reprinted with permission [212]. Copyright 2014, Royal Society of Chemistry. (For interpretation of the references to color in this figure legend, the reader is referred to the Web version of this article.)

to encapsulate tumor cells in core-shell microcapsules and (2) a microfluidic perfusion device (PDMS-glass) to assemble microtumors and stromal cells (including endothelial cells), enables the formation of millimeter-sized complex 3D vascularization surrounding the tumor cells [202]. FDA-approved doxorubicin (DOX) and NMs-DOX efficacy was evaluated using this model and observed that DOX alone suffers from drug resistance in the 3D model. By encapsulating with NMs (~60 nm with the spherical shape), it overcame the high drug resistance. Apart from drug response analysis, this model enabled to study the tumor progression under microenvironment, invasion, and metastasis. Overall, the results showed that this model allowed to understand the tumor progression and observed that interactions among cell-cell and cell-extracellular membrane play an important role in tumor progression stages. This information could help to discover the NMs-based drug formulation.

The tumor-on-a-chip model can also study the NMs accumulation on target tissue under various physiological flow conditions. For example, A spheroid (3D aggregates of tumor cells) on-a-chip model consists of four chambers to accommodate multicellular spheroids (~200 μm) in a three-layered (PDMS, glass, and polyvinyl chloride) microfluidic chip (Fig. 8a) was used to study the NMs penetration mechanism into the spheroids as well as the effect of surface charges of NMs onto the penetration [211]. Before penetration, polystyrene NMs (100 nm) surface was modified (in the presence of serum protein) by forming protein corona by adsorbing serum protein onto its surface. It results in lowering the NMs concentration on the spheroid surface with deeper penetration. Interstitial fluid flow was improved with exterior fluid flow conditions but strips the NMs (especially with NMs and protein corona) from spheroids' surface. In effect, penetration flux reduces significantly. Also, negatively charged NMs could easily attach and penetrate deeply inside the spheroids due to protein inhibition [211]. To better understand the spatiotemporal distribution of NMs on tumor targets and to strengthen the knowledge about mass transfer characteristics, this *in vitro* study has to be explored in detail in terms of its mechanism.

In another work, *in vivo* like interstitial flow was reproduced using tumor spheroids, and laminin surrounding the spheroids represented the physical barrier between medium and cells [214]. The chip was used to study the effect of NMs' size, receptor targeting, and flow rate effect on NMs accumulation on tumor target. The result showed that PEG conjugated NMs and iron transporting transferrin conjugated NMs of 40 nm could easily penetrate the spheroids and accumulate mainly in the interstitial spaces. The study found that NMs of size <110 nm at the tissue-media interface could quickly diffuse through the extracellular matrix and interact with the tumor cells. In addition, the delivery efficiency was higher (15-fold) with transferrin conjugated NMs than PEG conjugated NMs. Moreover, when the flow rate increased from 15 to 45 μL/min to create interstitial flow conditions, the accumulation of both NMs increased by two-fold, but the penetration was not so profound.

In summary, the tumor-on-a-chip model evaluates NMs' accumulation on the target tissue and its efficacy. It further enables nanomedicine development by evaluating *in vivo* outcomes and optimizing the dosage and treatment strategies. With the help of highly sensitive detection methodologies like the confocal microscopy technique, the tumor-on-a-chip model provides long-term tissue transport of NMs. To improve the analysis of systemic behavior of NMs, tumor-on-a-chip can be included with compartments to mimic blood filtration by the liver and kidneys. In the future, high throughput screening for optimal nanomedicine delivery can be achieved by executing parallel device models to screen large libraries of NMs.

4.6. Body-on-a-chip and animals-on-a-chip

Most clinical evaluation was carried out using single cell or organ-on-a-chip model, limiting the ability to test NMs accumulation and toxicity on undesired target body organs or cells. Compared to the single organ-on-a-chip model, body-on-a-chip model provides information about the combined response of NMs on several organs (or tissues) [212]. Organs-on-a-chip model started with lung-on-a-chip and expanded to cover heart, liver, kidney, breast, gut, and blood vessels, but clinical evaluation of NMs on all these models is not available. It has been reported that the liver is the critical organ affected by the cytotoxicity of NMs. Even though several liver on-a-chip models were developed, very few studies tried to quantify the NMs uptake by liver cells (hepatocytes), its transport, and hepatotoxicity profiles [197]. In general, while developing nanomedicine for any target organ, the effect of NMs on the liver also has to be investigated. In such models, NMs or nanomedicine has to be metabolized in the liver module first and study the action on the target organ. For example, a microfluidic model consisting of a colon tumor, liver, and marrow chamber interconnected using the blood flow behavior of the human body was developed to study the cytotoxicity of nanomedicine [215]. The study evaluated the toxicity of nanomedicine on tumor cells, myeloblasts, and liver cells to measure the tumor-killing effect, hematological toxicity, and hepatotoxicity, respectively.

Shuler and co-workers developed a body-on-a-chip model (Fig. 8b) to study the response from oral uptake of 50 nm carboxylated polystyrene NMs [212]. The model consists of two fluidic circuits; (1) NMs' recirculation through the gastrointestinal (GI) tract and (2) systemic circulation of the human body. GI module cocultures the human intestinal epithelium, which connects with the silicon chip that cocultures other tissues (liver, fat, kidney, and bone marrow) simultaneously. Results revealed that ~9.5% of NMs administered orally could cross the GI barrier and cause liver injury.

Small organisms can be cultured in a microfluidic chip, called the animals-on-a-chip model, which helps evaluate NMs uptake and toxicity profiles [197]. The most extensively studied small organism model is the *Caenorhabditis Elegans* (*C. Elegans*) due to its high homology between their genes and human genes. A PDMS-based chip was developed to study *C. Elegans*' growth and gene expression upon Ag NMs exposure. The chip has an incubation chamber (~1.5 mm length) and an immobilization channel (width tapered from 20 to 100 μm). At their larval stage, *C. Elegans* (~1 mm) were injected into the incubation chamber, incubated in the presence or absence of Ag NMs, and migrated into the immobilization channel for imaging and analysis. The analysis revealed that Ag NMs reduced the size of the *C. Elegans*, which helped them to migrate into the immobilization channel easily. A metal detoxification protein was detected after exposure to NMs, indicating the genotoxicity induced by Ag NMs [216]. The device can be coupled with real-time polymerase chain reaction analysis to discover which gene is overexpressed due to NMs exposure. In the future, rapid growth in body-on-a-chip and animal-on-a-chip models are expected due to their advantages in quantifying the combined effect of NMs on each organ and its tracking.

A detailed description of the various microfluidics model and NMs' clinical evaluation parameters are listed in Table 3. NMs' hemocompatibility is evaluated using a blood vessel on-a-chip model. For studying NMs transport, blood vessel on-a-chip, blood-brain barrier, and lung-on-a-chip model are used. NMs uptake and toxicity effects can be evaluated using single-cell microfluidics, tumor on-a-chip, organs-on-a-chip, and animals-on-a-chip models. NMs accumulation analysis uses tumor-on-a-chip model, while NMs efficacy employs tumor-on-a-chip and blood vessel on-a-chip model. The afore-mentioned examples used cell lines rather than primary cells and animal tissues rather than human tissues. To mimic the human tissues and organs, primary cells and human tissues are preferred. To solve this issue, a more complex or sophisticated microfluidic system is required to mimic the actual human physiological environment at a microscale level. In general, to do the clinical translation of NMs for wider industrial use, high throughput fabrication and screening compatibility of the microfluidic systems have to be considered. An appropriate balance should be there between model sophistication and model throughput for final industrial usage. Also, a standardized microfluidic model and protocols have to be built for NMs for specific biomedical applications. It can speed up the clinical

Table 3
Summary of essential works on clinical evaluation of NMs using microfluidics.

Composition	Shape	Size (nm)	Microfluidic Model	Clinical Evaluation Parameters	Ref.
Ag	Sphere	96.4 ± 35.6	Animals on-a-chip	Nanotoxicity and genotoxicity	[216]
Protein loaded high-density lipid	Sphere	~50	Blood-brain barrier	NMs uptake and transport	[204]
Au@citric acid & Au@DNA	Sphere	15,30 & 60	Single cell microfluidics	NMs uptake and transport, NMs accumulation	[207]
TiO_2 ZnO	Sphere	25 (TiO_2) 40 (ZnO)	Lung on-a-chip	Nanotoxicity	[208]
DOX coated fullerene-silica	Sphere	~60	Tumor on-a-chip	Efficacy	[202]
Carboplatin	–	312	Tumor on-a-chip	Efficacy	[217]
Polystyrene with anionic and cationic surface charge	Sphere	100	Spheroid on-a-chip	NMs penetration and accumulation	[211]
Amine modified polystyrene	Sphere	100	Blood-brain barrier	NMs transport	[199]
Magnetic NMs	Sphere	~18	Blood vessels on-a-chip	Hemocompatibility	[198]
Verteporfin loaded Oil-polyelectrolyte	Core-shell	<120	Tumor on-a-chip	Cytotoxicity and NMs accumulation	[213]
Ovalbumin conjugated Au	Rod	–	Single cell microfluidics	NMs uptake and toxicity	[200]
Silica, ZnO, Fe_2O_3, Ag and CeO_2	Sphere	14.7 (silica) 4.03 (CeO_2) 17.7 (ZnO) 13.7(Ag) 19.7 (Fe_2O_3)	Single-cell microfluidics	Genotoxicity and cytotoxicity	[205]
QDs	–	–	Single-cell microfluidics	NMs accumulation and cytotoxicity	[206]
PEGylated Au	Sphere	40, 50, 70, 110, 150 & 160 (hydrodynamic diameter)	Tumor on-a-chip	NMs accumulation	[214]
Carboxylated polystyrene	–	50	Body on-a-chip	NMs transport and uptake	[212]
Fluorescent NMs	–	20	Lung on-a-chip	NMs uptake	[201]

evaluation process and possible to compare different models and NMs.

5. Microfluidic nanomaterials for biomedical applications

The interplay among material science, microfluidics, clinical engineering, and microbiology fields gifted many diversities of biomedical applications using NMs synthesized from the microfluidic platform. Compared to the conventional batch synthesis method, NMs synthesized from microfluidics showed superior qualities, essential for biomedical application. For example, conventional bulk reactors execute each process step discretely for nano carrier-based drug delivery, which is time-consuming. On the other hand, microfluidics can execute everything (from synthesis to delivery) in a single chip within 3 min [218]. Also, microfluidic technology has offered a higher degree of encapsulation and loading efficiency with drugs [149,219]. In addition, the biostability and biological performance of NMs synthesized by microfluidic technology are higher than the conventional method, further enhancing biomedical field usage [73]. Overall, microfluidics provides the versatile design of NMs with higher loading efficiency as nanocarrier [26,68], high photoluminescence activity [162,169], high drug encapsulation capability [151,220], biodegradability and biocompatibility properties [26,33,178], ease of functionalization, and good thermal and electrical conductivity [26,28,29] compared to its bulk synthesis counterpart. Due to these features, microfluidic NMs have tremendous biological and biomedical applications including biomarkers [23–25], anti-tumour agent [13,30,159], drug and gene delivery vectors [32, 90,221,222], fluorescent probes for bioanalysis [26–29], drug coadjutants [223,224], bio-separation [225], drug delivery [90,149,151, 223], *in vitro and in vivo* imaging [83,166], cellular tracking [38,159], targeting [13,159], therapeutics and [31,220,226] biosensing [227, 228], hyperthermia treatment [166,229], inhibitory effect towards disease [165], cellular proteins fluorescent labelling [27], tumour detection [14,166], and detection of toxin and pathogens [170,227] etc.

All the biological and biomedical applications fall under the four categories; imaging, targeting, therapy, and sensing. This section describes the critical examples of biomedical applications under each category, which uses the NMs synthesized by microfluidic platform, with its current scenario. In addition, we briefly explain the importance of each type with the area it covers and the features of NMs that make them particularly suited for a specific application, and how it functions.

5.1. Imaging

In vivo imaging is an essential tool in medical diagnosis, evolved as a technique to develop targeted therapy [166]. NMs used for imaging purposes should possess minimum toxicity. If they inject intravenously, they should be cleared from the body through renal elimination and should not be uptake by non-targeted tissues. The hydrodynamic diameter of NMs affects the excretion efficiency of NMs. For spherical NMs, the threshold for renal excretion is 6–8 nm, and for core-shell, < 6 nm core size may soon coat with serum protein while circulating through the blood and may block renal excretion. So the use of hybrid NMs for multiple imaging modalities is evolved, thereby improving biodistribution studies [108].

Due to the superior magnetic properties of iron oxide NMs, they are used as MRI contrast agents. RBC-coated iron oxide NMs synthesized using electroporation mediated microfluidics are helpful as MRI contrast agents. The transverse relaxation rate of this nanomaterial is the same as iron oxide NMs. In addition, they possess improved biocompatibility and stability. *In vivo* MRI experiments performed in mice revealed the higher tumor enrichment of RBC coated NMs than that prepared by the conventional method [166]. Similarly, PEG-crosslinked hyaluronic acid NMs loaded with a fluorescent dye (for oligonucleotide labeling) synthesized by hydrodynamic flow focusing method found application in nuclear magnetic resonance relaxometry, which is considered as an alternative to clinical MRI [39]. Magnetic NMs synthesized from the 3D hydrodynamic flow-focusing device were also used in nuclear magnetic resonance studies. They observed that the transverse relaxation rate increased, and the longitudinal relaxation rate decreased with an increase in the hydrodynamic diameter of NMs up to 120 nm. If the NMs coat with alendronate (a drug used to treat and prevent osteoporosis), both relaxivities decreases [83].

In 2013, Kim et al. fabricated a biomimicking high-density lipoprotein in a rapid mixing micro-vortices microfluidic platform. They

established its usage in computed tomography (CT), MRI, and fluorescence microscopy by conjugating with Au, iron oxide, and QDs, respectively, using the same device (Fig. 9a (1)) [38]. During the synthesis process, mixing speed and lipid-protein ratios were varied to optimize the physicochemical properties of NMs (8–9 nm) for imaging modalities. CT imaging activity of Au-lipoprotein was found to be higher than that of Au-PEG, as their uptake by cellular macrophages was more (Fig. 9a (2–5)). Similarly, macrophages incubated with QDs-lipoprotein and iron oxide-lipoprotein showed higher cellular uptake in confocal microscopic and MRI images (Fig. 9a (6–9)), respectively. Advances in material fabrication technology helped to develop engineered hybrid materials in the microfluidic platform in a highly controlled manner. Sometimes, a hybrid nanomaterial without individual surface modification act as a multiple imaging modality contrast agent due to its inherent features. For example, recently, Au@CoFeB-Rg3 nanomedicines fabricated using the programmed microfluidic device were used for multi-mode imaging [30]. Due to the presence of Au core, it was visually tracked; superparamagnetic properties and their strong interaction with X-ray radiation enabled them to trace using MRI and CT imaging modalities. These features help the diagnosis more accurately and visible for both *in vivo* and *in vitro* studies for final clinical applications. Since these nanomedicines are clinically visible, they can be guided to the target organ or tissue using MRI or CT imaging.

In summary, microfluidics-enabled rapid mixing helps to develop hybrid NMs for imaging purposes. By simply varying the precursor concentration, multifunctional hybrid NMs can be synthesized in a highly controlled manner. Progresses in material science helped to fabricate hybrid NMs with inherent features that could be useful as contrast agents in several imaging modalities. For commercialization, these hybrid NMs could be produced in parallel microfluidics arrangement to facilitate reproducibility and controllability, thereby achieving rapid clinical development.

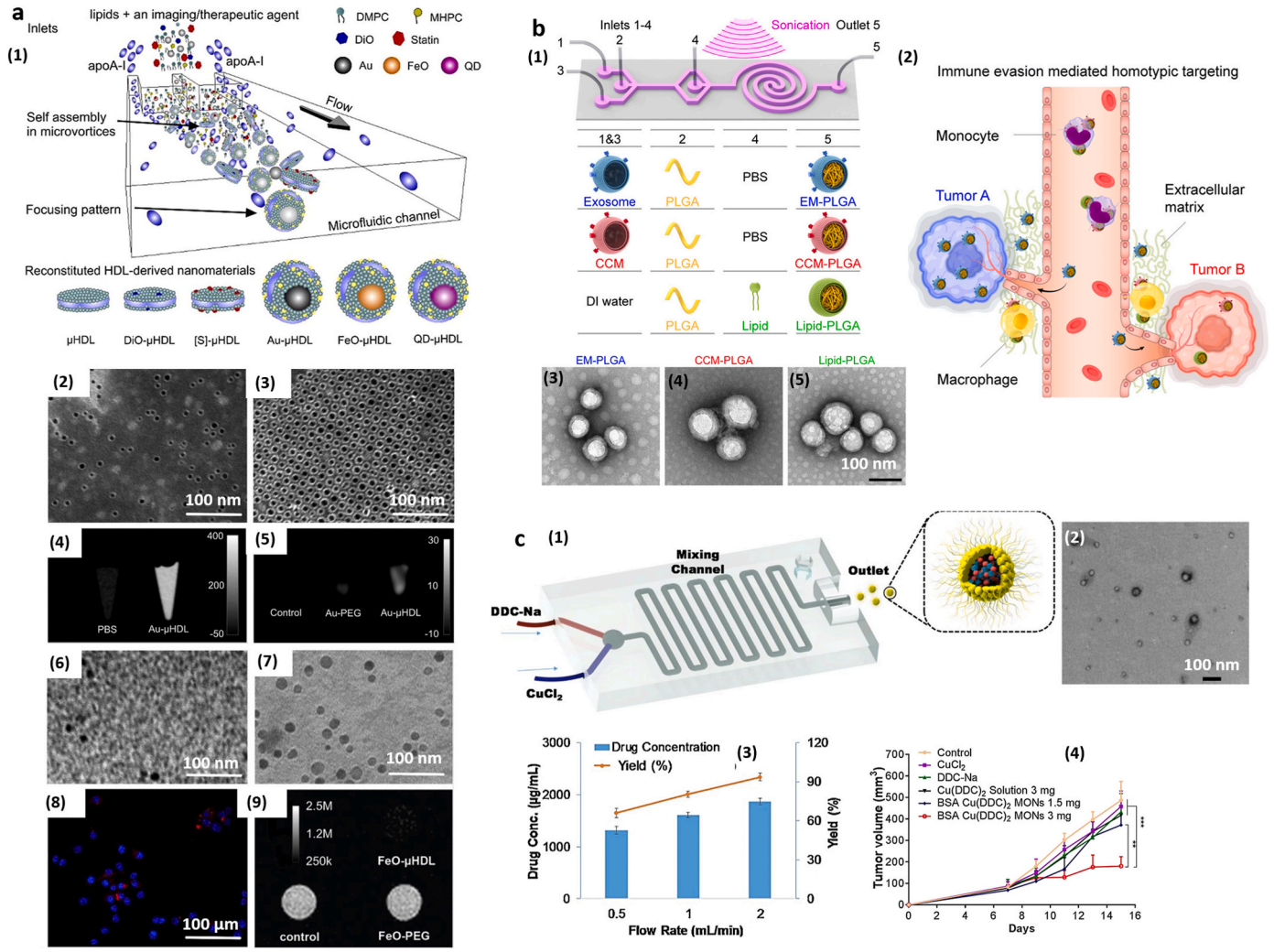

Fig. 9. Imaging, targeting, and breast cancer therapy using the NMs synthesized by the microfluidic platform. **a)** CT, MRI, and fluorescence imaging using μHDL NMs. (1) Schematic illustration of the synthesis of μHDL NMs and its conjugation with Au, iron oxide, and QDs. TEM images of Au-μHDL (2) before and (3) after purification. (4) CT imaging of Au-μHDL and PBS solution. (5) CT images of macrophage cell pellets. (6) TEM image of QDs-μHDL and (7) iron oxide-μHDL. (8) Confocal microscopic image of macrophages incubated with QDs-μHDL. (9) T2-weighted MRI images of macrophages incubated with iron oxide-μHDL. Reproduced with permission [38]. Copyright 2013, American Chemical Society. **b)** Tumour targeting using biomembrane coated PLGA NMs. (1) Schematic illustration of sonication mediated microfluidic chip to synthesize EM, CCM, and lipid-coated PLGA NMs. (2) Immune evasion mediated homotypic tumor targeting of EM-PLGA NMs compared to CCM-PLGA and lipid-PLGA NMs. (3) TEM images of corresponding NMs. Reproduced with permission [159]. Copyright 2019, American Chemical Society. **c)** Breast cancer therapy using biomimetic metal-organic NMs. (1) Schematic representation of the synthesis of BSA/Cu $(DDC)_2$ NMs using a 3D printed microfluidic device. (2) TEM image of synthesized particles. (3) Flow rate dependent drug concentration and yield. (4) Tumour volume changes in 4T1 breast cancer cells. Reproduced with permission [226] Copyright 2020, Elsevier. μHDL-High density lipoprotein synthesized in microfluidics; EM-Exosome membrane; CCM-Cancer cell membrane; BSA-Bovine Serum Albumin; Cu-Copper. (For interpretation of the references to color in this figure legend, the reader is referred to the Web version of this article.)

5.2. Targeting

Microfluidics provides a great platform to target biomolecules and biological or pathological tissues. Specific targeting of pathological tissues should be achieved using NMs and should not disturb any healthy tissues ideally. The parameter enhanced permeability and retention effect alone is not sufficient to distinguish tumor tissues from healthy tissues. For drug delivery purposes in a specific location, the interaction between NMs and the biological environment must be attained. For this purpose, NMs have to conjugate or make a bond with targeting ligands. Targeting ligands include peptides, proteins, aptamers, antibodies, oligosaccharides, and small molecules. Folic acid and Arginine-Glycine-Aspartic peptides have been widely studied as targeting ligands. Small molecules are not common due to the limitation in the specificity of biological recognition [108].

Surface-modified biopolymeric NMs (small and self-assembled) are commonly employed for targeting tumor cells to deliver nucleic acids. For example, monomolecular nucleic acid/lipid NMs (~38 nm) self-assembled with 21 bp (base-pair) double-stranded DNA using hydrodynamic flow focusing micromixing can target epithelial carcinoma cells after modifying the surface with folate-conjugated PEG-lipids [32]. Compared to conventional vortex mixing, microfluidics enabled mixing enhanced a 20% increase in encapsulation efficiency with negligible amounts of aggregation. To increase the encapsulating siRNA, parallelization of the microchannels can be implemented. It could produce an N-fold rise in encapsulated siRNA per hour, where N is the amount of parallelization. In another study, hyaluronic acid nanogel hybrids (80–160 nm) synthesized using a micro-vortices tunable microfluidic chip were found to be a promising candidate for targeted intracellular delivery of therapeutic proteins [13]. Used therapeutic proteins were cytochrome C, saporin, Herceptin, bovine serum albumin, and immunoglobulin G. All the proteins were loaded quickly with nanogel of various sizes and observed that saporin loaded protein releasing depended on the density of cross-linking; highly dense nanogel shown low releasing compared to low dense nanogel within 24 h of administration. In addition, the presence of glutathione (an antioxidant) improved the release of protein. The analysis of native and released saporin protein showed that the loading process does not introduce any significant effect on its structure, but the size of nanogel has an impact on the cellular uptake; compared to 150 nm, 80 nm has higher cellular uptake in the cytoplasm of breast cancer cells. Also, saporin loaded hyaluronic acid nanogels' anti-cancer effect can be improved by introducing a fusogenic peptide, 'GALA.' Its structure changes from the coil to α-helix, thereby promoting fast endosome escape of protein loaded nanogel [13].

Sometimes, biopolymeric NMs coated with a natural membrane can improve tumor-specific targeting. Advances in passive mixing technology enabled the usage of external stimuli to produce biomimetic NMs for targeting purposes. Recently, Liu et al. fabricated biological membrane coated PLGA NMs (<200 nm) using a sonication mediated microfluidic approach (Fig. 9b (1)) and analyzed the tumor-targeting efficiency and cellular uptake [159]. Exosome membrane, cancer cell membrane, and lipid layers were used as natural membranes to coat PLGA NMs. The chip works as follows; ultrasonic wave generates an intensive acoustic pressure field in the microchannel, which creates membrane pores on biological membranes and covers the PLGA NMs with those membranes. Due to the presence of endosomal and plasma membrane proteins on exosome membrane-PLGA NMs, they exhibit lower uptake by circulating monocytes and macrophages than others. It indicates immune evasion assisted targeting of exosome membrane-PLGA NMs. In the *in vivo* tumor targeting experiments, a higher accumulation of exosome membrane-PLGA NMs on the tumor site was observed after 4 h of post-injection, illustrating the superior homotypic targeting of these to the cancer cell membrane and lipid-PLGA nanohybrids. *Ex vivo* imaging also showed similar results; the exosome membrane-PLGA NMs possess higher intensity fluorescence signal followed by the cancer cell membrane and lipid-PLGA NMs in both tumor cells. The liver exhibited a higher fluorescence signal in major organs such as the lung, heart, spleen, and kidney.

Microfluidics synthesized NMs for targeting purpose mainly uses biopolymer NMs or biomimetic NMs. More materials have to be invented for targeting ligand function. Currently, sonication-triggered microfluidics are used to synthesize NMs with favorable features for targeting purposes. In the future, other external stimuli, such as electric field, magnetic field, etc., can also be utilized to fabricate biomimetic NMs in a highly controlled manner and can be compared in terms of their targeting efficiency.

5.3. Therapy

NMs involved in therapy can be nanomedicine, inhibitory effect towards some diseases, gene transfer, gene silencing, photodynamic therapy, or photothermal therapy. Nanomedicines have been considered as an alternative to traditional medicine over the decades due to their superior properties. Nanomedicine can be achieved in two ways; drugs can be either encapsulated on the NMs' structure or grafted on its surface. Even though the gain in efficiency is reported minimal in most cases, other quantities such as sensitivity, tunability, precise targeting, efficacy, and specificity of nanomedicine attracted the scientific community. Another advantage of nanomedicine is better drug solubility and more prolonged *in vivo* circulation time. Still, they may show side effects and alter the drug dosage due to a slowdown in drug release and metabolization rate [108]. NMs used for drug delivery include liposomes, polymer NMs, CNTs, QDs, inorganic nanocrystals, and DNA origami. Morphology includes hollow, mesoporous, or core-shell nanostructures. In nanomedicine, NMs act as drug-carrying vehicles that improve solubility and safety, protect the drug from degradation, deliver to the target and release the drug in a controlled manner [196]. Drug delivery using NMs is quantified using drug delivery efficiency, drug encapsulation efficiency, and drug mass loading capability. The encapsulation efficiency is defined as the fraction of initial drug concentration encapsulated within the NMs compared to the initial drug concentration before encapsulation. The loading capacity is the mass fraction of the encapsulated drug compared to the particle weight [90]. Drug loading efficiency and encapsulation efficiency are higher with NMs synthesized in microfluidic platforms than conventional batch reactors [157]. Commonly employed drugs with nanocarrier are DOX and paclitaxel. DOX is an antibiotic that can inhibit nucleic acid synthesis by binding with DNA. The paclitaxel results in cell death by promoting microtubule assembly [223].

The widely used drug nanocarrier is biopolymer NMs due to their low side effects and enhanced therapeutic effects [157]. Microfluidic-based nanomedicine has been studied extensively in the research sector, and its clinical evaluation is also broadly analyzed. Commonly employed microfluidic approaches for nanomedicine preparation are flow-focusing, micro-vortices, template assembly, flow lithography, chaotic mixing, and droplet formation [230]. In terms of drug delivery, earlier microfluidics was used in fabricating biopolymer NMs alone and drug conjugation was achieved separately, later started synthesizing hybrid NMs with drugs conjugated with it in a single microfluidic platform. Nowadays, multiple drugs are loaded using a single microfluidic device.

Chitosan nanomaterial is an essential drug carrier due to its protecting behavior of drugs from degradation, and it exhibits comparatively increased loading and slow, sustained release of the drug. In one of the studies, chitosan NMs (154 ± 20 nm at 400 μL/min) were synthesized using a microreactor with a magnetic needle embedded into the chamber to promote mixing efficiency [222]. Two approaches were used to load the drug; In the first approach, two chambers were used. Drug and tripolyphosphate flowed through the first chamber along with chitosan NMs and enhanced mixing efficiency in the second chamber. The second approach uses three chambers, and the third chamber actively

loaded drugs on synthesized chitosan NMs. The drug entrapment efficiency was found to be higher with the three chambers method. Thus, the microfluidic process enhances drug loading due to the improved interaction between chitosan NMs and drugs. Also, the drug release profile is biphasic (initial burst followed by slow, sustained release), and its rate is higher with microfluidic mediated drug delivery compared to the conventional method. Slow-release in the conventional batch reactor method is due to diffused drugs from inside of chitosan NMs. Rapid release in microfluidic synthesized chitosan NMs attributes a higher surface area to volume ratio. It can also be interpreted that the interaction forces between drug and chitosan NMs are fragile. Hence the release is through simple dissociation. Apart from drug delivery purposes, these NMs showed antifungal activity against *Candida albicans*, indicating good hemocompatibility [222].

In another study, encapsulation efficiency and loading capacity of hydrophobic (tamoxifen) and hydrophilic (DOX) drugs were optimized by tuning the flow rate and concentration ratio in a coaxial flow microreactor [90]. At the lower flow rate, encapsulation efficiency (57–89%) and loading capacity (11–18%) were higher for tamoxifen than DOX. On the other hand, encapsulation efficiency and loading capacity of DOX were increased with an increase in concentration ratio. Besides, solvent dichloromethane helps concentrate more drugs in the hydrophobic core of NMs, by shrinking towards the core during the evaporation process, thereby facilitating the sustained release of the drug. This is very important since the drug DOX degrade within a few hours after solubilizing in an aqueous medium. Compared to DOX, tamoxifen has a higher solubility in dichloromethane due to its hydrophobicity. Hence tamoxifen-loaded PLGA NMs are larger compared to DOX loaded PLGA NMs.

Sometimes, NMs which mimic the biological activity can be prepared using microfluidics for therapeutical purposes. In our body, disulfiram reacts with Cu to form a complex molecule, which possesses anti-cancer activity, but relatively low solubility makes it clinically challenging to achieve. Recently, biomimetic metal-organic NMs/drug (~63 nm) consisting of complex molecule core and BSA shell were synthesized on a large scale using a 3D printed microfluidic device with vortex mixing (Fig. 9c) [226]. Flow rate controlled the drug concentration and loading; the higher flow rate favored higher drug concentration and yield due to better mixing. In addition, these NMs effectively inhibited tumor growth in breast tumor cells and 3D cultured tumor spheroids.

Selective killing of tumor cells is possible by developing NMs with tumor microenvironment triggered drug delivery. Compared to single stimuli nanocarrier, multiple stimuli can effectively deliver the drug, as numerous stimuli act into the tumor site. Hence, combining the drugs in such a way to achieve co-delivery is an effective and active way of treating many solid tumors [223]. It can also suppress drug resistance and severe adverse effects [224]. For example, Liu et al. synthesized porous silicon conjugated acetylated dextran nanocomposites and loaded paclitaxel, sorafenib, and methotrexate drugs to treat the breast cancer cells using a 3D microfluidic co-flow device [224]. Among the prepared NMs, methotrexate conjugated NMs showed a relatively higher loading due to their large surface area and pore volume. It was also found that relatively low pH (~5) is needed for sustained drug release. Higher pH (~7.4) can tightly pack the drugs, and hence no drugs were released. The step-change in pH also supports this phenomenon; when pH changed from 7.4 to 5, it was observed from no delivery to the delivery of all three drugs at the same rate.

Like biopolymer NMs, mesoporous and hollow silica NMs fabricated using spiral microreactors are helpful as a drug carrier, and they exhibit pH-responsive long-term drug delivery [149,151]. The mesoporous silica has been studied extensively for smart drug delivery due to its easy chemical modification, excellent biocompatibility, and high encapsulation capacity. In mesoporous silica nanosheets, the drug encapsulation rate can be increased by increasing the flow rate [151]. In another recent study, a microfluidic mediated drug delivery system was developed using pH or redox triggered mesoporous silica NMs for the co-delivery of DOX and paclitaxel (Fig. 10a (1)) [223]. The DOX was loaded into the mesoporous silica, and paclitaxel was conjugated with mesoporous silica through a redox-sensitive linker that can enhance and control the loading degree, stability, and solubility of hydrophobic paclitaxel drug. Also, the NMs' surface was coated with Polystyrenesulfonate to make them acidic responsive and neutralize the surface charge required to reduce the damage to healthy tissues. The paclitaxel and DOX release profile (Fig. 10a (2&3)) reveal that the presence of DL-dithiothreitol enhances the paclitaxel release, and dithiothreitol and pH mainly influenced DOX release. In the co-delivery of paclitaxel and DOX, conditions such as Polystyrenesulfonate layer with acidic responsive and paclitaxel layer with redox response should meet simultaneously. Under acidic conditions, electrostatic interaction between Polystyrenesulfonate and mesoporous silica declines due to the attraction of unmodified amino group of mesoporous silica and protons, which leads to swelling and pore formation on Polystyrenesulfonate membrane. This results in reduced attraction of DOX with Polystyrenesulfonate, thereby release DOX rapidly [223].

Certain multifunctional hybrid nanostructures can combine the inherent properties of individual structures, showing an inhibitory effect on some diseases. For example, Hassan et al. showed the possibility of using multifunctional magneto plasmonic nanostructures synthesized using the microfluidic device in treating Alzheimer's disease [165]. Hybrid nanostructures were formed by assembling peptide-functionalized iron oxide NMs (26.7 ± 0.2 nm) and chitosan modified Au nanorod (69 ± 5 nm), maintaining their magnetic and plasmonic properties. This hybrid nanostructure formation helped inhibit fibril formation without causing any cytotoxicity, thereby opening Alzheimer's disease treatment. In another study, folate functionalized monomolecular nucleic acid/lipid NMs synthesized using microfluidic hydrodynamic mixing and loaded with green fluorescent protein-siRNA were successfully used for regulating gene expression [32]. These NMs bind with folate-receptor-expressing epithelial cancer cells, and cells can internalize the NMs within 20 min of binding.

Photothermal therapy is the most common application of plasmonic NMs (noble metals, QDs, etc.) synthesized using microfluidic devices. These NMs are important in photothermal therapy due to their plasmonic photoexcitation, converting absorbed light into heat energy. Photothermal therapy refers to the exposure of cells incubated with plasmonic NMs with radiation in the near-infrared region; NMs absorb the light with a plasmonic peak located at the near-infrared region and lead to nanoscale heating of the nanomaterial environment. Various plasmonic nanostructures were illustrated in the literature for this therapy. Noble metal NMs, specifically Au and nanohybrids formed by iron oxide-based magnetic NMs and silica NMs, have excellent plasmonic properties, which are useful for cancer therapy. For example, biomimetic cell membrane coated magnetic NMs synthesized using an electroporation-mediated microfluidics platform (Fig. 10b) possesses an absorption peak at 400 nm due to the RBC membrane and another peak at 808 nm due to magnetic NMs core [166]. Expose to laser at ~808 nm on tumor cells after incubating NMs, revealed that temperature increased in the region within 5 min. Also, complete tumor inhibition was observed in the mice treated with these NMs and laser irradiation. Further, it is assumed that the anti-tumor effect can be enhanced by applying an external magnetic field. Photothermal therapy can deliver exogenous molecules into the cells, which is an essential strategy in cellular therapy. Laser irradiation generates membrane pores, and through the pores, exogenous molecules can be delivered. Polymer-nucleic acid nanocomplex prepared using emulsion droplet microfluidic device were used to load plasmid DNA and mRNA into the stem cells [73].

In summary, inherent features of microfluidics enabled the controlled synthesis of biopolymer and silica NMs that can easily encapsulate drugs. A critical factor in conjugating drugs or other molecules with NMs is the rapid mixing of formulations; microfluidics with various mixing geometries favored rapid mixing. Other than drugs,

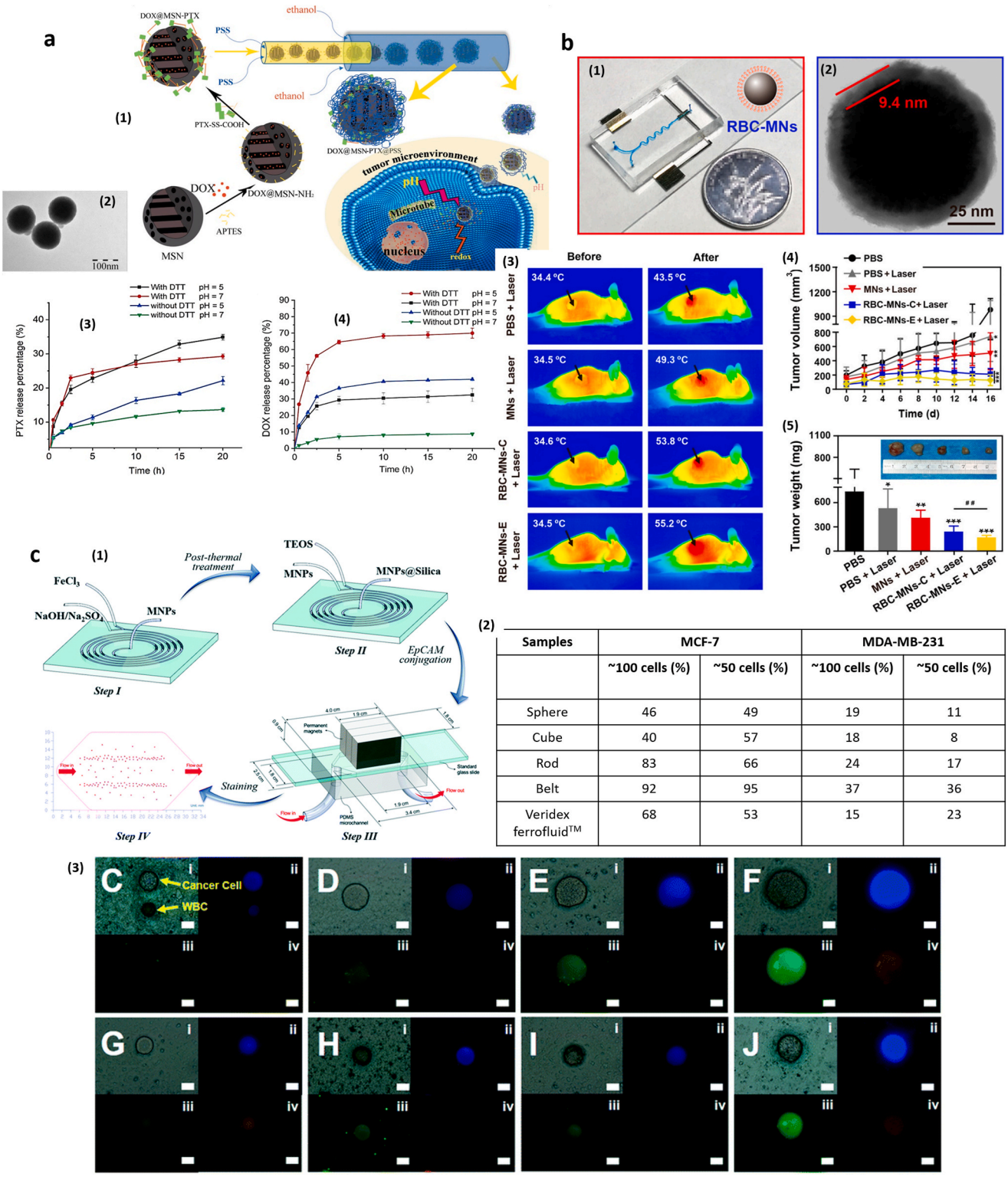

(2)

Samples	MCF-7		MDA-MB-231	
	~100 cells (%)	~50 cells (%)	~100 cells (%)	~50 cells (%)
Sphere	46	49	19	11
Cube	40	57	18	8
Rod	83	66	24	17
Belt	92	95	37	36
Veridex ferrofluid™	68	53	15	23

Fig. 10. Therapy and sensing using microfluidic synthesized NMs. **a)** Controlled release of multiple drugs using the nanomedicine synthesized from the microfluidic device. (1) Schematic illustration of the synthesis of DOX@MSN-PTX and DOX@MSN-PTX@PSS. (2) TEM characterization of DOX@MSN-PTX@PSS. The drug release profile of (3) PTX and (4) DOX. Reproduced with permission [223]. Copyright 2020, American Chemical Society. **b)** RBC coated magnetic NMs for PTT and tumor inhibition. (1) Photograph of the electroporation mediated microfluidic chip. (2) TEM image of a single RBC-Magnetic NMs. (3) *in vivo* infrared thermal images of mice treated with PTT. (4) Tumour volume curve after the treatment. (5) Average tumor weight of the various group. Reproduced with permission [166]. Copyright American Chemical Society, 2017. **c)** Screening of CTC using immunomagnetic NMs. (1) Schematic representation of synthesizing immunomagnetic NMs using two five-run spiral-shaped microreactors. Step 1 prepares Magnetic NMs, silica shell coats in step 2, functionalization using Ep-CAM and screening of CTC in step 3, and analysis of screening performance in step 4. (2) Screening efficiency of tumor cells (MCF-7 and MDA-MB-231) using various shaped NMs. (3) Representative images of captured MCF-7 cells using sphere, cube, rod, and belt in (C–F) and captured MDA-MB-231 in (G–J). All the scale bar denotes 20 μm. Reproduced with permission [228]. Copyright 2018, Royal Society of Chemistry. PTX-Paclitaxel; MSN-Mesoporous silica NMs; PSS-Polystyrenesulfonate.

molecules such as mRNA, siRNA, etc., can also be conjugated with biopolymers in microfluidics to treat cancers, genetic disorders and to develop vaccines against infectious diseases. Scale-up synthesis of these hybrid NMs has to be considered for rapid screening and commercialization. In the future, it is expected to synthesize more NMs with inherent features towards anti-disease activity or inhibition properties within microfluidics to promote the therapy against various diseases. In addition, photothermal and photodynamic therapy using hybrid NMs synthesized using microfluidics helps to kill tumor areas or repair wound-tissue by generating heat and producing reactive oxygen species, respectively. Even though tissue wound repair using NMs based photodynamic therapy is common, microfluidics synthesized NMs have to be explored in this area in detail.

5.4. Sensing

The NMs based biosensing showed high sensitivity due to its high surface-to-volume ratio. Since microfluidic device-based synthesis favors high surface-to-volume ratio NMs, biosensing can be achieved easily using these materials. The NMs' surface needs to be optimized for biological recognition specificity by restricting the interaction with other specific biological recognition. The commonly employed biosensing techniques such as enzyme-linked immunosorbent assay and surface-enhanced Raman spectrum have been assimilated with NMs, and they exhibited improved detection sensitivity [108].

Polymer/noble metal hybrid NMs, namely polymer-coated Au NMs, can be used as a colorimetric probe for sensing serum copper ions [227]. These NMs were fabricated using a droplet-based microfluidic device. Without copper ions (before adding serum), the polymer coating improved stability by preventing aggregation. With the addition of copper ions, the amino group in the NMs reacts with ions due to the empty orbital of copper. Thereby increasing the particle size, increasing the plasmonic intensity with a redshift, and improving copper ions' specificity.

One of the non-invasive methods for screening cancer is the isolation and detection of circulating tumor cells from the blood. Functionalized magnetic NMs with an external magnetic field can capture circulating tumor cells. Hao et al. synthesized four distinct shapes (sphere, rod, cube, and belt) of immunomagnetic NMs using a spiral microreactor for screening circulating tumor cells from the whole blood. They analyzed

Table 4
Review of recent works in biomedical applications of NMs synthesized using microfluidics.

Composition	Shape	Size (nm)	Type of microfluidic device	Tuning parameters	Category of biomedical application	Ref
Curcumin and catechin loaded liposomes	Core-shell	200	Hydrodynamic flow focusing	Molar ratio	Anti-cancer activity and drug loading	[231]
Sorafenib loaded lipid polymer hybrid	Core-shell	191.8 ± 0.4 to 302.0 ± 2.0	Co-flow nanoprecipitation	Inner and outer flow rates	Cancer chemotherapy	[232]
PTX and SFN loaded particles	Core-shell	60-450 (PTX) 70-550 (SFN)	Three sequentially nested cylindrical glass capillary	Reynolds number (flow rate)	Drug delivery	[233]
Paclitaxel loaded chitosan	Sphere	–	T-shaped hydrodynamic flow focusing	Flow ratio, velocity, incubation temperature, pH, and drug concentration	Drug delivery	[234]
Polymer-nucleic acid	Core-shell	–	microfluidic cross-flow droplet generator chip	Cell types	delivery of both plasmid DNA and messenger RNA payloads	[73]
MNPs @ SiO_2	Core-shell of sphere, rod, cube, and belt	5-10 (shell thickness)	Spiral microreactor	Flow rates	Screening and analysis of CTC biomarkers	[25]
DOX loaded PLGA	Sphere	~100	Hydrodynamic flow focusing	Mixing geometry, flow rate, and incubation time	Drug delivery	[235]
Liposomal drug	Core-shell	191.5 ± 33.4 (with AO) and 190.9 ± 43.0 (with DOX)	Flow focusing and counter flow microdialysis	pH and flow velocities	Drug delivery	[218]
Magnetic nanohybrids	Core-shell	3.2 ± 0.3 2.4 ± 0.3 (core) 1.2 ± 0.1 (shell)	Programmed microfluidic approach	Metal concentration	Contrast agents for MRI	[236]
Rigid pH-sensitive nanocomplex	Core-shell	50-190 (average)	SF; hexagon and spiral mixing geometry	Mass ratio, drug concentration, and pH	Drug delivery	[160]
Lipid-PLGA	Core-shell; bilayer and monolayer lipid	103.67 ± 8.51 (monolayer) 106.43 ± 6.75 (bilayer)	Straight channel and double spiral mixing	Reagent injecting order	Cancer drug delivery	[154]
Lipid-PLGA with water core	Hollow rigid nanovesicle	140 (hydrophilic core)	The straight and hexagonal channel followed by spirals	Type of reagent loading	Delivery of hydrophilic reagents (cancer treatment to *in vivo* imaging diagnosis)	[31]
Carbon QD-PLGA	Core-shell	100–150	Pattern tunable micro vortex	Mass ratio, nanoparticle concentration, and type of antibiotics	Chemo photothermal therapy against bacterial biofilms and antibiotic delivery	[170]
BSA-QD	Sphere	1.5	Temperature controlled microfluidic device	Type of bioconjugate	Optical probe for bioimaging,	[28]
Polymer dots	Sphere	20	Droplet generator	Dopamine concentration and excitation wavelength	Fluorescent sensing of dopamine	[27]
NH_2 functionalized UiO-66	Octahedral crystals	80–110	T mixer followed by reaction zone	Flow rate and residence time	Drug delivery	[171]
Curcumin loaded PLGA	Sphere	200 (PLGA)	Staggered herringbone structure	Total flow rate, flow rate ratio and functionalization	Drug delivery	[36]
PLGA	Sphere	35–350	Hydrodynamic flow focusing	Polymer concentration	Drug delivery	[237]
Docetaxel loaded PLGA-PEG-Mal	Core-shell micelle	72 ± 1	Y-junction and hexagonal channel	Docetaxel concentration	Multiple drug delivery for lung cancer treatment	[220]

the shape dependency on capturing the cells (Fig. 9c) [228]. The microfluidic chip of two spiral microreactors with five turns was used for synthesis purposes; one reactor fabricates magnetic NMs while, second coats the silica shell on the magnetic structure to stabilize the NMs. Later, NMs were conjugated with targeting antibodies. Flow rates of first and second reactors were tuned to control the shape of NMs and thickness of the silica shell, respectively. For screening, another PDMS-based microfluidic chip (Fig. 10c (2)) having a hexagonal-shaped chamber (34x18x0.5 mm) and permanent magnets of alternating polarities kept outside were used. When a blood sample flows through the microchannel, circulating the functionalized immunomagnetic NMs can capture tumor cells. They can be attracted within the channel substrate by magnets. After the screening process, detected circulating tumor cells could be analyzed by staining immunofluorescent for counting, identification, etc. Also, it was observed that circulating tumor cells screening depends on the shape of NMs and the cancer cell type (Fig. 9c (3)); In tumor cell-spiked whole blood samples, belt-shaped NMs with the largest aspect ratio showed the highest capture rate followed by the rod, sphere, and cube.

Other recent works in biomedical applications of NMs synthesized using microfluidics are listed in Table 4, along with their properties, device geometry, and tuning parameters. It is observed that microfluidics synthesized NMs based therapy was extensively studied, and most of them used biopolymer NMs. Due to the improved mixing efficiency compared to the conventional batch reactor, microfluidics facilitated controlled synthesis of core-shell, drug-loaded, or assembly of NMs essential for various biomedical applications. Most of the biomedical applications reported in this section are performed other than microfluidic devices. In the future, it is expected to utilize the full advantages of microfluidic flow to develop NMs synthesis, screening of parameters, clinical evaluation, and application in a cascaded microfluidic platform such as reported by Hao et al. [228]. In addition, more *in vivo* studies are expected, and parallelization of microfluidic channel enabling scale-up synthesis of reproducible NMs in a high throughput manner could speed up the commercialization of applications.

6. Summary and future perspectives

Microfluidics is a growing field considered the most promising platform for synthesizing NMs in a controlled manner for biomedical applications. The small surface-to-volume ratio is the critical feature of microfluidics that imparts several advantages. Microfluidics NMs are homogenous with a narrow size distribution, highly reproducible, easy scale-up validation, and possess tunable physicochemical properties. It can efficiently synthesize noble metal, silica, biopolymer, iron oxide, QDs, carbon-based, rare-earth-based, and other NMs commonly employed in biomedical applications in a highly controlled manner. The tuning parameters include the flow rate (or residence time), temperature, molar ratio, pH, geometry and dimension of the device, etc. In addition, as most NMs synthesis demands high reaction temperature, the material that can withstand high temperature has to be invented. Further, that material should be transparent (like PDMS) so that monitoring of reaction process is easy. Currently, NMs are synthesizing with the help of external stimuli and shown physicochemical properties dependent on stimuli strength. Integration of real-time monitoring devices with the microfluidic platform has been demonstrated for parameter screening. This had multiplied the capability for producing NMs within a short time. Several software has been adopted to control these parameters, resulting in "intelligent synthesis" that automates the process and minimizes user dependency. The majority of the recent works in QDs synthesis are fully automated due to easy monitoring of photoluminescence, and developing a control algorithm in this regard is straightforward. Most importantly, microfluidics can adapt to the microphysiological environment, and control the dynamic flow behavior and concentration gradient. It enables a clinical evaluation of NMs within microfluidics, which is an essential step prior to the clinical use of NMs. NMs synthesized using microfluidics have shown tremendous improvement in properties relevant to specific biomedical applications, including surface-enhanced Raman signal enhancement, imaging as a contrast agent, improved encapsulation efficiency, higher loading capacity in drug delivery, multiple drug delivery, improved inhibitory effects towards cancer, encapsulation of molecules in a single step, long term stability in protein immobilized materials, etc. Thus, the microfluidic device offers a controlled synthesis of NMs for biomedical applications and easy clinical translation.

Despite the several advantages offered by microfluidic devices over conventional batch reactors, it suffers from intrinsic limitations. For instance, most microfluidic devices are fabricated using lithography technique, which requires a cleanroom facility. The commonly used photoresist molds such as SU-8 are costly. Conventional batch reactor does not require a clean room facility or costly photoresists to synthesize NMs. Next issue is the low production quantity due to minimal operating volume. Low reagent consumption is the biggest advantage of microfluidics for NMs synthesis, that helps to reduce the cost and wastage. However, this limits the production rate to grams per hour even after increasing the flow rate [68]. Very few reports are available on the scaled-up production of NMs utilizing parallel microreactors or combinatorial reactors [182,238]. Compared to conventional batch reactors synthesized NMs, microfluidics synthesized NMs contains extra reagents such as oil, toluene, etc. (multiphase flow). It requires extra effort for the complete removal of these reagents before clinical usage. Widely used device materials such as PDMS and PMMA lack high-temperature resistance and possesses low solvent compatibility. Another issue is clogging associated with the microchannel in PDMS, which may adversely alter the reagent mixing [59]. At present, inline control for real-time analysis is seldom available for biomedical NMs [68,161].

For biomedical applications, the most crucial part is the clinical translation of NMs, which is still in its infant stage. Most of the applications explained in this review are laboratory proof of concept. Clinical translation further demands application-specific synthesis of NMs in sufficient quantity and *in vivo* and *in vitro* validation [239]. Hence, a long way has to travel to achieve the clinical translation of NMs synthesized by microfluidic devices. Very few demonstrated rapid screening and the quick evaluation of NMs under microenvironment for biomedical applications.

Nevertheless, it is expected that in the future more research in the rapid assessment of NMs for biomedical applications in a microfluidic platform. Biopolymer NMs-based drug delivery has been studied extensively. In the future, similar trends in other domains such as imaging, sensing, targeting, and photothermal therapy are expected by utilizing the relevant features of microfluidics. PLGA based drug delivery was successfully implemented in the clinical sectors. Yet, such particles' mass production in microchannels is still challenging due to the clogging of particles in materials like PDMS. Also, it is challenging to obtain sophisticated channels in materials such as glass and Teflon [240]. Therefore, efforts are on to develop clogging-free materials for microchannels in the future.

Biomimicking NMs are another category of NMs that can be easily synthesized in microfluidics, probably the future clinical market's bottleneck. Few studies utilized microfluidics' features and external energy sources to generate these NMs [38]. Similarly, biological environment mimicking NMs is also possible, as the microchannels can quickly adapt to physiological flow conditions and chemical gradients. For example, any biological mechanism that produces anti-cancer activity within our body can be transformed into microchannels. That kind of particular materials can be prepared, thereby opening the window for a new therapy mode. At present, most of the microfluidic device material faces the fouling issue, which is expected to be overcome by using bioinspired smart material design [126]. It further leads to new biofabrication technologies such as 4D bioprinting, adding a new dimension to 3D bioprinting, like shape change upon applying stimuli.

NMs to deliver therapeutic agents are of great interest nowadays due

to the emergence in vaccines based on mRNAs such as in infectious diseases like coronavirus disease-2019 (COVID-19), cancer or genetic disorder treatment, and nanotechnology provides a platform to achieve the same. Lipid NMs have been investigated in detail, and they were successfully used as a delivery agent in developing two vaccines (mRNA-1273 and BNT162b) against COVID-19 [241]. To use lipid-mRNA NMs for therapeutic purposes, produced NMs should be highly stable, and the stability depends on how fast formulations are mixed. This rapid mixing can be easily achieved in a microfluidic platform; through electrostatic interaction, mRNA could be attached to the core of the interior of lipid molecules [241]. Further, scale-up production of lipid-based NMs has been reported [187] and could be used to develop highly stable lipid-mRNA NMs in a precisely controlled manner for industrial purposes. In addition, this might help fight against several infectious diseases and genetic disorders. In the future, microfluidics can develop next-generation lipid NMs and deliver other categories of molecules, which further enhances the therapies for a broader range of diseases, thereby improving healthcare.

New material design and modification in existing materials, and fabrication technologies are expected in the coming years. However, the complete automated process for synthesis, screening, and clinical evaluation is challenging to achieve in the near future. The screening performs on the crude reaction product, whatever the optimization algorithm or complexity exists in screening parameters and optimizing the process. Product purification is a crucial stage in NMs synthesis. If we can integrate components for this purpose, it will be an outstanding achievement in microfluidic-based NMs synthesis [180]. We expect to implement external energy-based centrifuging within the microfluidics to purify the NMs solution after synthesis. For example, external electric fields with opposite polarities can provide rotations in NMs solution, and enough centrifuging can be achieved with sufficient voltage. We hope the microfluidics domain is expected to focus on the clinical evaluation of NMs as it is the major bottleneck in the procedure towards the biomedical application of NMs.

Declaration of competing interest

The authors declare that they have no known competing financial interests or personal relationships that could have appeared to influence the work reported in this paper.

Acknowledgments

This work was supported by DBT/Wellcome Trust India Alliance Fellowship grant number IA/E/16/1/503062 awarded to Dr. Tuhin Subhra Santra.

References

[1] G.M. Whitesides, The origins and the future of microfluidics, Nature 442 (2006) 368–373, https://doi.org/10.1016/j.agee.2012.07.026.
[2] B. Antes, P. Oberkleiner, A. Nechansky, O.H.J. Szolar, Qualification of a microfluidics-based electrophoretic method for impurity testing of monoclonal antibodies, J. Pharmaceut. Biomed. Anal. 51 (2010) 743–749, https://doi.org/10.1016/j.jpba.2009.09.022.
[3] C. Situma, M. Hashimoto, S.A. Soper, Merging microfluidics with microarray-based bioassays, Biomol. Eng. 23 (2006) 213–231, https://doi.org/10.1016/j.bioeng.2006.03.002.
[4] A. Zubair, P.D. Burbelo, L.G. Vincent, M.J. Iadarola, P.D. Smith, N.Y. Morgan, Microfluidic LIPS for serum antibody detection: demonstration of a rapid test for HSV-2 infection, Biomed. Microdevices 13 (2011) 1053–1062, https://doi.org/10.1007/s10544-011-9575-x.
[5] N.K. Inamdar, J.T. Borenstein, Microfluidic cell culture models for tissue engineering, Curr. Opin. Biotechnol. 22 (2011) 681–689, https://doi.org/10.1016/j.copbio.2011.05.512.
[6] C.J. Bettinger, J.T. Borenstein, Biomaterials-based microfluidics for engineered tissue constructs, Soft Matter 6 (2010) 4999–5015, https://doi.org/10.1039/c0sm00247j.
[7] M. Kitsara, D. Kontziampasis, O. Agbulut, Y. Chen, Heart on a chip: micro-nanofabrication and microfluidics steering the future of cardiac tissue engineering, Microelectron. Eng. 203–204 (2019) 44–62, https://doi.org/10.1016/j.mee.2018.11.001.
[8] S.G.M. Uzel, A. Pavesi, R.D. Kamm, Microfabrication and microfluidics for muscle tissue models, Prog. Biophys. Mol. Biol. 115 (2014) 279–293, https://doi.org/10.1016/j.pbiomolbio.2014.08.013.
[9] I. Ullah, C.A. Serra, N. Anton, T. Vandamme, Microfluidics: a focus on improved cancer targeted drug delivery systems, J. Contr. Release 172 (2013) 1065–1074.
[10] L. Zhang, Q. Chen, Y. Ma, J. Sun, Microfluidic methods for fabrication and engineering of nanoparticle drug delivery systems, ACS Appl. Bio Mater. 3 (2020) 107–120, https://doi.org/10.1021/acsabm.9b00853.
[11] E. Blanco, H. Shen, M. Ferrari, Principles of nanoparticle design for overcoming biological barriers to drug delivery, Nat. Biotechnol. 33 (2015) 941–951, https://doi.org/10.1038/nbt.3330.
[12] S. Damiati, U.B. Kompella, S.A. Damiati, R. Kodzius, Microfluidic devices for drug delivery systems and drug screening, Genes 9 (2018), https://doi.org/10.3390/genes9020103.
[13] K. Huang, Y. He, Z. Zhu, J. Guo, G. Wang, C. Deng, Z. Zhong, Small , traceable , endosome-disrupting , and bioresponsive click nanogels fabricated via microfluidics for CD44-targeted cytoplasmic delivery of therapeutic proteins, ACS Appl. Mater. Interfaces 11 (2019) 22171–22180, https://doi.org/10.1021/acsami.9b05827.
[14] D.C. Wimalachandra, Y. Li, J. Liu, S. Shikha, J. Zhang, Y.C. Lim, Y. Zhang, Microfluidic-based immunomodulation of immune cells using upconversion nanoparticles in simulated blood vessel-tumor system, ACS Appl. Mater. Interfaces 11 (2019) 37513–37523, https://doi.org/10.1021/acsami.9b15178.
[15] M. Unni, J. Zhang, T.J. George, M.S. Segal, Z.H. Fan, C. Rinaldi, Engineering magnetic nanoparticles and their integration with microfluidics for cell isolation, J. Colloid Interface Sci. 564 (2020) 204–215, https://doi.org/10.1016/j.jcis.2019.12.092.
[16] M. Winter, T. Hardy, M. Rezaei, V. Nguyen, D. Zander-Fox, M. Ebrahimi Warkiani, B. Thierry, Isolation of circulating fetal trophoblasts using inertial microfluidics for noninvasive prenatal testing, Adv. Mater. Technol. 3 (2018) 1–10, https://doi.org/10.1002/admt.201800066.
[17] X. Xu, Z. Jiang, J. Wang, Y. Ren, A. Wu, Microfluidic applications on circulating tumor cell isolation and biomimicking of cancer metastasis, Electrophoresis 41 (2020) 933–951, https://doi.org/10.1002/elps.201900402.
[18] L. Wu, L. Zhu, M. Huang, J. Song, H. Zhang, Y. Song, W. Wang, C. Yang, Aptamer-based microfluidics for isolation, release and analysis of circulating tumor cells, TrAC Trends Anal. Chem. (Reference Ed.) 117 (2019) 69–77, https://doi.org/10.1016/j.trac.2019.05.003.
[19] K. Niciński, J. Krajcz, A. Kudelski, E.W.J. Trzcińska, Detection of circulating tumor cells in blood by shell-isolated nanoparticle – enhanced Raman spectroscopy (SHINERS) in microfluidic device, Sci. Rep. 9 (2019) 1–14.
[20] M.T. Vitor, S. Sart, A. Barizien, L.G. De La, C.N. Baroud, Tracking the evolution of transiently transfected individual cells in a microfluidic platform, Sci. Rep. 25–28 (2018), https://doi.org/10.1038/s41598-018-19483-y.
[21] H.N. Joensson, H. Andersson Svahn, Droplet microfluidics-A tool for single-cell analysis, Angew. Chem. Int. Ed. 51 (2012) 12176–12192, https://doi.org/10.1002/anie.201200460.
[22] K. Samlali, F. Ahmadi, A.B.V. Quach, G. Soffer, S.C.C. Shih, One cell, one drop, one click: hybrid microfluidics for mammalian single cell isolation, Small 16 (2020) 1–13, https://doi.org/10.1002/smll.202002400.
[23] Y. Yeh, Z. Lin, S. Zheng, M. Terrones, A carbon nanotube integrated microfluidic device for blood plasma extraction, Sci. Rep. 8 (2018) 1–8, https://doi.org/10.1038/s41598-018-31810-x.
[24] M. Hu, J. Yan, Y. He, H. Lu, L. Weng, S. Song, C. Fan, L. Wang, Ultrasensitive, multiplexed detection of cancer biomarkers directly in serum by using a quantum dot-based microfluidic protein chip, ACS Nano 4 (2010) 488–494, https://doi.org/10.1021/nn901404h.
[25] N. Hao, Y. Nie, T. Shen, J.X.J. Zhang, Microfluidics enabled rational design of immunomagnetic nanomaterials and their shape, Lab Chip 18 (2018) 1997, https://doi.org/10.1039/c8lc00273h, 2002.
[26] N. Hao, Y. Nie, J.X.J. Zhang, Microfluidic flow synthesis of functional mesoporous silica nanofibers with tunable aspect ratios, ACS Sustain. Chem. Eng. 6 (2018) 1522–1526, https://doi.org/10.1021/acssuschemeng.7b03527.
[27] N. Alizadeh, A. Salimi, Polymer dots as a novel probe for fluorescence sensing of dopamine and imaging in single living cell using droplet microfluidic platform, Anal. Chim. Acta 1091 (2019) 40–49, https://doi.org/10.1016/j.aca.2019.08.036.
[28] S. Hu, S. Zeng, B. Zhang, C. Yang, P. Song, T.J. Hang Danny, G. Lin, Y. Wang, T. Anderson, P. Coquet, L. Liu, X. Zhang, K.T. Yong, Preparation of biofunctionalized quantum dots using microfluidic chips for bioimaging, Analyst 139 (2014) 4681–4690, https://doi.org/10.1039/c4an00773e.
[29] J.B. Wacker, I. Lignos, V.K. Parashar, M.A.M. Gijs, Controlled synthesis of fluorescent silica nanoparticles inside microfluidic droplets, Lab Chip 12 (2012) 3111–3116, https://doi.org/10.1039/c2lc40300e.
[30] W. Zhang, X. Zhao, Y. Yuan, F. Miao, W. Li, X. Huang, X. Chen, T. Jiang, D. A. Weitz, Y. Song, Microfluidic synthesis of multi-mode Au@CoFeB-Rg3 nanomedicines and their cytotoxicity and anti-tumor effects, Chem. Mater. 32 (2020) 5044–5056, https://doi.org/10.1021/acs.chemmater.0c00797.
[31] L. Zhang, Q. Feng, J. Wang, J. Sun, X. Shi, X. Jiang, Microfluidic synthesis of rigid nanovesicles for hydrophilic reagents delivery, Angew. Chem. Int. Ed. 54 (2015) 3952–3956, https://doi.org/10.1002/anie.201500096.
[32] R. Krzysztoń, B. Salem, D.J. Lee, G. Schwake, E. Wagner, J.O. Rädler, Microfluidic self-assembly of folate-targeted monomolecular siRNA-lipid nanoparticles, Nanoscale 9 (2017) 7442–7453, https://doi.org/10.1039/c7nr01593c.

[33] W. Wei, J. Sun, X.Y. Guo, X. Chen, R. Wang, C. Qiu, H.T. Zhang, W.H. Pang, J. C. Wang, Q. Zhang, Microfluidic-based holonomic constraints of siRNA in the kernel of lipid/polymer hybrid nanoassemblies for improving stable and safe in vivo delivery, ACS Appl. Mater. Interfaces 12 (2020) 14839–14854, https://doi.org/10.1021/acsami.9b22781.

[34] H. Kim, J. Sung, Y. Chang, A. Alfeche, C. Leal, Microfluidics synthesis of gene silencing cubosomes, ACS Nano 12 (2018) 9196–9205, https://doi.org/10.1021/acsnano.8b03770.

[35] S. Shen, T. Gu, D. Mao, X. Xiao, P. Yuan, M. Yu, L. Xia, Q. Ji, L. Meng, W. Song, C. Yu, G. Lu, Synthesis of nonspherical mesoporous silica ellipsoids with tunable aspect ratios for magnetic assisted assembly and gene delivery, Chem. Mater. 24 (2012) 230–235.

[36] Y. Morikawa, T. Tagami, A. Hoshikawa, T. Ozeki, The use of an efficient microfluidic mixing system for generating stabilized polymeric nanoparticles for controlled drug release, Biol. Pharm. Bull. 41 (2018) 899–907.

[37] Z. Zhang, X. Ma, M. Jia, B. Li, J. Rong, X. Yang, Deposition of CdTe quantum dots on microfluidic paper chips for rapid fluorescence detection of pesticide 2,4-D, Analyst 144 (2019) 1282–1291, https://doi.org/10.1039/c8an02051e.

[38] Y. Kim, F. Fay, D.P. Cormode, B.L. Sanchez-Gaytan, J. Tang, E.J. Hennessy, M. Ma, K. Moore, O.C. Farokhzad, E.A. Fisher, W.J.M. Mulder, R. Langer, Z. A. Fayad, Single step reconstitution of multifunctional high-density lipoprotein-derived nanomaterials using microfluidics, ACS Nano 7 (2013) 9975–9983, https://doi.org/10.1021/nn4039063.

[39] O. Tammaro, A. Costagliola, R. Eugenia, P. Antonio, E. Tori, A microfluidic platform to design multimodal PEG - crosslinked hyaluronic acid nanoparticles (PEG-cHANPs) for diagnostic applications, Sci. Rep. 10 (2020) 1–11.

[40] M. Seo, I. Gorelikov, R. Williams, N. Matsuura, Microfluidic assembly of monodisperse, nanoparticle-incorporated perfluorocarbon microbubbles for medical imaging and therapy, Langmuir 26 (2010) 13855–13860, https://doi.org/10.1021/la102272d.

[41] I.W. Park, M. Yoon, Y.M. Kim, Y. Kim, H. Yoon, H.J. Song, V. Volkov, A. Avilov, Y. J. Park, Magnetic properties and microstructure of cobalt nanoparticles in a polymer film, Solid State Commun. 126 (2003) 385–389, https://doi.org/10.1016/S0038-1098(03)00189-3.

[42] J. Shi, S. Gider, K. Babcock, D.D. Awschalom, Magnetic clusters in molecular beams, metals, and semiconductors, Science 80 (271) (1996) 937–941, https://doi.org/10.1126/science.271.5251.937.

[43] P.G. Jamkhande, N.W. Ghule, A.H. Bamer, M.G. Kalaskar, Metal nanoparticles synthesis: an overview on methods of preparation, advantages and disadvantages, and applications, J. Drug Deliv. Sci. Technol. 53 (2019), https://doi.org/10.1016/j.jddst.2019.101174.

[44] B. Das, S. Subramaniam, M.R. Melloch, Effects of electron-beam-induced damage on leakage currents in back-gated GaAs/AlGaAs devices, Semicond. Sci. Technol. 8 (1993) 1347–1351, https://doi.org/10.1088/0268-1242/8/7/025.

[45] P. Piszczek, A. Radtke, Silver nanoparticles fabricated using chemical vapor deposition and atomic layer deposition techniques: properties, applications and Perspectives: review, in: Noble Precious Met. - Prop. Nanoscale Eff, Appl., 2018, pp. 187–213, https://doi.org/10.5772/intechopen.71571.

[46] J. Lai, W. Niu, R. Luque, G. Xu, Solvothermal synthesis of metal nanocrystals and their applications, Nano Today 10 (2015) 240–267, https://doi.org/10.1016/j.nantod.2015.03.001.

[47] J. Li, Q. Wu, J. Wu, Synthesis of nanoparticles via solvothermal and hydrothermal methods, in: Handb. Nanoparticles, Springer Switzerland, 2015, pp. 1–1426, https://doi.org/10.1007/978-3-319-15338-4.

[48] P. Puja, P. Kumar, A perspective on biogenic synthesis of platinum nanoparticles and their biomedical applications, Spectrochim, Acta PartA Mol. Biomol. Spectrosc. 211 (2019) 94–99.

[49] J. Ali, N. Ali, L. Wang, H. Waseem, G. Pan, Revisiting the mechanistic pathways for bacterial mediated synthesis of noble metal nanoparticles, J. Microbiol. Methods 159 (2019) 18–25, https://doi.org/10.1016/j.mimet.2019.02.010.

[50] G.M. Chow, N.I. Noskova. Nanostructured Materials, Springer-Science+Business Media, B.V., 2001.

[51] X. Huang, N. Zheng, One-pot , high-yield synthesis of 5-fold twinned Pd nanowires and nanorods, J. Am. Chem. Soc. 131 (2009) 4602–4603, https://doi.org/10.1021/ja9009343.

[52] G. Fu, K. Wu, X. Jiang, L. Tao, Y. Chen, J. Lin, Y. Zhou, S. Wei, Y. Tang, T. Lu, X. Xia, Polyallylamine-directed green synthesis of platinum nanocubes. Shape and electronic effect codependent enhanced electrocatalytic activity, Phys. Chem. Chem. Phys. 15 (2013) 3793–3802, https://doi.org/10.1039/c3cp44191a.

[53] L. Habte, N. Shiferaw, D. Mulatu, T. Thenepalli, Synthesis of nano-calcium oxide from waste eggshell by sol-gel method, Sustainability 11 (2019) 1–10.

[54] B.K. Park, S. Jeong, D. Kim, J. Moon, S. Lim, J.S. Kim, Synthesis and size control of monodisperse copper nanoparticles by polyol method, J. Colloid Interface Sci. 311 (2007) 417–424, https://doi.org/10.1016/j.jcis.2007.03.039.

[55] H. Nagao, M. Ichiji, I. Hirasawa, Synthesis of platinum nanoparticles by reductive crystallization using polyethyleneimine, Chem. Eng. Technol. 40 (2017) 1242–1246, https://doi.org/10.1002/ceat.201600656.

[56] S. Chopra, N. Bertrand, J.M. Lim, A. Wang, O.C. Farokhzad, R. Karnik, Design of insulin-loaded nanoparticles enabled by multistep control of nanoprecipitation and zinc chelation, ACS Appl. Mater. Interfaces 9 (2017) 11440–11450, https://doi.org/10.1021/acsami.6b16854.

[57] L.-L. Li, X. Li, H. Wang, Microfluidic synthesis of nanomaterials for biomedical applications, Small Methods 1 (2017) 1700140, https://doi.org/10.1002/smtd.201700140.

[58] X. Zhao, F. Bian, L. Sun, L. Cai, L. Li, Y. Zhao, Microfluidic generation of nanomaterials for biomedical applications, Small 16 (2020) 1–19, https://doi.org/10.1002/smll.201901943.

[59] J. Ma, S.M.-Y. Lee, C. Yi, C.-W. Li, Controllable synthesis of functional nanoparticles by microfluidic platform for biomedical applications - a review, Lab Chip 17 (2017) 209–226, https://doi.org/10.1039/C6LC01049K.

[60] Y. Song, D. Cheng, L. Zhao. Microfluidics: Fundamentals, Devices, and Applications, Wiley-VCH, Germany, 2018.

[61] Microfluidics and Bio-MEMS: Devices and Applications, in: Tuhin Subhra Santra (Ed.), Jenny Stanford Publishing, 2021, ISBN 9789814800853.

[62] S. Watanabe, T. Hiratsuka, Y. Asahi, A. Tanaka, K. Mae, M.T. Miyahara, Flow synthesis of plasmonic gold nanoshells via a microreactor, part. Part, Syst. Charact 1–9 (2014), https://doi.org/10.1002/ppsc.201400126.

[63] X. Luo, P. Su, W. Zhang, C.L. Raston, Microfluidic devices in fabricating nano or micromaterials for biomedical applications, Adv. Mater. Technol. 4 (2019) 1900488, https://doi.org/10.1002/admt.201900488.

[64] N. Hao, Y. Nie, J.X.J. Zhang, Microfluidic synthesis of functional inorganic micro-/nanoparticles and applications in biomedical engineering, Int. Mater. Rev. 63 (2018) 461–487, https://doi.org/10.1080/09506608.2018.1434452.

[65] K.S. Elvira, X.C. I Solvas, R.C.R. Wootton, A.J. Demello, The past, present and potential for microfluidic reactor technology in chemical synthesis, Nat. Chem. 5 (2013) 905–915, https://doi.org/10.1038/nchem.1753.

[66] C.D. Ahrberg, J.W. Choi, B.G. Chung, Automated capillary dropelt reactor for the synthesis of iron oxide gold core-shell nanoparticles, in: 23rd Int. Conf. Miniaturized Syst. Chem. Life Sci. MicroTAS 2019, 2019, pp. 542–543.

[67] B. Pinho, L. Torrente-murciano, Continuous manufacturing of silver nanoparticles between 5 and 80 nm with rapid online optical size and shape evaluation, React. Chem. Eng. 5 (2020) 342–355, https://doi.org/10.1039/c9re00452a.

[68] N. Hao, Y. Nie, J.X.J. Zhang, Microfluidics for silica biomaterials synthesis: opportunities and challenges, Biomater. Sci. 7 (2019) 2218–2240, https://doi.org/10.1039/c9bm00238c.

[69] J. Wang, Y. Song, Microfluidic synthesis of nanohybrids, Small 13 (2017) 1–19, https://doi.org/10.1002/smll.201604084.

[70] K.S. Krishna, Y. Li, S. Li, C.S.S.R. Kumar, Lab-on-a-chip synthesis of inorganic nanomaterials and quantum dots for biomedical applications, Adv. Drug Deliv. Rev. 65 (2013) 1470–1495, https://doi.org/10.1016/j.addr.2013.05.006.

[71] J.W. Choi, Y.J. Kim, J.M. Lee, J.H. Choi, J.W. Choi, B.G. Chung, Droplet-based synthesis of homogeneous gold nanoparticles for enhancing HRP-based ELISA signals, Biochip J (2020), https://doi.org/10.1007/s13206-020-4307-z.

[72] K.I. Min, D.J. Im, H.J. Lee, D.P. Kim, Three-dimensional flash flow microreactor for scale-up production of monodisperse PEG-PLGA nanoparticles, Lab Chip 14 (2014) 3987–3992, https://doi.org/10.1039/c4lc00700j.

[73] C.L. Grigsby, Y. Ho, C. Lin, J.F.J. Engbersen, K.W. Leong, Microfluidic preparation of polymer-nucleic acid nanocomplexes improves nonviral gene transfer, Sci. Rep. 3 (2013) 1–7, https://doi.org/10.1038/srep03155.

[74] Z. Han, X. Jiang, Microfluidic synthesis of functional nanoparticles, Nanotechnol. Microfluid. (2020) 319–345, https://doi.org/10.1002/9783527818341.ch10.

[75] Y. He, K.J. Kim, C.H. Chang, Segmented microfluidic flow reactors for nanomaterial synthesis, Nanomaterials 10 (2020) 1–21, https://doi.org/10.3390/nano10071421.

[76] M. Lu, A. Ozcelik, C.L. Grigsby, Y. Zhao, F. Guo, K.W. Leong, T.J. Huang, Microfluidic hydrodynamic focusing for synthesis of nanomaterials, Nano Today 11 (2016) 778–792, https://doi.org/10.1016/j.nantod.2016.10.006.

[77] R.R. Hood, D.L. Devoe, J. Atencia, W.N. Vreeland, D.M. Omiatek, A facile route to the synthesis of monodisperse nanoscale liposomes using 3D microfluidic hydrodynamic focusing in a concentric capillary array, Lab Chip 14 (2014) 2403–2409, https://doi.org/10.1039/c4lc00334a.

[78] A. Yaghmur, A. Ghazal, R. Ghazal, M. Dimaki, W.E. Svendsen, A hydrodynamic flow focusing microfluidic device for the continuous production of hexosomes based on docosahexaenoic acid monoglyceride, Phys. Chem. Chem. Phys. 21 (2019) 13005–13013, https://doi.org/10.1039/c9cp02393c.

[79] M.V. Bandulasena, G.T. Vladisavljević, B. Benyahia, Droplet-based microfluidic method for robust preparation of gold nanoparticles in axisymmetric flow focusing device, Chem. Eng. Sci. 195 (2019) 657–664, https://doi.org/10.1016/j.ces.2018.10.010.

[80] M. Lu, S. Yang, Y. Ho, C.L. Grigsby, K.W. Leong, L.U.E.T. Al, Shape-controlled synthesis of hybrid nanomaterials via three-dimensional hydrodynamic focusing, ACS Nano 8 (2014) 10026–10034.

[81] A.M. Gañán-calvo, J.M. Montanero, L. Martín-banderas, M. Flores-mosquera, Building functional materials for health care and pharmacy from microfluidic principles and Flow Focusing, Adv. Drug Deliv. Rev. 65 (2013) 1447–1469.

[82] O. Kašpar, A.H. Koyuncu, A. Hubatová-Vacková, M. Balouch, V. Tokárová, Influence of channel height on mixing efficiency and synthesis of iron oxide nanoparticles using droplet-based microfluidics, RSC Adv. 10 (2020) 15179–15189, https://doi.org/10.1039/d0ra02470h.

[83] J. Bemetz, A. Wegemann, K. Saatchi, A. Haase, U.O. Häfeli, R. Niessner, B. Gleich, M. Seidel, Microfluidic-based synthesis of magnetic nanoparticles coupled with miniaturized NMR for online relaxation studies, Anal. Chem. 90 (2018) 9975–9982, https://doi.org/10.1021/acs.analchem.8b02374.

[84] P.M. Valencia, P.A. Basto, L. Zhang, M. Rhee, R. Langer, O.C. Farokhzad, R. Karnik, Single-step assembly of homogenous lipid-polymeric and lipid-quantum dot nanoparticles enabled by microfluidic rapid mixing, ACS Nano 4 (2010) 1671–1679, https://doi.org/10.1021/nn901433u.

[85] G. Schabas, H. Yusuf, M.G. Moffitt, D. Sinton, Controlled self-assembly of quantum dots and block copolymers in a microfluidic device, Langmuir 24 (2008) 637–643, https://doi.org/10.1021/la703297q.

[86] K. Liu, Z. Zhu, X. Wang, D. Gonçalves, B. Zhang, A. Hierlemann, P. Hunziker, Microfluidics-based single-step preparation of injection-ready polymeric nanosystems for medical imaging and drug delivery, Nanoscale 7 (2015) 16983–16993, https://doi.org/10.1039/c5nr03543k.
[87] B. Herranz-Blanco, E. Ginestar, H. Zhang, J. Hirvonen, H.A. Santos, Microfluidics platform for glass capillaries and its application in droplet and nanoparticle fabrication, Int. J. Pharm. 516 (2017) 100–105, https://doi.org/10.1016/j.ijpharm.2016.11.024.
[88] A. Abou-hassan, R. Bazzi, V. Cabuil, Multistep continuous-flow microsynthesis of magnetic and fluorescent γ-Fe2O3@SiO2 core/shell nanoparticles, Angew. Chem. Int. Ed. 48 (2009) 7180–7183.
[89] G. Bovone, E.A. Guzzi, M.W. Tibbitt, Flow-based reactor design for the continuous production of polymeric nanoparticles, AIChE J. 65 (2019) 1–13, https://doi.org/10.1002/aic.16840.
[90] J. Xu, S. Zhang, A. Machado, S. Lecommandoux, O. Sandre, Controllable microfluidic production of drug-loaded PLGA nanoparticles using partially water-miscible mixed solvent microdroplets as a precursor, Sci. Rep. 7 (2017) 1–12, https://doi.org/10.1038/s41598-017-05184-5.
[91] S. Ding, M.F. Attia, J. Wallyn, C. Taddei, C.A. Serra, N. Anton, M. Kassem, M. Schmutz, M. Er-Rafik, N. Messaddeq, A. Collard, W. Yu, M. Giordano, T. F. Vandamme, Microfluidic-assisted production of size-controlled superparamagnetic iron oxide nanoparticles-loaded poly(methyl methacrylate) nanohybrids, Langmuir 34 (2018) 1981, https://doi.org/10.1021/acs.langmuir.7b01928, 1991.
[92] Microfluidics Market - Global Forecast to 2025 | MarketsandMarkets, (n.d.). https://www.marketsandmarkets.com/Market-Reports/microfluidics-market-1305.html (accessed December 24, 2020).
[93] Microfluidics Market | Growth, Trends, and Forecast, 2020 - 2025 (n.d.), https://www.mordorintelligence.com/industry-reports/microfluidics-market. (Accessed 24 December 2020).
[94] L. Liu, N. Xiang, Z. Ni, Droplet-based microreactor for the production of micro/nano-materials, Electrophoresis 41 (2020) 833–851, https://doi.org/10.1002/elps.201900380.
[95] J. Ma, Y. Wang, J. Liu, Biomaterials meet microfluidics : from synthesis technologies to biological applications, Micromachines 8 (2017), https://doi.org/10.3390/mi8080255.
[96] X.C.I. Solvas, A. Demello, Droplet microfluidics: recent developments and future applications, Chem. Commun. 47 (2011) 1936–1942, https://doi.org/10.1039/c0cc02474k.
[97] P. Shrimal, G. Jadeja, S. Patel, A review on novel methodologies for drug nanoparticle preparation: microfluidic approach, Chem. Eng. Res. Des. 153 (2020) 728–756, https://doi.org/10.1016/j.cherd.2019.11.031.
[98] Q. Ma, J. Cao, Y. Gao, S. Han, Y. Liang, Microfluidic-mediated nano-drug delivery systems: from fundamentals to fabrication for advanced therapeutic applications, Nanoscale (2020), https://doi.org/10.1039/d0nr02397c.
[99] N. Hao, Y. Nie, Z. Xu, J.X.J. Zhang, Ultrafast microfluidic synthesis of hierarchical triangular silver core-silica shell nanoplatelet toward enhanced cellular internalization, J. Colloid Interface Sci. 542 (2019) 370–378.
[100] R. Manno, V. Sebastian, R. Mallada, 110th anniversary : nucleation of Ag nanoparticles in helical microfluidic reactor . Comparison between microwave and conventional heating, Ind. Eng. Chem. Res. 58 (2019) 12702–12711, https://doi.org/10.1021/acs.iecr.9b01460.
[101] L. Pan, J. Tu, H. Ma, Y. Yang, Z. Tian, Controllable synthesis of nanocrystals in droplet reactors, Lab Chip (2017), https://doi.org/10.1039/c7lc00800g.
[102] S.A. Khan, A. Gu, M.A. Schmidt, K.F. Jensen, Microfluidic synthesis of colloidal silica, Langmuir 20 (2004) 8604–8611.
[103] O. Sartipzadeh, S. Morteza, A. Seyfoori, M. Rahmanian, Controllable size and form of droplets in microfluidic-assisted devices : effects of channel geometry and fluid velocity on droplet size, Mater. Sci. Eng. C 109 (2020).
[104] M.V. Bandulasena, G.T. Vladisavljević, B. Benyahia, Droplet-based microfluidic method for robust preparation of gold nanoparticles in axisymmetric flow focusing device, Chem. Eng. Sci. 195 (2019) 657–664, https://doi.org/10.1016/j.ces.2018.10.010.
[105] S. Abalde-cela, P. Taladriz-blanco, M.G. De Oliveira, C. Abell, Droplet microfluidics for the highly controlled synthesis of branched gold nanoparticles, Sci. Rep. (2018) 1–6, https://doi.org/10.1038/s41598-018-20754-x.
[106] S. Duraiswamy, S.A. Khan, Droplet-based microfluidic synthesis of anisotropic metal nanocrystals, Small 5 (2009) 2828–2834, https://doi.org/10.1002/smll.200901453.
[107] C.J. Johnson, E. Dujardin, S.A. Davis, C.J. Murphy, S. Mann, Growth and form of gold nanorods prepared by seed-mediated, surfactant-directed synthesis, J. Mater. Chem. 12 (2002) 1765–1770, https://doi.org/10.1039/b200953f.
[108] G. De Crozals, R. Bonnet, C. Farre, C. Chaix, Nanoparticles with multiple properties for biomedical applications : a strategic guide, Nano Today 11 (2016) 435–463.
[109] F. Parveen, B. Sannakki, M.V. Mandke, H.M. Pathan, Copper nanoparticles: synthesis methods and its light harvesting performance, Sol. Energy Mater. Sol. Cells 144 (2016) 371–382, https://doi.org/10.1016/j.solmat.2015.08.033.
[110] C.L. Nehl, J.H. Hafner, Shape-dependent plasmon resonances of gold nanoparticles, J. Mater. Chem. 18 (2008) 2415–2419, https://doi.org/10.1039/b714950f.
[111] W.Q. Lim, Z. Gao, Plasmonic nanoparticles in biomedicine, Nano Today 11 (2016) 168–188.
[112] X. Xu, X. Liu, L. Tan, Z. Cui, X. Yang, S. Zhu, Z. Li, X. Yuan, Y. Zheng, K.W. K. Yeung, P.K. Chu, S. Wu, Controlled-temperature photothermal and oxidative bacteria killing and acceleration of wound healing by polydopamine-assisted Au-hydroxyapatite nanorods, Acta Biomater. 77 (2018) 352–364, https://doi.org/10.1016/j.actbio.2018.07.030.
[113] J. He, Y. Qiao, H. Zhang, J. Zhao, W. Li, T. Xie, D. Zhong, Q. Wei, S. Hua, Y. Yu, K. Yao, H.A. Santos, M. Zhou, Gold–silver Nanoshells Promote Wound Healing from Drug-Resistant Bacteria Infection and Enable Monitoring via Surface-Enhanced Raman Scattering Imaging, Biomaterials, 2020, p. 234, https://doi.org/10.1016/j.biomaterials.2020.119763.
[114] N.S. Abadeer, C.J. Murphy, Recent progress in cancer thermal therapy using gold nanoparticles, J. Phys. Chem. C 120 (2016) 4691–4716, https://doi.org/10.1021/acs.jpcc.5b11232.
[115] A.M. Boies, P. Lei, S. Calder, W.G. Shin, S.L. Girshick, Hot-wire synthesis of gold nanoparticles, Aerosol Sci. Technol. 45 (2011) 654–663, https://doi.org/10.1080/02786826.2010.551145.
[116] H. Huang, H. du Toit, M.O. Besenhard, S. Ben-Jaber, P. Dobson, I. Parkin, A. Gavriilidis, Continuous flow synthesis of ultrasmall gold nanoparticles in a microreactor using trisodium citrate and their SERS performance, Chem. Eng. Sci. 189 (2018) 422–430, https://doi.org/10.1016/j.ces.2018.06.050.
[117] T. Araújo, R. Candeias, N. Nunes, H. Gamboa, Evaluation of motor neuron excitability by CMAP scanning with electric modulated current, Neurosci. J. (2015) 1–5, https://doi.org/10.1155/2015/360648, 2015.
[118] P. Shinde, L. Mohan, A. Kumar, K. Dey, A. Maddi, A.N. Patananan, F.G. Tseng, H. Y. Chang, M. Nagai, T.S. Santra, Current trends of microfluidic single-cell technologies, Int. J. Mol. Sci. 19 (2018), https://doi.org/10.3390/ijms19103143.
[119] J. Watt, B.G. Hance, R.S. Anderson, D.L. Huber, Effect of seed age on gold nanorod formation: a microfluidic, real-time investigation, Chem. Mater. 27 (2015) 6442–6449, https://doi.org/10.1021/acs.chemmater.5b02675.
[120] E.C. Dreaden, A.M. Alkilany, X. Huang, C.J. Murphy, M.A. El-Sayed, The golden age: gold nanoparticles for biomedicine, Chem. Soc. Rev. 41 (2012) 2740–2779, https://doi.org/10.1039/c1cs15237h.
[121] T.S. Santra, F.-G. Tseng, Pulse laser activated photoporation for high efficient intracellular delivery using nano-corrugated mushroom shape gold nanoparticles, Int. Conf. Miniaturized Syst. Chem. Life Sci. (2016) 1097–1098.
[122] X. Xie, J. Liao, X. Shao, Q. Li, Y. Lin, The effect of shape on cellular uptake of gold nanoparticles in the forms of stars, rods, and triangles, Sci. Rep. 7 (2017) 1–9, https://doi.org/10.1038/s41598-017-04229-z.
[123] G. Liu, X. Ma, X. Sun, Y. Jia, T. Wang, Controllable synthesis of silver nanoparticles using three-phase flow pulsating mixing microfluidic chip, Ann. Mater. Sci. Eng. (2018), https://doi.org/10.1155/2018/3758161.
[124] W. Jin, G. Liang, Y. Zhong, Y. Yuan, Z. Jian, Z. Wu, W. Zhang, The influence of CTAB-capped seeds and their aging time on the morphologies of silver nanoparticles, Nanoscale Res. Lett. 14 (2019), https://doi.org/10.1186/s11671-019-2898-x.
[125] N.T.K. Thanh, N. Maclean, S. Mahiddine, Mechanisms of nucleation and growth of nanoparticles in solution, Chem. Rev. 114 (2014) 7610–7630, https://doi.org/10.1021/cr400544s.
[126] X. Hou, Y.S. Zhang, G.T. De Santiago, M.M. Alvarez, J. Ribas, S.J. Jonas, P. S. Weiss, A.M. Andrews, J. Aizenberg, A. Khademhosseini, Interplay between materials and microfluidics, Nat. Rev. Mater. 2 (2017) 1–15, https://doi.org/10.1038/natrevmats.2017.16.
[127] L. Panariello, S. Damilos, H. Toit, G. Wu, A.N.P. Radhakrishnan, I.P. Parkin, A. Gavriilidis, Highly reproducible, high-yield flow synthesis of gold nanoparticles based on a rational reactor design exploiting the reduction of passivated Au(III), React. Chem. Eng. 5 (2020) 663–676, https://doi.org/10.1039/c9re00469f.
[128] R. Manno, P. Ranjan, V. Sebastian, R. Mallada, S. Irusta, U.K. Sharma, E.V. Van Der Eycken, Continuous microwave-assisted synthesis of silver nanoclusters confined in mesoporous SBA-15 : application in alkyne cyclizations, Chem. Mater. 32 (2020) 2874–2883.
[129] R. Baber, L. Mazzei, N. Thi, K. Thanh, A. Gavriilidis, An engineering approach to synthesis of gold and silver nanoparticles by controlling hydrodynamics and mixing based on a coaxial flow reactor, Nanoscale 9 (2017) 14149–14161, https://doi.org/10.1039/c7nr04962e.
[130] S. Sachdev, R. Maugi, J. Woolley, C. Kirk, Z. Zhou, S.D.R. Christie, M. Platt, Synthesis of gold nanoparticles using the interface of an emulsion droplet, Lab Chip 33 (2017) 5464–5472, https://doi.org/10.1021/acs.langmuir.7b00564.
[131] X.Z. Lin, A.D. Terepka, H. Yang, Synthesis of silver nanoparticles in a continuous flow tubular microreactor, Nano Lett. 4 (2004) 2227–2232, https://doi.org/10.1021/nl0485859.
[132] K. Illath, A.K. Narasimahan, M. Nagai, S. Wankhar, T.S. Santra, Microfluidic based metallic nanoparticle synthesis and applications, in: Bio-MEMS Bio-NEMS Devices Appl, Jenny Stanford Publishers, 2020. https://www.routledge.com/Microfluidics-and-BioMEMS-Devices-and-Applications/Santra/p/book/9789814800853.
[133] L. Xu, J. Peng, M. Yan, D. Zhang, A.Q. Shen, Droplet synthesis of silver nanoparticles by a microfluidic device, Chem. Eng. Process. Process Intensif. 102 (2016) 186–193, https://doi.org/10.1016/j.cep.2016.01.017.
[134] D. Shalom, R.C.R. Wootton, R.F. Winkle, B.F. Cottam, R. Vilar, A.J. deMello, C. P. Wilde, Synthesis of thiol functionalized gold nanoparticles using a continuous flow microfluidic reactor, Mater. Lett. 61 (2007) 1146–1150, https://doi.org/10.1016/j.matlet.2006.06.072.
[135] J. Wagner, J.M. Köhler, Continuous synthesis of gold nanoparticles in a microreactor, Nano Lett. 5 (2005) 685–691, https://doi.org/10.1021/nl050097t.
[136] C.H. Kwak, S.-M. Kang, E. Jung, Y. Haldorai, Y.-K. Han, W.-S. Kim, T. Yu, Y. S. Huh, Customized microfluidic reactor based on droplet formation for the synthesis of monodispersed silver nanoparticles, J. Ind. Eng. Chem. 63 (2018) 405–410.

[137] A. Pekkari, Z. Say, A. Susarrey-arce, C. Langhammer, H. Ha, V. Sebastian, K. Moth-poulsen, Continuous microfluidic synthesis of Pd nanocubes and PdPt core − shell nanoparticles and their catalysis of NO2 reduction, ACS Appl. Mater. Interfaces 11 (2019) 36196–36204, https://doi.org/10.1021/acsami.9b09701.
[138] C.H. Weng, C.C. Huang, C.S. Yeh, G. Bin Lee, Synthesis of hexagonal gold nanoparticles using microfluidic reaction systems, J. Micromech. Microeng. 18 (2007) 462–466, https://doi.org/10.1109/NANO.2007.4601232.
[139] V. Sebastian, C.D. Smith, K.F. Jensen, Shape-controlled continuous synthesis of metal nanostructures, Nanoscale (2016), https://doi.org/10.1039/c5nr08531d.
[140] T. Gu, S.A. Khan, C. Zheng, F. He, Y. Zhang, T.A. Hatton, Electrically controlled mass transport into microfluidic droplets from nanodroplet carriers with application in controlled nanoparticle flow, Lab Chip 18 (2018) 1330–1340, https://doi.org/10.1039/c8lc00114f.
[141] J. Zhao, C. Wu, L. Zhai, X. Shi, X. Li, G. Weng, J. Zhu, J. Li, J.-W. Zhao, A SERS-based immunoassay for the detection of a-fetoprotein using AuNS@Ag@SiO2 core–shell nanostars, J. Mater. Chem. C. 7 (2019) 8432–8441, https://doi.org/10.1039/c9tc01890e.
[142] V. López, M.R. Villegas, V. Rodríguez, G. Villaverde, D. Lozano, A. Baeza, M. Vallet-Regí, Janus mesoporous silica nanoparticles for dual targeting of tumor cells and mitochondria, ACS Appl. Mater. Interfaces 9 (2017) 26697–26706, https://doi.org/10.1021/acsami.7b06906.
[143] P. He, G. Greenway, S.J. Haswell, The on-line synthesis of enzyme functionalized silica nanoparticles in a microfluidic reactor using polyethylenimine polymer and R5 peptide, Nanotechnology 19 (2008) 315603, https://doi.org/10.1088/0957-4484/19/31/315603.
[144] L. Gutierrez, L. Gomez, S. Irusta, M. Arruebo, J. Santamaria, Comparative study of the synthesis of silica nanoparticles in micromixer-microreactor and batch reactor systems, Chem. Eng. J. 171 (2011) 674–683.
[145] T.N. Ng, X.Q. Chen, K.L. Yeung, Direct manipulation of particle size and morphology of ordered mesoporous silica by flow synthesis, RSC Adv. 5 (2015) 13331–13340, https://doi.org/10.1039/c4ra16679e.
[146] C.K. Chung, T.R. Shih, C.K. Chang, C.W. Lai, B.H. Wu, Design and experiments of a short-mixing-length baffled microreactor and its application to microfluidic synthesis of nanoparticles, Chem. Eng. J. 168 (2011) 790–798.
[147] P. He, G. Greenway, S.J. Haswell, Microfluidic synthesis of silica nanoparticles using polyethylenimine polymers, Chem. Eng. J. 167 (2011) 694–699, https://doi.org/10.1016/j.cej.2010.08.079.
[148] Y. He, K. Kim, C. Chang, Continuous, size and shape-control synthesis of hollow silica nanoparticles enabled by a microreactor-assisted rapid mixing process, Nanotechnology 28 (2017).
[149] N. Hao, Y. Nie, A. Tadimety, A.B. Closson, X.J. John, Microfluidics-mediated self-template synthesis of anisotropic hollow ellipsoidal mesoporous silica nanomaterials, Mater. Res. Lett. 5 (2017) 584–590, https://doi.org/10.1080/21663831.2017.1376720.
[150] I. Lignos, H. Ow, D.A. Mccollum, H. Zhang, J. Imbrogno, Y. Shen, S. Chang, W. Wang, K.F. Jensen, Continuous multistage synthesis and functionalization of sub-100 nm silica nanoparticles in 3D-printed continuous stirred-tank reactor cascades, ACS Appl. Mater. Interfaces 12 (2020) 6699–6706.
[151] N. Hao, Y. Nie, A.B. Closson, J.X.J. Zhang, Microfluidic synthesis and on-chip enrichment application of two-dimensional hollow sandwich-like mesoporous silica nanosheet with water ripple-like surface, J. Colloid Interface Sci. 539 (2019) 87–94.
[152] J.M. Chem, L. Gomez, M. Arruebo, V. Sebastian, J. Santamaria, Facile synthesis of SiO 2 – Au nanoshells in a three-stage microfluidic system, J. Mater. Chem. 22 (2012) 21420–21425, https://doi.org/10.1039/c2jm34206e.
[153] P. Masse, S. Mornet, E. Duguet, M. Tréguer-Delapierre, Synthesis of size-monodisperse spherical Ag@SiO2 nanoparticles and 3-D assembly assisted by microfluidics, Langmuir 29 (2013) 1790–1795.
[154] L. Zhang, Q. Feng, J. Wang, S. Zhang, B. Ding, Y. Wei, M. Dong, J.Y. Ryu, T. Y. Yoon, X. Shi, J. Sun, X. Jiang, Microfluidic synthesis of hybrid nanoparticles with controlled lipid layers: understanding flexibility-regulated cell-nanoparticle interaction, ACS Nano 9 (2015) 9912–9921, https://doi.org/10.1021/acsnano.5b05792.
[155] L. Zhang, A. Beatty, L. Lu, A. Abdalrahman, T.M. Makris, G. Wang, Q. Wang, Microfluidic-assisted polymer-protein assembly to fabricate homogeneous functional nanoparticles, Mater. Sci. Eng. C 111 (2020), https://doi.org/10.1016/j.msec.2020.110768.
[156] L. Zhang, Q. Chen, Y. Ma, J. Sun, Microfluidic methods for fabrication and engineering of nanoparticle drug delivery systems, ACS Appl. Bio Mater. 3 (2020) 107–120, https://doi.org/10.1021/acsabm.9b00853.
[157] D. Liu, S. Cito, Y. Zhang, C. Wang, T.M. Sikanen, H.A. Santos, A versatile and robust microfluidic platform toward high throughput synthesis of homogeneous nanoparticles with tunable properties, Adv. Mater. 27 (2015) 2298–2304, https://doi.org/10.1002/adma.201405408.
[158] P.M. Valencia, E.M. Pridgen, M. Rhee, R. Langer, O.C. Farokhzad, R. Karnik, Microfluidic platform for combinatorial synthesis and optimization of targeted nanoparticles for cancer therapy, ACS Nano 7 (2013) 10671–10680, https://doi.org/10.1021/nn403370e.
[159] C. Liu, W. Zhang, Y. Li, J. Chang, F. Tian, F. Zhao, Y. Ma, J. Sun, Microfluidic sonication to assemble exosome membrane-coated nanoparticles for immune evasion-mediated targeting, Nano Lett. 19 (2019) 7836–7844, https://doi.org/10.1021/acs.nanolett.9b02841.
[160] Q. Feng, J. Liu, X. Li, Q. Chen, J. Sun, X. Shi, B. Ding, H. Yu, Y. Li, X. Jiang, One-step microfluidic synthesis of nanocomplex with tunable rigidity and acid-switchable surface charge for overcoming drug resistance, Small 13 (1–9) (2017) 1603109, https://doi.org/10.1002/smll.201603109.
[161] C.D. Ahrberg, J. Wook Choi, B. Geun Chung, Automated droplet reactor for the synthesis of iron oxide/gold core-shell nanoparticles, Sci. Rep. 10 (2020) 1737, https://doi.org/10.1038/s41598-020-58580-9.
[162] T.H. Nguyen, A. Sedighi, U.J. Krull, C.L. Ren, Multifunctional droplet microfluidic platform for rapid immobilization of oligonucleotides on semiconductor quantum dots, ACS Sens. 5 (2020) 746–753, https://doi.org/10.1021/acssensors.9b02145.
[163] A. Ali, H. Zafar, M. Zia, I. ul Haq, A.R. Phull, J.S. Ali, A. Hussain, Synthesis, characterization, applications, and challenges of iron oxide nanoparticles, Nanotechnol. Sci. Appl. 9 (2016) 49–67.
[164] N. Hassan, V. Cabuil, A. Abou-hassan, Continuous multistep microfluidic assisted assembly of fluorescent, plasmonic, and magnetic nanostructures **, Angew. Chem. Int. Ed. 52 (2013) 1994–1997, https://doi.org/10.1002/anie.201208324.
[165] N. Hassan, M.L. Cordero, R. Sierpe, M. Almada, J. Juárez, M. Valdez, A. Riveros, E. Vargas, A. Abou-Hassan, J.M. Ruso, M.J. Kogan, Peptide functionalized magneto-plasmonic nanoparticles obtained by microfluidics for inhibition of β-amyloid aggregation, J. Mater. Chem. B. 6 (2018) 5091–5099, https://doi.org/10.1039/c8tb00206a.
[166] L. Rao, B. Cai, L.L. Bu, Q.Q. Liao, S.S. Guo, X.Z. Zhao, W.F. Dong, W. Liu, Microfluidic electroporation-facilitated synthesis of erythrocyte membrane-coated magnetic nanoparticles for enhanced imaging-guided cancer therapy, ACS Nano 11 (2017) 3496–3505, https://doi.org/10.1021/acsnano.7b00133.
[167] S. Kubendhiran, Z. Bao, K. Dave, R. Liu, Microfluidic synthesis of semiconducting colloidal quantum dots and their applications, ACS Appl. Nano Mater. 2 (2019) 1773–1790, https://doi.org/10.1021/acsanm.9b00456.
[168] J.B. Edel, R. Fortt, J.C. DeMello, A.J. Demello, Microfluidic routes to the controlled production of nanoparticles, Chem. Commun. (2002) 1136–1137.
[169] R. Cheng, K. Ma, H.-G. Ye, L. Ling, G. Wu, C.-F. Wang, S. Chen, Magnetothermal microfluidic-directed synthesis of quantum dots, J. Mater. Chem. C. 8 (2020) 6309–6626, https://doi.org/10.1039/d0tc00305k.
[170] Z. Huang, T. Zhou, Y. Yuan, S. Natalie Kłodzińska, T. Zheng, C. Sternberg, H. Mørck Nielsen, Y. Sun, F. Wan, Synthesis of carbon quantum dot-poly lactic-co-glycolic acid hybrid nanoparticles for chemo-photothermal therapy against bacterial biofilms, J. Colloid Interface Sci. 577 (2020) 66–74, https://doi.org/10.1016/j.jcis.2020.05.067.
[171] S. Tai, W. Zhang, J. Zhang, G. Luo, Y. Jia, Facile preparation of UiO-66 nanoparticles with tunable sizes in a continuous flow microreactor and its application in drug delivery, Microporous Mesoporous Mater. 220 (2016) 148–154.
[172] H.M. Jun, M.J. Oh, J.H. Lee, P.J. Yoo, Microfluidic synthesis of carbon nanotube-networked solid- shelled bubbles, Langmuir 36 (2020) 948–955, https://doi.org/10.1021/acs.langmuir.9b03268.
[173] S. Shikha, X. Zheng, Y. Zhang, Upconversion nanoparticles-encoded hydrogel microbeads-based multiplexed protein detection, Nano-Micro Lett. 10 (2018), https://doi.org/10.1007/s40820-017-0184-y.
[174] P. Stolzenburg, T. Lorenz, A. Dietzel, G. Garnweitner, Microfluidic synthesis of metal oxide nanoparticles via the nonaqueous method, Chem. Eng. Sci. 191 (2018) 500–510.
[175] P. Ranadive, A. Parulkar, N.A. Brunelli, Jet-mixing reactor for the production of monodisperse silver nanoparticles using a reduced amount of capping agent †, React. Chem. Eng. 4 (2019) 1779–1789, https://doi.org/10.1039/c9re00152b.
[176] E. Chow, B. Raguse, D. Gaspera, J. Hong, L.J. Hubble, R. Chai, J.S. Cooper, A. Sosa, S.J. Barrow, Flow-controlled synthesis of gold nanoparticles in a biphasic system with inline liquid – liquid separation †, React. Chem. Eng 45–48 (2019) https://doi.org/10.1039/c9re00403c.
[177] L. Uson, V. Sebastian, M. Arruebo, J. Santamaria, Continuous microfluidic synthesis and functionalization of gold nanorods, Chem. Eng. J. 285 (2016) 286–292, https://doi.org/10.1016/j.cej.2015.09.103.
[178] N. Hao, Y. Nie, Z. Xu, A.B. Closson, T. Usherwood, J.X.J. Zhang, Microfluidic continuous flow synthesis of functional hollow spherical silica with hierarchical sponge-like large porous shell, Chem. Eng. J. 366 (2019) 433–438.
[179] L. Uson, M. Arruebo, V. Sebastian, J. Santamaria, Single phase microreactor for the continuous, high-temperature synthesis of <4 nm superparamagnetic iron oxide nanoparticles, Chem. Eng. J. 340 (2018) 66–72, https://doi.org/10.1016/j.cej.2017.12.024.
[180] J. Nette, P.D. Howes, A.J. DeMello, Microfluidic synthesis of luminescent and plasmonic nanoparticles: fast, efficient, and data-rich, Adv. Mater. Technol. 5 (2020), https://doi.org/10.1002/admt.202000060.
[181] R.M. Maceiczyk, I.G. Lignos, A.J. Demello, Online detection and automation methods in microfluidic nanomaterial synthesis, Curr. Opin. Chem. Eng. 8 (2015) 29–35, https://doi.org/10.1016/j.coche.2015.01.007.
[182] M.J. Toth, T. Kim, Y.T. Kim, Robust manufacturing of lipid-polymer nanoparticles through feedback control of parallelized swirling microvortices, Lab Chip 17 (2017) 2805–2813, https://doi.org/10.1039/c7lc00668c.
[183] L. Litti, Y. Gao, P. V Gwozdz, L. Sharpnack, R.H. Blick, L.M. Liz-marza, M. Grzelczak, M. Trebbin, Time-resolved analysis of the structural dynamics of assembling gold nanoparticles, ACS Nano 13 (2019) 6596–6604, https://doi.org/10.1021/acsnano.9b00575.
[184] J. Watt, B.G. Hance, R.S. Anderson, D.L. Huber, Effect of seed age on gold nanorod formation: a microfluidic, real- time investigation, Chem. Mater. 27 (2015) 6442–6449, https://doi.org/10.1021/acs.chemmater.5b02675.
[185] A. Knauer, A. Eisenhardt, S. Krischok, J.M. Koehler, Nanometer precise adjustment of the silver shell thickness during automated Au-Ag core-shell nanoparticle synthesis in microfluid segment sequences, Nanoscale 6 (2014) 5230–5238, https://doi.org/10.1039/c3nr06438g.

[186] S. Krishnadasan, R.J.C. Brown, A.J. DeMello, J.C. DeMello, Intelligent routes to the controlled synthesis of nanoparticles, Lab Chip 7 (2007) 1434–1441, https://doi.org/10.1039/b711412e.
[187] I. Srivastava, M.S. Khan, K. Dighe, M. Alafeef, Z. Wang, T. Banerjee, T. Ghonge, L. M. Grove, R. Bashir, D. Pan, On-chip electrical monitoring of real-time "soft" and "hard" protein corona formation on carbon nanoparticles, Small Methods 4 (2020), https://doi.org/10.1002/smtd.202000099.
[188] M. Sedighi, S. Sieber, F. Rahimi, M.A. Shahbazi, A.H. Rezayan, J. Huwyler, D. Witzigmann, Rapid optimization of liposome characteristics using a combined microfluidics and design-of-experiment approach, Drug Deliv. Transl. Res. 9 (2018) 404–413, https://doi.org/10.1007/s13346-018-0587-4.
[189] L. Bezinge, R.M. Maceiczyk, I. Lignos, M. V Kovalenko, J. Andrew, Pick a Color MARIA: Adaptive sampling enables the rapid identification of complex perovskite nanocrystal compositions with defined emission characteristics, ACS Appl. Mater. Interfaces 10 (2018) 18869–18878, https://doi.org/10.1021/acsami.8b03381.
[190] C.B. Kerr, R.W. Epps, M. Abolhasani, A low-cost, non-invasive phase velocity and length meter and controller for multiphase lab-in- a-tube devices†, Lab Chip 19 (2019) 2107–2113, https://doi.org/10.1039/c9lc00296k.
[191] M. Berenguel-Alonso, I. Ortiz-Gómez, B. Fernández, P. Couceiro, J. Alonso-Chamarro, L.F. Capitán-Vallvey, A. Salinas-Castillo, M. Puyol, An LTCC monolithic microreactor for the synthesis of carbon dots with photoluminescence imaging of the reaction progress, Sensor. Actuator. B Chem. 296 (2019) 126613, https://doi.org/10.1016/j.snb.2019.05.090.
[192] R.M. Maceiczyk, L. Bezinge, A.J. Demello, Kinetics of nanocrystal synthesis in a microfluidic reactor: theory and experiment, React. Chem. Eng. 1 (2016) 261–271, https://doi.org/10.1039/c6re00073h.
[193] I. Lignos, S. Stavrakis, G. Nedelcu, L. Protesescu, A.J. Demello, M.V. Kovalenko, Synthesis of cesium lead halide perovskite nanocrystals in a droplet-based microfluidic platform: fast parametric space mapping, Nano Lett. 16 (2016) 1869–1877, https://doi.org/10.1021/acs.nanolett.5b04981.
[194] I. Lignos, R.M. MacEiczyk, M.V. Kovalenko, S. Stavrakis, Tracking the fluorescence lifetimes of cesium lead halide perovskite nanocrystals during their synthesis using a fully automated optofluidic platform, Chem. Mater. 32 (2020) 27–37, https://doi.org/10.1021/acs.chemmater.9b03438.
[195] I. Lignos, V. Morad, Y. Shynkarenko, C. Bernasconi, R.M. Maceiczyk, L. Protesescu, F. Bertolotti, S. Kumar, S.T. Ochsenbein, N. Masciocchi, A. Guagliardi, C.J. Shih, M.I. Bodnarchuk, A.J. Demello, M.V. Kovalenko, Exploration of near-infrared-emissive colloidal multinary lead halide perovskite nanocrystals using an automated microfluidic platform, ACS Nano 12 (2018) 5504–5517, https://doi.org/10.1021/acsnano.8b01122.
[196] Z. He, N. Ranganathan, P. Li, Evaluating nanomedicine with microfluidics, Nanotechnology 29 (2018), https://doi.org/10.1088/1361-6528/aae18a.
[197] D. Zhu, Q. Long, Y. Xu, J. Xing, Evaluating nanoparticles in preclinical research using microfluidic systems, Micromachines 10 (2019), https://doi.org/10.3390/mi10060414.
[198] R.O. Rodrigues, M. Bañobre-López, J. Gallo, P.B. Tavares, A.M.T. Silva, R. Lima, H.T. Gomes, Haemocompatibility of iron oxide nanoparticles synthesized for theranostic applications: a high-sensitivity microfluidic tool, J. Nanoparticle Res. 18 (2016), https://doi.org/10.1007/s11051-016-3498-7.
[199] A.P. Falanga, G. Pitingolo, M. Celentano, A. Cosentino, P. Melone, R. Vecchione, D. Guarnieri, P.A. Netti, Shuttle-mediated nanoparticle transport across an in vitro brain endothelium under flow conditions, Biotechnol. Bioeng. 114 (2017) 1087–1095, https://doi.org/10.1002/bit.26221.
[200] C.A. Cunha-Matos, O.R. Millington, A.W. Wark, M. Zagnoni, Real-time assessment of nanoparticle-mediated antigen delivery and cell response, Lab Chip 16 (2016) 3374–3381, https://doi.org/10.1039/c6lc00599c.
[201] D. Huh, B.D. Matthews, A. Mammoto, M. Montoya-Zavala, H.Y. Hsin, D.E. Ingber, Reconstituting organ-level lung functions on a chip, Science 80 (328) (2010) 1662–1668.
[202] P. Agarwal, H. Wang, M. Sun, J. Xu, S. Zhao, Z. Liu, K.J. Gooch, Y. Zhao, X. Lu, X. He, Microfluidics enabled bottom-up engineering of 3D vascularized tumor for drug discovery, ACS Nano 11 (2017) 6691–6702, https://doi.org/10.1021/acsnano.7b00824.
[203] Tang, et al., Organ-on-a-Chip platforms for studying drug delivery systems, J. Contr. Release 190 (2014) 82–93, https://doi.org/10.1016/j.jconrel.2014.05.004.Organ-on-a-Chip.
[204] S.I. Ahn, Y.J. Sei, H.J. Park, J. Kim, Y. Ryu, J.J. Choi, H.J. Sung, T.J. MacDonald, A.I. Levey, Y.T. Kim, Microengineered human blood–brain barrier platform for understanding nanoparticle transport mechanisms, Nat. Commun. 11 (2020) 1–12, https://doi.org/10.1038/s41467-019-13896-7.
[205] C. Watson, J. Ge, J. Cohen, G. Pyrgiotakis, B.P. Engelward, P. Demokritou, High-throughput screening platform for engineered nanoparticle-mediated genotoxicity using cometchip technology, ACS Nano 8 (2014) 2118–2133, https://doi.org/10.1021/nn404871p.
[206] J. Wu, H. Li, Q. Chen, X. Lin, W. Liu, J.M. Lin, Statistical single-cell analysis of cell cycle-dependent quantum dot cytotoxicity and cellular uptake using a microfluidic system, RSC Adv. 4 (2014) 24929–24934, https://doi.org/10.1039/c4ra01665c.
[207] H. Wang, B. Chen, M. He, X. Li, P. Chen, B. Hu, Study on uptake of gold nanoparticles by single cells using droplet microfluidic chip-inductively coupled plasma mass spectrometry, Talanta 200 (2019) 398–407, https://doi.org/10.1016/j.talanta.2019.03.075.
[208] M. Zhang, C. Xu, L. Jiang, J. Qin, A 3D human lung-on-a-chip model for nanotoxicity testing, Toxicol. Res. (Camb). 7 (2018) 1048–1060, https://doi.org/10.1039/c8tx00156a.
[209] S.M. Amin Arefi, C.W. Tony Yang, D.D. Sin, J.J. Feng, Simulation of nanoparticle transport and adsorption in a microfluidic lung-on-a-chip device, Biomicrofluidics 14 (2020), https://doi.org/10.1063/5.0011353.
[210] P.K. Kabadi, A.L. Rodd, A.E. Simmons, N.J. Messier, R.H. Hurt, A.B. Kane, A novel human 3D lung microtissue model for nanoparticle-induced cell-matrix alterations, Part, Fibre Toxicol 16 (2019) 1–15, https://doi.org/10.1186/s12989-019-0298-0.
[211] K. Huang, R. Boerhan, C. Liu, G. Jiang, Nanoparticles penetrate into the multicellular spheroid-on-chip: effect of surface charge, protein corona, and exterior flow, Mol. Pharm. 14 (2017) 4618–4627, https://doi.org/10.1021/acs.molpharmaceut.7b00726.
[212] M.B. Esch, G.J. Mahler, T. Stokol, M.L. Shuler, Body-on-a-chip simulation with gastrointestinal tract and liver tissues suggests that ingested nanoparticles have the potential to cause liver injury, Lab Chip 14 (2014) 3081–3092, https://doi.org/10.1039/c4lc00371c.
[213] K. Tokarska, M. Bułka, U. Bazylińska, E. Jastrzębska, M. Chudy, A. Dybko, K. A. Wilk, Z. Brzózka, Evaluation of nanoencapsulated verteporfin's cytotoxicity using a microfluidic system, J. Pharmaceut. Biomed. Anal. 127 (2016) 39–48, https://doi.org/10.1016/j.jpba.2016.02.052.
[214] A. Albanese, A.K. Lam, E.A. Sykes, J.V. Rocheleau, W.C.W. Chan, Tumour-on-a-chip provides an optical window into nanoparticle tissue transport, Nat. Commun. 4 (2013) 1–8, https://doi.org/10.1038/ncomms3718.
[215] J.H. Sung, M.L. Shuler, A micro cell culture analog (CCA) with 3-D hydrogel culture of multiple cell lines to assess metabolism-dependent cytotoxicity of anti-cancer drugs, Lab Chip 9 (2009) 1385–1394, https://doi.org/10.1039/b901377f.
[216] J.H. Kim, S.H. Lee, Y.J. Cha, S.J. Hong, S.K. Chung, T.H. Park, S.S. Choi, C. elegans-on-a-chip for in situ and in vivo Ag nanoparticles' uptake and toxicity assay, Sci. Rep. 7 (2017) 1–11, https://doi.org/10.1038/srep40225.
[217] H.J. Pandya, K. Dhingra, D. Prabhakar, V. Chandrasekar, S.K. Natarajan, A. S. Vasan, A. Kulkarni, H. Shafiee, A microfluidic platform for drug screening in a 3D cancer microenvironment, Biosens. Bioelectron. 94 (2017) 632–642, https://doi.org/10.1016/j.bios.2017.03.054.
[218] R.R. Hood, W.N. Vreeland, D.L. Devoe, Microfluidic remote loading for rapid single-step liposomal drug preparation, Lab Chip 14 (2014) 3359–3367, https://doi.org/10.1039/c4lc00390j.
[219] G. Luo, L. Du, Y. Wang, Y. Lu, J. Xu, Controllable preparation of particles with microfluidics, Particuology 9 (2011) 545–558, https://doi.org/10.1016/j.partic.2011.06.004.
[220] Y. Bao, Q. Deng, Y. Li, S. Zhou, Engineering docetaxel-loaded micelles for non-small cell lung cancer : a comparative study of microfluidic and bulk nanoparticle preparation †, RSC Adv. 8 (2018) 31950–31966, https://doi.org/10.1039/c8ra04512g.
[221] M.A. Tomeh, X. Zhao, Recent advances in microfluidics for the preparation of drug and gene delivery systems, Mol. Pharmaceutics 17 (12) (2020) 4421–4434, https://doi.org/10.1021/acs.molpharmaceut.0c00913.
[222] V. Kamat, I. Marathe, V. Ghormade, D. Bodas, K. Paknikar, Synthesis of monodisperse chitosan nanoparticles and in situ drug loading using active microreactor, ACS Appl. Mater. Interfaces 7 (2015) 22839–22847, https://doi.org/10.1021/acsami.5b05100.
[223] J. Yan, X. Xu, J. Zhou, C. Liu, L. Zhang, D. Wang, F. Yang, H. Zhang, Fabrication of a pH/redox-triggered mesoporous silica-based nanoparticle with microfluidics for anticancer drugs doxorubicin and paclitaxel codelivery, ACS Appl. Mater. Interfaces 3 (2020) 1216–1225.
[224] D. Liu, H. Zhang, E. Makila, J. Fan, B. Herranz-Blanco, C.-F. Wang, R. Rosa, A. J. Ribeiro, J. Salonen, J. Hirvonen, H.A. Santos, Microfluidic assisted one-step fabrication of porous silicon@acetalated dextran nanocomposites for precisely controlled combination chemotherapy, Biomaterials 39 (2015) 249–259.
[225] J.J. Lee, K.J. Jeong, M. Hashimoto, A.H. Kwon, A. Rwei, S.A. Shankarappa, J. H. Tsui, D.S. Kohane, Synthetic ligand-coated magnetic nanoparticles for microfluidic bacterial separation from blood, Nano Lett. 14 (2014) 1–5, https://doi.org/10.1021/nl3047305.
[226] Y. Chang, J. Jiang, W. Chen, W. Yang, L. Chen, P. Chen, J. Shen, S. Qian, T. Zhou, L. Wu, L. Hong, Y. Huang, F. Li, Biomimetic metal-organic nanoparticles prepared with a 3D-printed microfluidic device as a novel formulation for disulfiram-based therapy against breast cancer, Appl. Mater. Today. 18 (2020), https://doi.org/10.1016/j.apmt.2019.100492.
[227] J. Qiao, H. Ding, Q. Liu, R. Zhang, L. Qi, Preparation of Polymer@AuNPs with droplets approach for sensing serum copper ions, Anal. Chem. 89 (2017) 2080–2085, https://doi.org/10.1021/acs.analchem.6b04722.
[228] N. Hao, Y. Nie, T. Shen, J.X.J. Zhang, Microfluidics-enabled rational design of immunomagnetic nanomaterials and their shape effect on liquid biopsy, Lab Chip 18 (2018) 1997, https://doi.org/10.1039/c8lc00273h, 2002.
[229] D. Habault, A. Déry, J. Leng, S. Lecommandoux, J.F. Le Meins, O. Sandre, Droplet microfluidics to prepare magnetic polymer vesicles and to confine the heat in magnetic hyperthermia, IEEE Trans. Magn. 49 (2013) 182–190, https://doi.org/10.1109/TMAG.2012.2221688.
[230] J. Ahn, J. Ko, S. Lee, J. Yu, Y.T. Kim, N.L. Jeon, Microfluidics in nanoparticle drug delivery; from synthesis to pre-clinical screening, Adv. Drug Deliv. Rev. 128 (2018) 29–53, https://doi.org/10.1016/j.addr.2018.04.001.
[231] S.C. Hong, K.M. Park, C.R. Hong, J.C. Kim, S.H. Yang, H.S. Yu, H.D. Paik, C. H. Pan, P.S. Chang, Microfluidic assembly of liposomes dual-loaded with catechin and curcumin for enhancing bioavailability, Colloids Surfaces A Physicochem. Eng. Asp. 594 (2020), https://doi.org/10.1016/j.colsurfa.2020.124670.
[232] N. Tahir, A. Madni, W. Li, A. Correia, M.M. Khan, M.A. Rahim, H.A. Santos, Microfluidic fabrication and characterization of Sorafenib-loaded lipid-polymer

hybrid nanoparticles for controlled drug delivery, Int. J. Pharm. 581 (2020), https://doi.org/10.1016/j.ijpharm.2020.119275.
[233] D. Liu, H. Zhang, S. Cito, J. Fan, E. Mäkilä, J. Salonen, J. Hirvonen, T.M. Sikanen, D.A. Weitz, H.A. Santos, Core/shell nanocomposites produced by superfast sequential microfluidic nanoprecipitation, Nano Lett. 17 (2017) 606–614, https://doi.org/10.1021/acs.nanolett.6b03251.
[234] F.S. Majedi, M.M. Hasani-Sadrabadi, J.J. VanDersarl, N. Mokarram, S. Hojjati-Emami, E. Dashtimoghadam, S. Bonakdar, M.A. Shokrgozar, A. Bertsch, P. Renaud, On-chip fabrication of paclitaxel-loaded chitosan nanoparticles for cancer Therapeutics.pdf, Adv. Funct. Mater. 24 (2014) 432–441.
[235] J. Sun, Y. Xianyu, M. Li, W. Liu, L. Zhang, D. Liu, C. Liu, G. Hu, X. Jiang, A microfluidic origami chip for synthesis of functionalized polymeric nanoparticles†, Nanoscale 5 (2013) 5262–5265, https://doi.org/10.1039/c3nr01289a.
[236] J. Wang, K. Zhao, X. Shen, W. Zhang, S. Ji, Y. Song, X. Zhang, R. Rong, X. Wang, Microfluidic synthesis of ultra-small magnetic nanohybrids for enhanced magnetic resonance imaging, J. Mater. Chem. C. 3 (2015) 12418–12429, https://doi.org/10.1039/c5tc02279g.
[237] L. Chronopoulou, C. Sparago, A modular microfluidic platform for the synthesis of biopolymeric nanoparticles entrapping organic actives, J. Nanoparticle Res. 16 (2014), https://doi.org/10.1007/s11051-014-2703-9.
[238] L. Gomez, V. Sebastian, S. Irusta, A. Ibarra, M. Arruebo, J. Santamaria, Scaled-up production of plasmonic nanoparticles using microfluidics: from metal precursors to functionalized and sterilized nanoparticles, Lab Chip 14 (2014) 325–332, https://doi.org/10.1039/c3lc50999k.
[239] P.M. Valencia, O.C. Farokhzad, R. Karnik, R. Langer, Microfluidic technologies for accelerating the clinical translation of nanoparticles, Nat. Nanotechnol. 7 (2012) 623–629, https://doi.org/10.1038/nnano.2012.168.
[240] X. Li, X. Jiang, Microfluidics for producing poly (lactic-co-glycolic acid)-based pharmaceutical nanoparticles ☆, Adv. Drug Deliv. Rev. 128 (2017) 101–114, https://doi.org/10.1016/j.addr.2017.12.015.
[241] X. Hou, T. Zaks, R. Langer, Y. Dong, Lipid nanoparticles for mRNA delivery, Nat. Rev. Mater. (2021), 0123456789, https://doi.org/10.1038/s41578-021-00358-0.